Abstract

Precise Measurement of the Positive Muon Anomalous Magnetic Moment

Huaizhang Deng
2002

A precise measurement of the anomalous magnetic moment, $a_\mu = (g-2)/2$, for the positive muon has been made at the Brookhaven Alternating Gradient Synchrotron. Highly polarized μ^+ of 3.09 GeV/c from a secondary beam line are injected through a superconducting inflector into a storage ring 14.2 m in diameter. The superferric storage ring has a homogeneous magnetic field of 1.45 T, which is measured by an NMR (nuclear magnetic resonance) system relative to the free proton NMR angular frequency ω_p. The muon spin precesses faster than its momentum rotates by an angular frequency ω_a in the magnetic field. The frequency ω_a is determined by measuring the decay positrons from the stored muons. The value of the muon anomalous magnetic moment is obtained by

$$a_\mu = \frac{\omega_a}{\frac{e}{m_\mu c}\langle B\rangle}, \tag{1}$$

where $\langle B\rangle$ is the magnetic field weighted over the muon distribution in space and time, e and m_μ are the charge and the the mass of the muon, and c is the speed of light in vacuum.

During the data-taking period in 1999, the number of collected positrons increased by a factor of 20 compared to the previous data-taking period in 1998. The result from the data taken in 1999,

$$a_{\mu^+} = 11\ 659\ 202(14)(6) \times 10^{-10}\ (1.3\ \text{ppm}). \tag{2}$$

is in good agreement with previous measurements and reduces the combined error by a factor of about 3. The difference between the weighted mean of all experimental results, $a_\mu(\text{exp}) = 11\ 659\ 203(15) \times 10^{-10}$, and the theoretical value from the standard model, $a_\mu(\text{SM}) = 11\ 659\ 176.6(6.7) \times 10^{-10}$, is

$$a_\mu(\text{exp}) - a_\mu(\text{SM}) = 26(16) \times 10^{-10}. \tag{3}$$

The error is the addition in quadrature of experimental and theoretical uncertainties. The difference is 1.6 times the stated error.

Precise Measurement of the Positive Muon Anomalous Magnetic Moment

Huaizhang Deng
Advisor : Vernon W. Hughes
Yale University

September 2002

UMI Number: 3068268

ProQuest Information and Learning Company
300 North Zeeb Road
P.O. Box 1346
Ann Arbor, MI 48106-1346

Dedication

This dissertation is dedicated to my parents, Deng Yanmin and Tu Xizu, who dedicate themselves to my life.

Acknowledgements

I am fortunate to have the opportunity to work on this experiment for the past 5 years. I gratefully acknowledge all the members of the collaboration and all people who have contributed to this experiment.

I want to thank my advisor Prof. Vernon W. Hughes for providing me with the opportunity to work on the muon g-2 experiment and for his advice and encouragement which guide me through the studies. This dissertation is part of the research carried out through his vision throughout past twenty years.

My gratitude also goes to my colleagues Mario Deile, Satish Dhawan, David Kawall, Matthias Grosse Perdekamp, Jörg Pretz, Sergei Redin, Ernst Sichtermann and Axel Steinmetz who have all dedicated part of their valuable time for my works.

I thank also Alex Grossmann, Klaus Jungmann and Ralf Prigl for their great help and their contributions to NMR system and the analysis of the magnetic field.

I would like to thank my parents and my sister for their love, support and pride in my work. Finally, I thank Qian Wang for her love and encouragement. Thank you.

This experiment is funded by the Department of Energy of United States.

Contents

List of Tables

List of Figures

Chapter 1

Introduction

The gyromagnetic factor of a particle is defined as

$$g = \left(\frac{\mu}{e\hbar/2mc}\right) / \left(\frac{S}{\hbar}\right), \tag{1.1}$$

where μ, S, m, and e are the magnetic moment, the spin, the mass, and the charge of that particle. For a pointlike lepton Dirac theory gives $g = 2$. Virtual radiative corretions cause the g value for leptons to differ from 2. The anomalous g-value is defined as $a = (g-2)/2$.

The anomalous g-value of the electron and muon, a_e and a_μ, played an important role in the development of particle physics and continue to serve as fundamental quantities for testing the validity of the Standard Model and putting stringent constraints on speculative theories beyond the Standard Model.

For the electron, the experimental value of a_e has been determined to be

$$a_e = 11\ 596\ 521\ 884(43) \times 10^{-13}\ (3.7\ \text{ppb})[1,\ 2]. \tag{1.2}$$

This value is from the measurement of a single electron confined in an electromagnetic trap with a strong magnetic field. The theoretical value of a_e[3, 4] has been calculated through the $\mathcal{O}(\alpha^4)$ term for the contribution from virtual electrons and photons. The result is

$$\begin{aligned} a_e(\text{QED}\ :\ e,\gamma) \ &= \ 0.5\left(\frac{\alpha}{\pi}\right) + 0.328\ 478\ 965\ 6...\left(\frac{\alpha}{\pi}\right)^2 + \\ &\quad 1.181\ 241\ 5...\left(\frac{\alpha}{\pi}\right)^3 - 1.509\ 8(384)\left(\frac{\alpha}{\pi}\right)^4. \end{aligned} \tag{1.3}$$

where the first three coefficients are analytic values and the last coefficient is a numerical evaluation. The contribution to a_e from heavier particles is $43.93(27) \times 10^{-13}$, at the level of the the uncertainty of experimental value. Equating experimental and theoretical value of a_e provides the best determination of the fine structure constant,

$$\alpha^{-1}(a_e) = 137.035\ 999\ 76(50)[4,\ 5]. \tag{1.4}$$

This value agrees with the less precise value from the Quantum-Hall effect measurements

$$\alpha^{-1}(\text{Hall}) = 137.035\ 003\ 7(33)[6]. \tag{1.5}$$

To test the current theory requires an alternative measurement of α with an accuracy comparable to that from the eletron $g-2$ experiment.

For the muon, because the muon mass m_μ is larger than the electron mass m_e, the contribution to a_μ from heavier particles such as hadrons or weak vector bosons through virtual processes is greater than that to a_e typically by a factor of $(m_\mu/m_e)^2 \simeq 4 \times 10^4$. This sensitivity enhancement of a_μ applies generally also for postulated new particles such as supersymmetric particles. Hence, the measurement of a_μ provides us more information than that of a_e though a_μ is less well known than a_e.

The muon anomalous magnetic moment was measured three times in CERN [7, 8, 9]. The last CERN muon $g-2$ experiment[9], from 1969 to 1976, measured both μ^+ and μ^- and their results are

$$\begin{aligned} a_{\mu^+} &= 1\ 165\ 910(11) \times 10^{-9}\ (9.4\ \text{ppm}) \\ a_{\mu^-} &= 1\ 165\ 937(12) \times 10^{-9}\ (10.3\ \text{ppm}). \end{aligned} \tag{1.6}$$

The two values agree within two times the standard deviation. The equality of two values is the test of CPT invariance. The combined value for the muon is

$$a_\mu = 1\ 165\ 923(8.4) \times 10^{-9}\ (7.2\ \text{ppm}), \tag{1.7}$$

which is in good agreement with the present theoretical value from the Standard Model $a_\mu(\text{SM}) = 11\ 659\ 177(7) \times 10^{-10}$[10]. The dominant error for the CERN muon $g-2$ experiment was the statistical error of 7 ppm. The major systematic error was a 1.5 ppm error in the limited knowledge of the magnetic field.

The BNL experiment E821 uses a muon storage ring and has the goal of measuring a_μ to 0.4 ppm which would represent a factor 20 improvement over the latest measurement from CERN. The specific scientific motivations are the following:

1. To measure the effect of the weak interactions on a_μ. This measurement will provide a test of the renormalizability of the unified electroweak theory.

2. To search for physics beyond the Standard Model.

   Many speculative theories beyond the Standard Model propose a difference, $a_\mu(\text{exp})$-$a_\mu(\text{SM})$, of an amount which would be detected by a measurement of a_μ to 0.35 ppm. The muon anomalous g-value a_μ can be regarded as a standard against which any speculative new theories can be tested. Such a precision test is complementary to direct searches for new physics with the highest energy accelerators.

Compared to the CERN muon $g-2$ experiment, the major improvements of this experiment are :

1. the use of the BNL AGS proton beam which is a factor of 200 more intense than the CERN proton beam at the time of CERN $g-2$ experiment;
2. a superconducting magnet of high stability and homogeneity, and an NMR (nuclear magnetic resonance) system capable of 0.25 ppm absolute accuracy;
3. the use of muon injection which substantially increases the number of stored muons in the storage ring and reduces the background compared to the pion injection used at CERN;
4. an improved electron spectrometer system with higher energy resolution;
5. the use of fast modern electronics and modern computers.

The experiment started taking data on μ^+ in 1997 after more than 10 years of preparation. Since then there have been 3-4 months long data-taking periods each year. In 1997, π^+ injection was used. The result from the data collected in this run was

$$a_{\mu^+} = 1\ 165\ 925(15) \times 10^{-9}(13\ \text{ppm})[11]. \tag{1.8}$$

After the 1997 run, magnetic kickers were installed and muon injection has been used ever since. A thermal insulator and a feedback system were installed and significantly improved the magnetic field stability. Some 84 million decay e^+ from the data collected in 1998 were analyzed and the result is

$$a_{\mu^+} = 11\ 659\ 191(59) \times 10^{-10}(5\ \text{ppm})[12]. \tag{1.9}$$

In 1999, much more data were collected and 0.95×10^9 e^+ were analyzed. Hence the statistical error, which is the dominant error, was reduced significantly. The data taken in 1999 give

$$a_{\mu^+} = 11\ 659\ 202(15) \times 10^{-10}(1.3\ \text{ppm})[13]. \tag{1.10}$$

The world experimental value of a_μ is determined to the accuracy of 1.3 ppm by combining the CERN measurement[9] with the measurements at Brookhaven National Laboratory[11, 12, 13]:

$$a_\mu(\text{exp}) = 11\ 659\ 203(15) \times 10^{-10}\ (1.3\ \text{ppm}).$$

The theoretical value in the Standard Model is

$$a_\mu(\text{SM}) = 11\ 659\ 177(7) \times 10^{-10}\ (0.6\ \text{ppm})[10]. \tag{1.11}$$

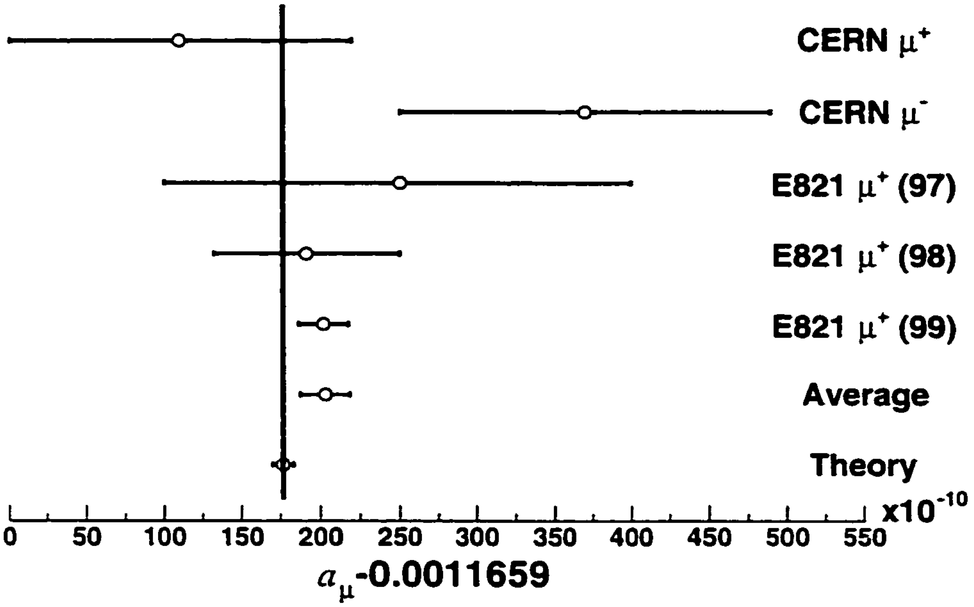

Figure 1.1: Experimental and theoretical values of a_μ.

The difference between the world experimental and theoretical value is $26(16) \times 10^{-10}(1.6\sigma)$. The comparison between world experimental and theoretical values is shown in Fig. 1.1.

Four times more data have been taken in 2000. The error on a_{μ^+} is reduced to 0.7 ppm[14]. In 2001, a_{μ^-} was measured and the data are under analysis now.

This dissertation reports in detail the result of muon $g-2$ experiment at Brookhaven National Laboratory based on the data collected from January to March 1999. The author of this dissertation took part in the shimming and measurement of the magnetic field, data-taking, construction and measurement of Čerenkov detector. The author also made one of the two independent analyses of the magnetic field measurement, and did studies for the analysis of the muon spin precession frequency.

In Chapter 2, the calculation of the theoretical value of a_μ and its current status are discussed, including the prediction of the Standard Model and the speculation from theories beyond Standard Model.

In Chapter 3, we discuss the principle and the experimental setup of the muon $g-2$ experiment.

In Chapter 4, we describe the running of the experiment in 1999.

In Chapter 5, the analysis of the magnetic field measurements is presented.

In Chapter 6, the analysis of the muon spin precession frequency is presented.

In Chapter 7, we give the result of a_μ from our data taken in the 1999 run and a future perspective.

Chapter 2

Theory of the muon anomalous magnetic moment

The lowest order Feynman diagram for the interaction of a muon with an external magnetic field is shown in Fig 2.1 and gives $g = 2$.

The anomalous g-value, defined as $a_\mu = (g-2)/2$, deviates from 0 because of radiative corrections to Fig. 2.1. In the Standard Model, a_μ comes from the contributions of quantum electrodynamics, weak, and hadronic interactions.

$$a_\mu(\mathrm{SM}) = a_\mu(\mathrm{QED}) + a_\mu(\mathrm{weak}) + a_\mu(\mathrm{had})[10, 15]. \tag{2.1}$$

2.1 QED Contribution

The contribution of the electromagnetic interaction, $a_\mu(\mathrm{QED})$, includes those of the photon, electron, muon, and tauon fields. Fig. 2.2 shows some low order QED contributions to a_μ.

The result of QED contribution is most conveniently expressed as

$$a_\mu(QED) = C_1\left(\frac{\alpha}{\pi}\right)+C_2\left(\frac{\alpha}{\pi}\right)^2+C_3\left(\frac{\alpha}{\pi}\right)^3+C_4\left(\frac{\alpha}{\pi}\right)^4+C_5\left(\frac{\alpha}{\pi}\right)^5+...[15], \tag{2.2}$$

where $C_1 = 0.5$; $C_2 = 0.765\,857\,388(44)$; $C_3 = 24.050\,509(2)$; $C_4 = 126.04(41)$; $C_5 = 930(170)$. Using $\alpha^{-1} = 137.035\,999\,58(52)$ from Eq. 1.4, we obtain:

$$a_\mu(\mathrm{QED}) = 11\,658\,470.56(0.29) \times 10^{-10}(25\ \mathrm{ppb})[10, 15] \tag{2.3}$$

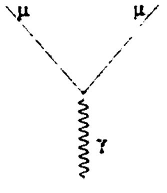

Figure 2.1: The interaction of a muon with an external magnetic field.

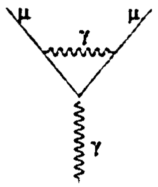

Second Order

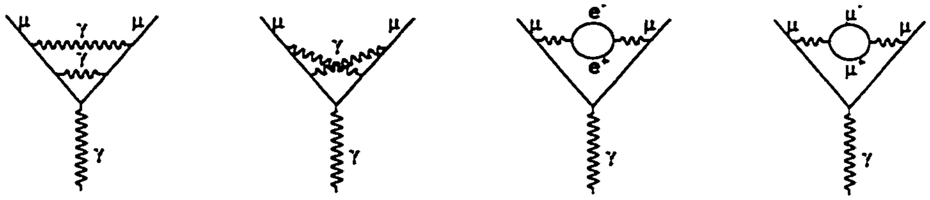

Fourth Order

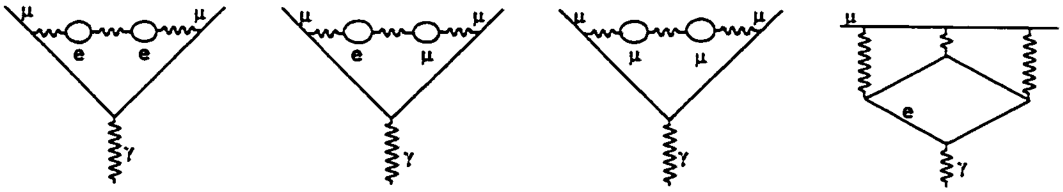

Sixth Order

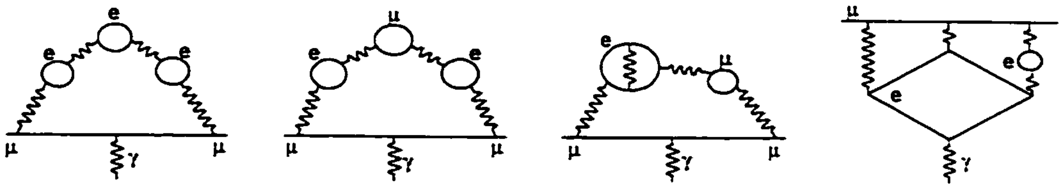

Eighth Order

Figure 2.2: Examples of the high order QED contribution to a_μ.

2.2 Weak Contribution

The weak interaction contribution based on the standard electroweak theory arises in lowest order from the single loop diagrams in Fig. 2.3 which involves ν_μ, Z, and H particle exchanges. The diagrams with the W and Z particles are

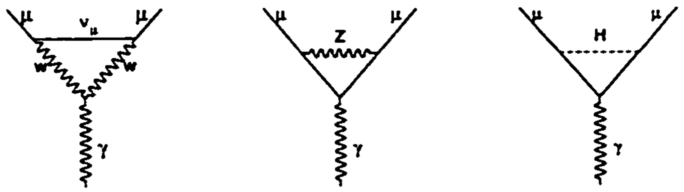

Figure 2.3: Lowest order weak contribution to a_μ.

evaluated to contribute

$$a_\mu(\mathrm{W}) = \frac{G_F m_\mu^2}{8\pi^2\sqrt{2}} \times \frac{10}{3} = 38.9 \times 10^{-10}, \tag{2.4}$$

$$a_\mu(\mathrm{Z}) = \frac{G_F m_\mu^2}{8\pi^2\sqrt{2}} \times \frac{1}{3}\left[(3 - 4\cos^2\theta_W)^2 - 5\right] = -19.4 \times 10^{-10}, \tag{2.5}$$

where the Fermi constant $G_F = 1.166\ 39(1) \times 10^{-5}$ GeV^2[16] and the weak mixing angle $\sin^2\theta_W = 1 - m_W^2/m_Z^2 = 0.231$[16]. Since searches establish that the mass of the Higgs particle, m_H, is greater than 100 GeV, the contribution from the diagram with H is negligible[10].

The next order weak contribution involves two loop diagrams (Fig. 2.4), including low energy hadronic electroweak loops, and has been fully calculated[17, 18]. The total weak contribution is

$$\begin{aligned} a_\mu(\mathrm{weak}) &= a_\mu^{weak}(1\ loop) + a_\mu^{weak}(2\ loop) \\ &= 19.5 \times 10^{-10} - 4.4 \times 10^{-10} \\ &= 15.1(0.4) \times 10^{-10}, \end{aligned} \tag{2.6}$$

where the quoted error is an estimate of hadronic, Higgs and higher order corrections[10]. Higher order leading logs of the form $(\alpha \ln m_Z^2/m_\mu^2)^n$, can be computed via renormalization group techniques. Due to cancellations, they give a relatively small contribution of 0.5×10^{-11} to a_μ[19].

Comparison of theory and experiment on a_μ(weak) will constitute a new and sensitive test of the unified electroweak theory with its prescription for renormalizability.

2.3 Hadronic Contribution

The hadronic contribution to a_μ is about 60 ppm, and contributes the principal uncertainty to a_μ(SM). The calculation of the lowest order hadronic contribution(Fig. 2.5), a_μ(had 1), involves low energy scales near the muon mass.

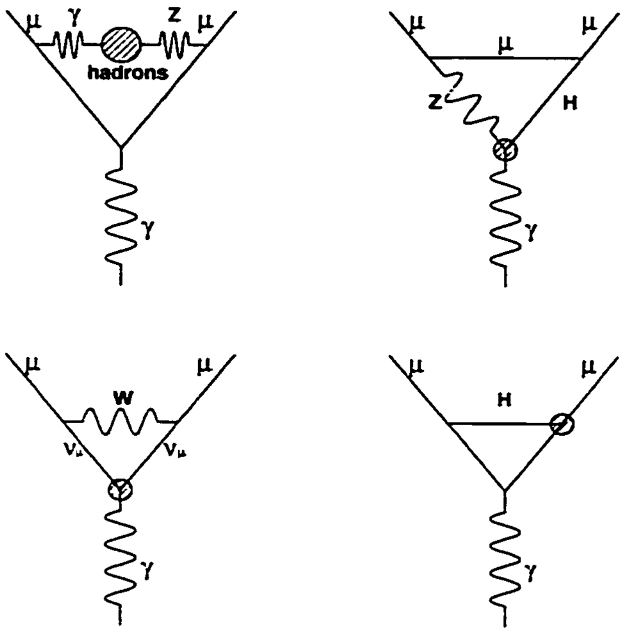

Figure 2.4: Examples of higher order two loop electroweak diagrams.

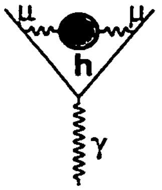

Figure 2.5: Lowest order hadronic contribution to a_μ.

Therefore it can not now be done from QCD alone. However, by dispersion theory[20] this contribution can be related to the measured ratio

$$R(s) = \frac{\sigma_{\mathrm{total}}(e^+e^- \rightarrow hadrons)}{\sigma_{\mathrm{total}}(e^+e^- \rightarrow \mu^+\mu^-)}, \tag{2.7}$$

in which $\sqrt{s}$ is the total energy in the center of mass frame for the e^+e^- collision(Fig. 2.6.a) and the cross sections of the reactions are denoted by σ. The dispersion relation

$$a_\mu(\mathrm{had\ 1}) = \left(\frac{\alpha m_\mu}{3\pi}\right)^2 \int_{4m_\pi^2}^{\infty} \frac{ds}{s^2} K(s) R(s), \tag{2.8}$$

involves the integral from the threshold energy for pion pair, $4m_\pi^2$, to ∞. The kinematic factor $K(s)$, which decreases monotonically from about 4.045 to 0

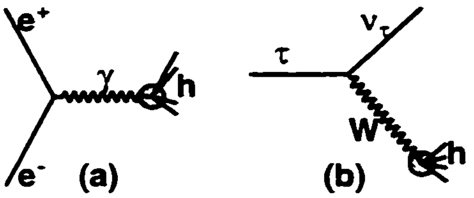

Figure 2.6: (a) The hadronic production of e^+e^- collision. (b) Hadronic τ decay.

when s increases from $4m_\pi^2$ to ∞,

$$K(s) = x^2\left(1 - \frac{x^2}{2}\right) + (1+x)^2\left(1 + \frac{1}{x^2}\right)\left[\ln(1+x) - x + \frac{x^2}{2}\right] + \frac{1+x}{1-x}x^2 \ln x, \tag{2.9}$$

where

$$x = \frac{1 - \sqrt{1 - 4m_\mu^2/s}}{1 + \sqrt{1 - 4m_\mu^2/s}}. \tag{2.10}$$

Data from hadronic τ decay can also be used with the assumption of the validity of conserved vector current(CVC)[21, 22] The diagram is shown in Fig. 2.6.b, in which the weak charge current can be related to the isovector part of the electromagnetic current in Fig. 2.6.a. Only the vector weak current, through which the τ decays to an even number of pions, is related to $g - 2$. The isospin violation effect of order a few percent is taken into account in calculating a_μ.

The principal contribution to a_μ(had 1) in Eq. 2.8 comes from the region of $\sqrt{s} < 1$ GeV because of the factor s^{-2} in the dispersion relation and large $R(s)$ at some resonances in low energy region. Measurements of R have been made at the Budker Institute of Nuclear Physics in Novosibirsk in the energy range of $\sqrt{s} = 0.3 - 1.4$ GeV[23]. Data on R were also obtained with the e^+e^- collider in Beijing in the range of $\sqrt{s} = 2 - 5$ GeV[24]. Data on hadronic τ decay come from CLEO-II[25], ALEPH[26], and OPAL[27]. For the higher energy region, perturbative QCD becomes applicable and is used in the evaluation of a_μ(had 1) for energy region $\sqrt{s} > 1.8$ GeV. The evaluation from QCD now is confirmed by the data from Beijing[24]. The value of a_μ(had1) is currently evaluated as a_μ(had 1)= $692.4(6.2) \times 10^{-10}$(0.6 ppm)[21].

Feynman diagrams for the next-to-lowest order hadronic contributions, a_μ(had 2), are shown in Fig. 2.7. These contributions can be expressed in terms of the dispersion integral and is evaluated to be

$$a_\mu(\text{had 2}) = 10.1(0.6) \times 10^{-10}[28, 22]. \tag{2.11}$$

The evaluation of hadronic light-by-light scattering, as shown Figure 2.8, has not been successfully expressed in terms of experimentally accessible variables. Approximate calculations within the framework of chiral perturbation

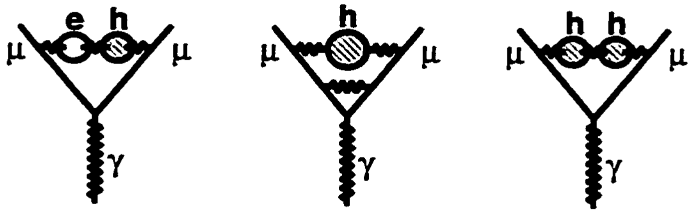

Figure 2.7: Higher order hadronic contribution to a_μ.

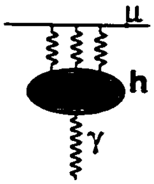

Figure 2.8: Hadronic light-by-light contribution to a_μ.

theory[29, 30] initially gave

$$a_\mu(\text{had lbl}) = -8.5(2.5) \times 10^{-10}. \tag{2.12}$$

Subsequent evaluation of the pion-pole contribution using a description of $\pi^0 - \gamma^* - \gamma^*$ transition form factor based on large-N_c and short distance properties of QCD gave a value of the same magnitude but opposite sign to the previous calculations[31, 32]. This calculation involved an effective field approach, and its result was confirmed[33] in a vector dominance model calculation. Then the authors of the earlier calculations discovered an error in sign[34, 35]. We now take

$$a_\mu(\text{had lbl}) = +8.6(3.2) \times 10^{-10}. \tag{2.13}$$

The hadronic contribution up to the 2nd order

$$\begin{aligned} a_\mu(\text{had}) &= a_\mu(\text{had 1}) + a_\mu(\text{had 2}) + a_\mu(\text{had lbl}) \\ &= 692.4(6.2) \times 10^{-10} - 10.1(0.6) \times 10^{-10} + 8.6(3.2) \times 10^{-10} \\ &= 691(7) \times 10^{-10}. \end{aligned} \tag{2.14}$$

The inclusion of the new experimental measurements of R from Beijing[36] and Novosibirsk[37] and measurements from hadronic τ decays[25] should reduce the error in a_μ(had) in future. New data from e^+e^- collisions is expected from the Frascati ϕ factory and from the B factories.

Adding the QED, weak, and hadronic contributions, we obtain

$$a_\mu(\text{SM}) = 11\ 659\ 177(7) \times 10^{-10}\ (0.6\ \text{ppm}). \tag{2.15}$$

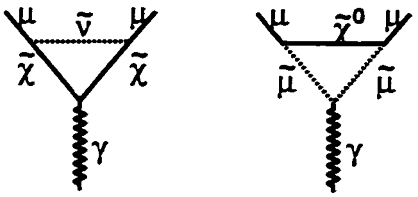

Figure 2.9: Supersymmetric loop contributions to a_μ.

2.4 Contributions Beyond the Standard Model

Extensions of the standard model will in general contribute to a_μ. Hence, a comparison of a_μ(expt) with a_μ(SM) can in principle detect physics beyond the standard model[38]. Two classes of extensions can be considered. One involves the introduction of extra dimensions or extra particles, particularly supersymmetric particles. The other postulates compositeness or internal structure for leptons, quarks or gauge bosons.

The muon $g-2$ value is particularly sensitive to supersymmetry[39, 40, 41]. The leading supersymmetry contribution to a_μ comes from sneutrino-chargino and smuon-neutralino loops as shown in Fig. 2.9. In the limit of large $\tan\beta$, which is the ratio of the vacuum expectation values of the two Higgs doublets, and for a degenerate spectrum of superparticles with mass $\widetilde{m}$, the leading effect is given by

$$\begin{aligned} |a_\mu(SUSY)| &\approx \frac{\alpha(M_Z)}{8\pi\sin^2\theta_W}\frac{m_\mu^2}{\widetilde{m}^2}\tan\beta\left(1-\frac{4\alpha}{\pi}\ln\frac{\widetilde{m}}{m_\mu}\right) \\ &\approx 14\times10^{-10}\left(\frac{100\ GeV}{\widetilde{m}}\right)\tan\beta[10]. \end{aligned} \qquad (2.16)$$

Leptoquarks[42] or theories with extra dimensions[43] could also lead to a difference between a_μ(exp) and a_μ(SM).

In the standard model leptons, quarks and gauge bosons are assumed to be pointlike elementary particles with no internal structure. The magnetic moment of a particle provides a sensitive test for its compositeness. If the muon is composite, the current theoretical viewpoint would imply that

$$|a_\mu(\text{muon structure})| \approx \frac{m_\mu^2}{\Lambda^2}[10,\ 44], \qquad (2.17)$$

in which Λ is the composite mass scale. Determination of a_μ to 0.35 ppm would be sensitive to $\Lambda \sim 4$ TeV. If the muon were composite, excited muon states would be expected, and from an experimental accuracy for a_μ at 0.35 ppm a sensitivity to the mass of the excited muon m_μ^* up to 400 GeV would be obtained. Compositeness of the W gauge boson or new strong dynamics would lead to an anomalous g_W value $\Delta\kappa$. Determination of a_μ to 0.35 ppm would provide a sensitivity to $\Delta\kappa = 0.04$, which corresponds to $\Lambda_W \sim 2$ TeV.

In the radiative muon mass model[44], the muon mass is zero due to an underlying chiral symmetry. The symmetry is broken by quantum loop effect and this leads to a finite calculable mass for the muon. The source of this chiral symmetry breaking also contributes to a_μ. This contribution is generally given by

$$a_\mu(\text{rad } \mu \text{ mass}) \approx C\frac{m_\mu^2}{M^2}, \qquad C \sim \mathcal{O}(1) \tag{2.18}$$

where M is some physical high mass scale associated with the chiral symmetry breaking interaction and C is a model-dependent number roughly of order of 1(it can be larger). Determination of a_μ to 0.35 ppm would be sensitive to $M \sim 4$ TeV

Chapter 3

Muon $g-2$ experiment at BNL

3.1 Principles and Overview

For a muon moving in a uniform magnetic field $\vec{B}$, which is perpendicular to the muon spin direction and to the plane of the orbit, and with an electric field $\vec{E}$, both the spin and the momentum precess as indicated in Fig. 3.1. The angular frequency difference, ω_a, between the spin precession frequency ω_s and the cyclotron frequency ω_c is given by

$$\vec{\omega}_a = \vec{\omega}_s - \vec{\omega}_c = -\frac{e}{m_\mu c}\left[a_\mu \vec{B} - \left(a_\mu - \frac{1}{\gamma^2-1}\right)\vec{\beta}\times\vec{E}\right] \tag{3.1}$$

for $\vec{\beta}\cdot\vec{B} = 0$ and $\vec{\beta}\cdot\vec{E} = 0$, where m_μ and e are the mass and charge of the muon, c is the speed of light, β is the ratio of speed of the muon and the speed of light, and $\gamma = 1/\sqrt{1-\beta^2}$. In our present muon $g-2$ experiment, the dependence of ω_a on the electric field is eliminated by storing muons with the "magic" $\gamma = 29.3$ such that

$$a_\mu - \frac{1}{\gamma^2-1} = 0. \tag{3.2}$$

This corresponds to a muon momentum $p = 3.09$ GeV/c. Hence, the measurement of ω_a and B determines a_μ,

$$a_\mu = \frac{\omega_a}{\frac{e}{m_\mu c}B}. \tag{3.3}$$

In our experiment, the magnetic field is measured by an NMR system which is calibrated with respect to the free proton NMR angular frequency ω_p as

$$B = \frac{\hbar\omega_p}{2\mu_p}, \tag{3.4}$$

where μ_p is the magnetic moment of the free proton. By combination with 3.3, 3.4 and using muon spin $S/\hbar = 1/2$ and the definition of $g_\mu = 2(1+a_\mu)$,

$$a_\mu = \frac{\omega_a}{\frac{e}{m_\mu c}\frac{\hbar\omega_p}{2\mu_p}} = \frac{\omega_a}{\frac{4\mu_\mu}{\hbar g_\mu}\frac{\hbar\omega_p}{2\mu_p}} = \frac{\omega_a/\omega_p}{\frac{\mu_\mu}{(1+a_\mu)\mu_p}} = \frac{\omega_a/\omega_p}{\mu_\mu/\mu_p}(1+a_\mu), \tag{3.5}$$

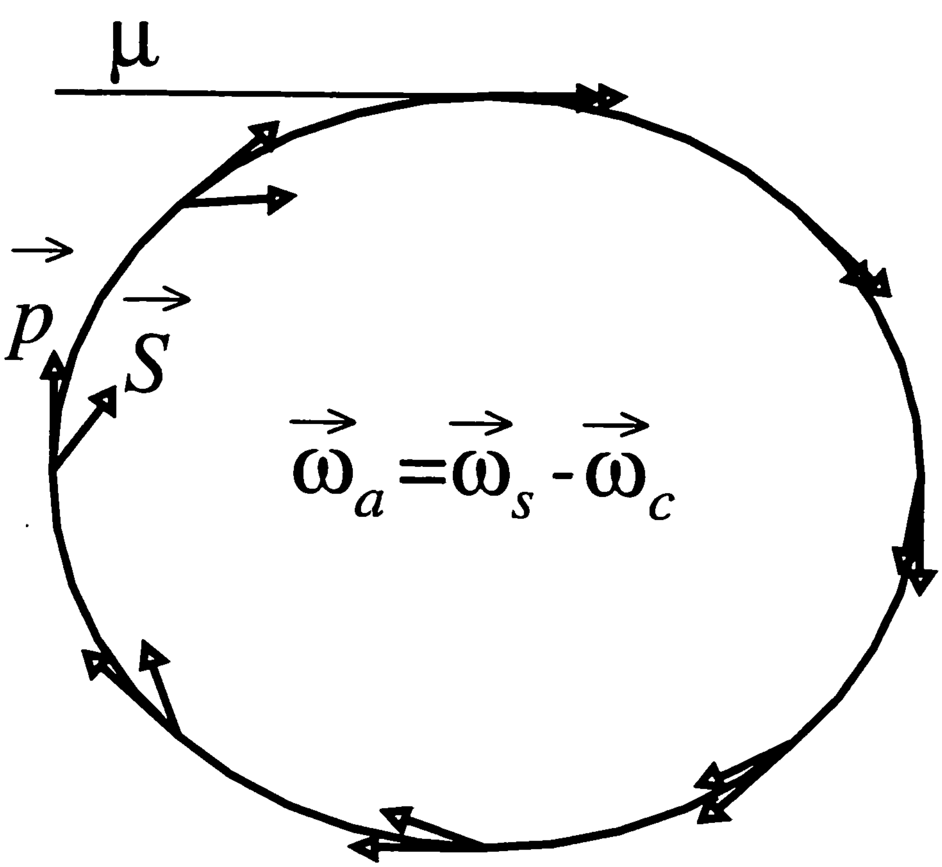

Figure 3.1: Muon momentum ($\vec{p}$) and spin ($\vec{S}$) motion in an electromagnetic field, where ω_c is the angular frequency of the momentum precession and ω_s is the angular frequency of the spin precession.

so that

$$a_\mu = \frac{\omega_a/\omega_p}{\mu_\mu/\mu_p - \omega_a/\omega_p}. \tag{3.6}$$

The ratio $\mu_\mu/\mu_p = 3.183\ 345\ 39(10)$[16], as determined from muonium spectroscopy [45].

The frequency ω_a is measured by counting high energy decay positrons. In the muon rest frame, parity violation in the decay $\mu^+ \to e^+\nu_e\bar{\nu}_\mu$ causes e^+ to be emitted with an angular and energy asymmetry with respect to the muon spin direction[16]. The differential decay rate $d\Gamma$ is

$$\frac{d^2\Gamma}{dx\,d\cos\theta} = \frac{G_F^2 m_\mu^2}{192\pi^3}[3 - 2x + \cos\theta(2x-1)]x^2, \tag{3.7}$$

where θ is the angle between the electron momentum and the muon spin, and $x = 2E_e/m_\mu$. Positrons are emitted preferentially along the muon spin direction. Positrons emitted along the muon momentum direction get the largest

Lorentz boost and have highest energy in the laboratory frame. Hence, the angle between the muon momentum and muon spin determines the number of high energy decay positrons. While the muon spin precesses with angular frequency ω_s and the muon momentum precesses with angular ω_c in the magnetic field, the number of decay positrons with energy greater than some threshold energy E oscillates with the angular frequency $\omega_a = \omega_s - \omega_c$ and is ideally described by

$$N(t) = N_0(E)e^{-t/(\gamma\tau)}\{1 + A(E)\sin[\omega_a t + \phi_a(E)]\} \tag{3.8}$$

in which $\gamma\tau$ is the dilated muon life time, A is the asymmetry, ϕ is the phase of the oscillation. Both A and ϕ depend on the energy threshold of the decay positrons. However, the frequency ω_a does not depend on E.

The general arrangement of the muon $g-2$ experiment[46] is shown in Fig. 3.2. The proton beam from the Alternating Gradient Synchrotron(AGS)

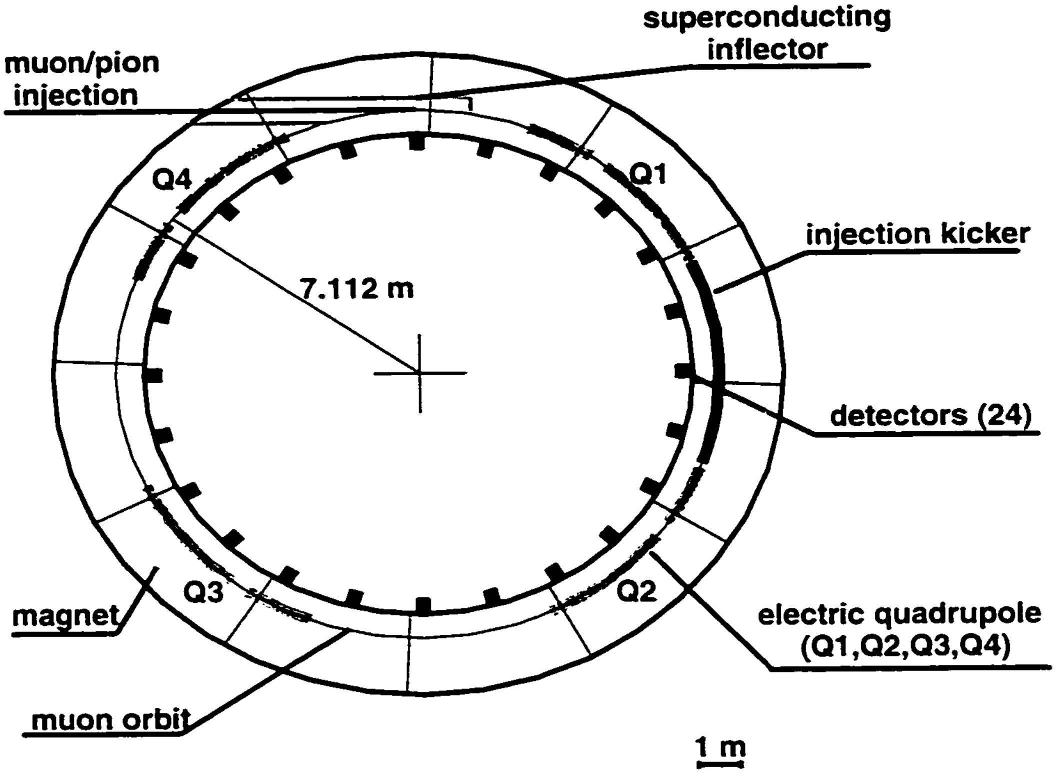

Figure 3.2: General arrangement of the muon $g-2$ experiment.

strikes a nickel target to produce pions. The pions are captured into a secondary beamline where a fraction of about 50% decays to muons. We select the high energy muons which come from the forward decay. They are polarized due to the parity violation in the decay $\pi^+ \rightarrow \mu^+\nu_\mu$. The muons are injected through a superconducting inflector into the muon storage ring with

1.45 T uniform magnetic field which is measured by a NMR system relative to the free proton NMR frequency. A pulsed magnetic kicker at about 90° from the injection point gives muons a 10 mrad deflection which places the muons onto stored orbits. The electrostatic quadrupole fields provide vertical focusing. The decay positrons are detected by 24 lead/scintillating fiber electromagnetic calorimenters read out by waveform digitizers. Both the waveform digitizer and NMR clocks were phase locked to the Loran C frequency signal.

The details of the experiment setup are presented in the following sections.

3.2 Alternating Gradient Synchrotron and Secondary Beamline

The AGS at Brookhaven National Laboratory delivers typically 4×10^{13} protons of 24 GeV in each cycle of 2.5 s. The protons are directed in six bunches, separated by 33 ms, onto a nickel target. After the target, the dipole magnets, D1 and D4, and the collimators K1 and K2, are used to select pions. K1 determines the upper limit on the pion momentum and K2 the lower limit. The pions are then transported along a 116 m secondary beam line. The scheme of the $g-2$ beam line is shown in Fig. 3.3. In the beamline, a fraction of

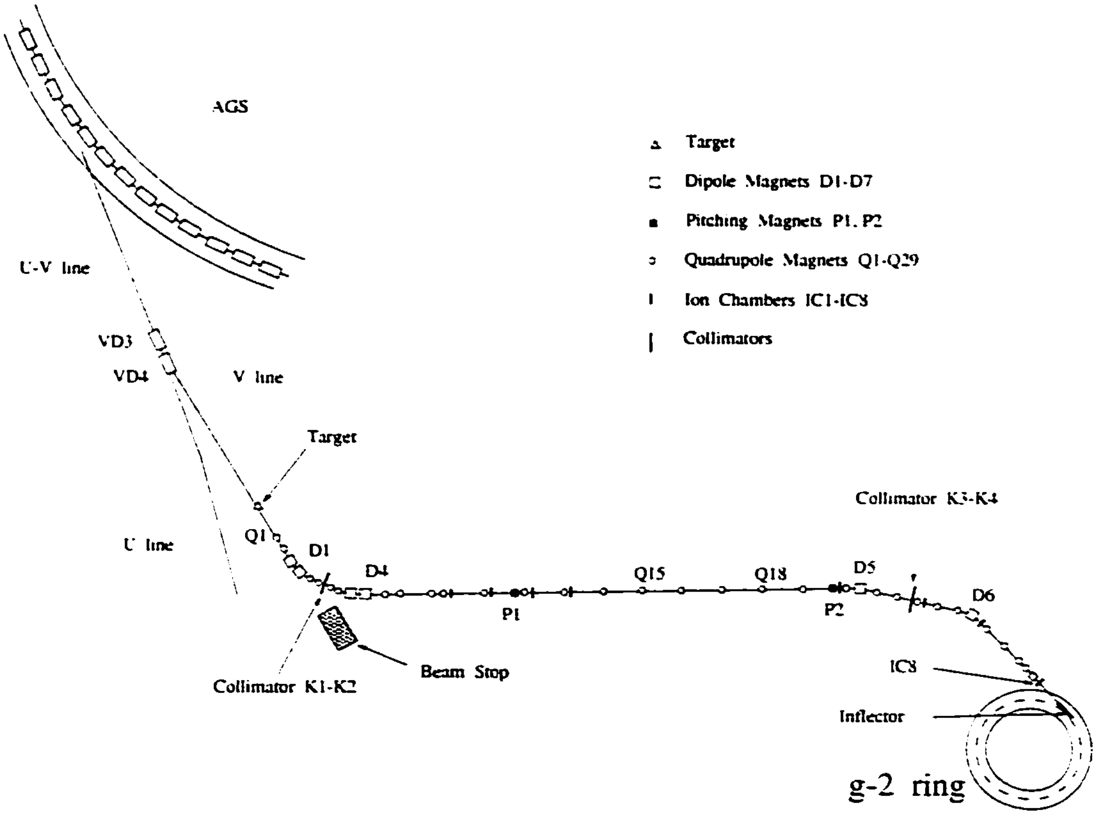

Figure 3.3: $g-2$ secondary beam line.

$\sim$ 50% of the pions decays into muons. The particles are transported through the beamline with its 38 magnets and the beam profile is measured by 8 ion chambers. At the end of the beamline, dipole magnets D5 and D6 together with collimators K3 and K4 are used to select the particles to be injected into our storage ring according to their momentum. K3 sets the upper limit on the momentum and K4 sets the lower limit. Other particles were directed into a beam dump. The beam composition was measured by a Čerenkov counter located just before the last ion chamber IC8 in the 1998 run during which the beamline settings were similar to those in the 1999 run. The numbers of e^+, μ^+ and π^+ were found to be roughly equal in the beam. The number of protons is estimated to be about one third of the number of pions by calculations. The Čerenkov counter was removed from the beam path during the normal running period to improve the beam emittance. Finally the beam is injected into the inflector.

3.3 Superconducting Inflector

The injection of a particle beam into a storage ring is usually done with a pulsed magnetic inflector[47] which locally cancels the field of the main magnet, so that the beam enters the storage region as close as possible and almost tangent to the equilibrium orbit of the ring. Because of the high beam repetition rate in our experiment, it was concluded that a pulsed inflector would be very difficult to build regardless of the uncertainty of the effect due to the pulsed inflector field on the field of the main magnet which we need to know very accurately. A direct current non-ferrous superconducting septum magnet is used[48]. To trap the inflector fringe field, a superconducting shield, made of type II superconducting material, is added around the magnet.

The position of the inflector in the storage ring is shown in Figure 3.4 and the cross section of the inflector is shown in Figure 3.5.

During the powering of the main magnet to the full current of about 5200 A, the inflector is not in a superconducting status. Hence the magnetic flux goes through the shield. The magnetic field is about 1.45 T inside the inflector. Then the inflector is cooled down and both its coils and shield become superconducting. Currents of about 2700 A are applied to the coils to cancel the magnetic flux inside the inflector from the main magnet. The large change of the magnetic field is trapped inside the inflector by the internal eddy cuurents in the shield and ideally does not affect the magnetic field in the storage region which is only 7.7 cm away. However, the inflector used in 1999 had two places where the field was not fully trapped by the shield and therefore the residual fringe field of the inflector affected the magnetic field in the storage region.

- One place is at the injection point in azimuth and 7.7 cm away from the center of the storage region in radial direction. Because the inner coil of the inflector was damaged once in one test, the shield had to be cut at this place to allow the access to the coil to repair the damage. A

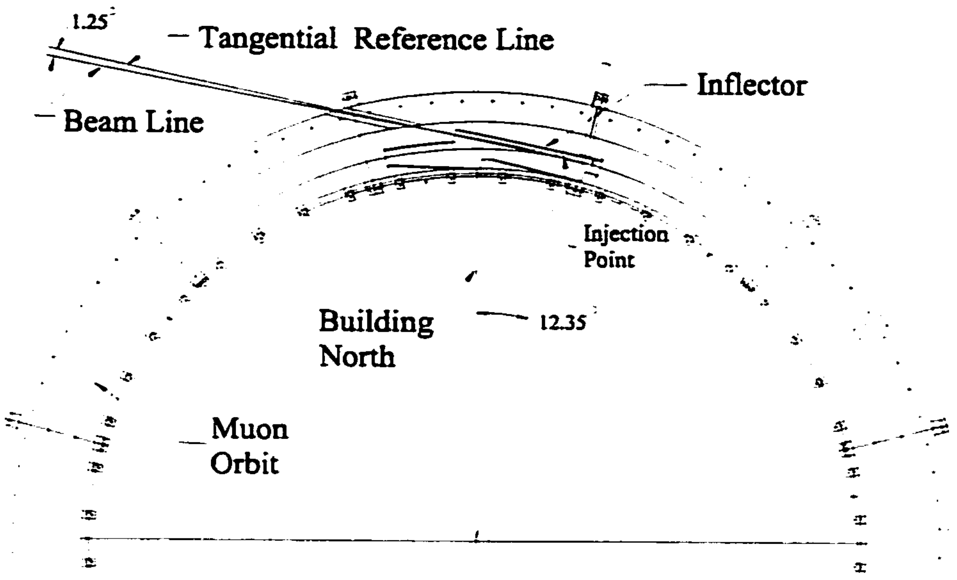

Figure 3.4: Inflector in the storage ring.

patch was used to cover the cut after repair. However, the shield is not longer a whole piece and there are currents along the edge of the cut and the patch. Therefore, the field flux inside the inflector leaks out at this point.

- The other place is at the end of the inflector shield, 26 cm downstrean from the injection point and 11.7 cm away from the center of the storage region, where the leads of the coils come out of the shield. The two leads are 4.75cm apart in the vertical direction for about 2cm before their separation is reduced to 6-7mm between the coil centers. The currents in the leads create a dipole field which influences the field in the storage region.

The inflector fringe field reduces the storage ring field by about 600 ppm at the center of the storage region, increasing to 3000 ppm at the edge of the aperture over an azimuthal angle of 1°. The large field inhomogeniety makes the measurement with NMR probe difficult in this location.

3.4 Muon Storage Ring and Magnet Shimming

The muon storage ring magnet[49] is a single continuous superferric magnet. It is 7.11 meter in radius, and "C" shaped with the opening facing towards the circle center because the decay positrons, with lower energy than stored muons, are bent inward by the magnetic field. A photograph of the ring is

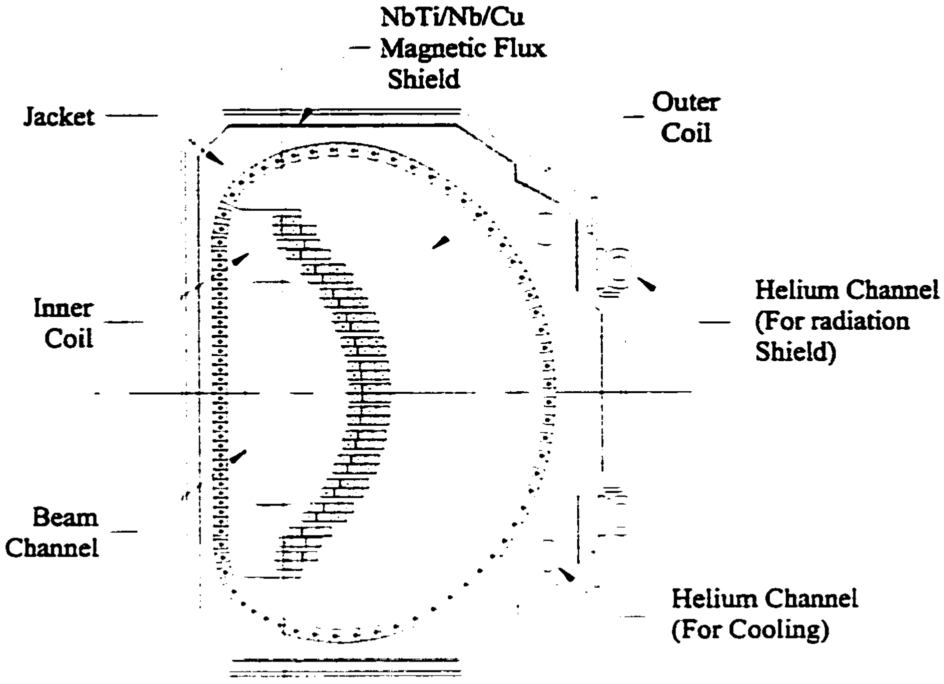

Figure 3.5: Inflector cross section.

shown in Figure 3.6 and the cross section is shown in Figure 3.7. The whole magnet consists of twelve 30° yoke sections which are made of conventional quality steel 1006 (0.07% carbon content). The yokes are named A to L along the beam direction with the A at the inflector location. There are three pole pieces, each 10° or about 124 cm long, on both top and bottom surfaces of each yoke. Between the pole pieces and the yokes, there are wedge-shaped air gaps with a larger air gap on the outer radius, closest to the iron return of the C magnet. Its slope serves to compensate for the gradient due to C magnet asymmetry. These air gaps sufficiently isolate the precision poles from the yoke returns so that field aberations, or multipoles about the dipole terms, are minimally affected by reasonable variations in the yoke reluctance. Since the poles dominate the field aberations, very pure continuous cast steel is used for their construction. This material is typically of 0.004% carbon content.

The magnet is excited by three ring-shaped superconductiong coils, as shown in Fig. 3.7, operating at a current of about 5200 A, and produces a $\sim$ 1.45 T magnetic field. The superconducting coils provide the following advantages : thermal stability once cold; relatively low power requirements; the

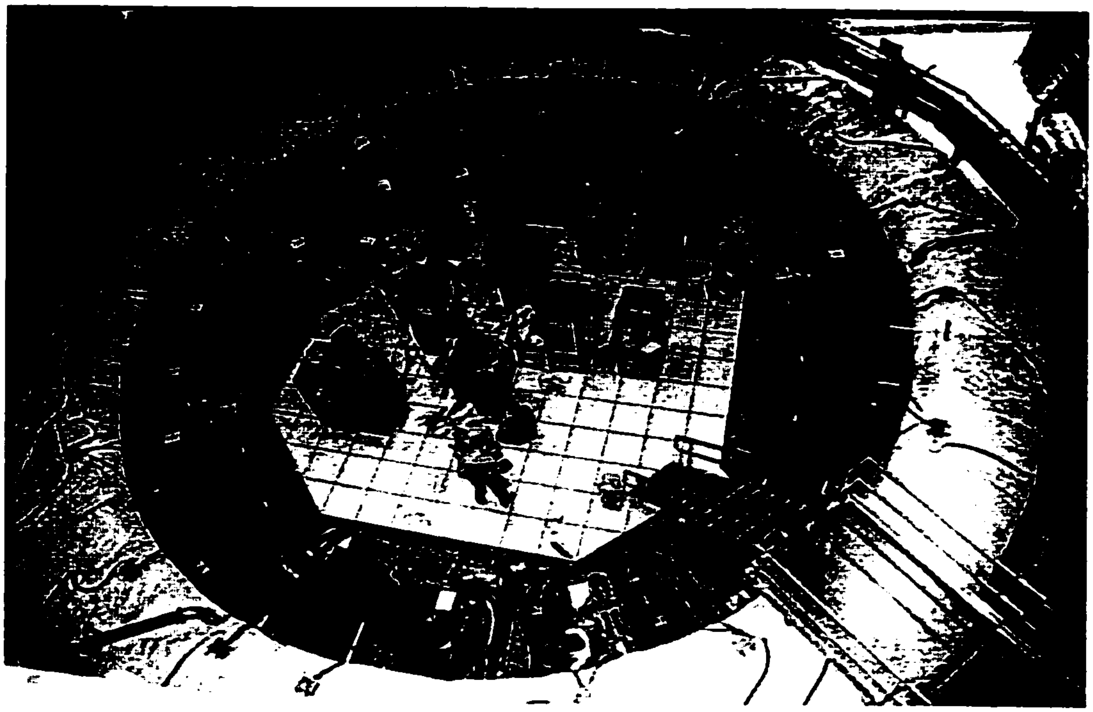

Figure 3.6: Photograph of the muon $g-2$ storage ring with the thermal insulator.

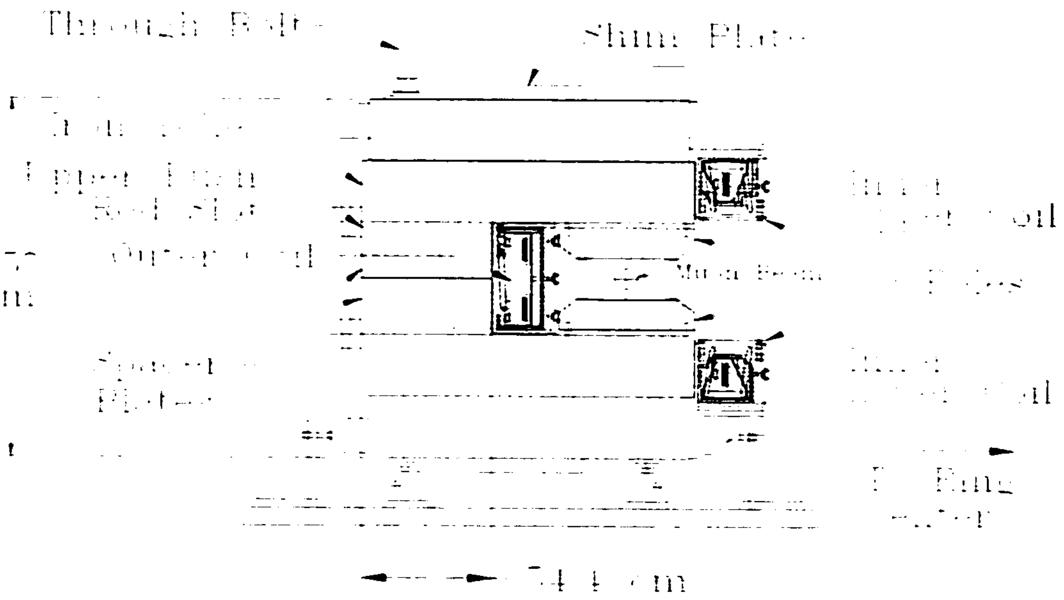

Figure 3.7: Cross section of the storage ring magnet.

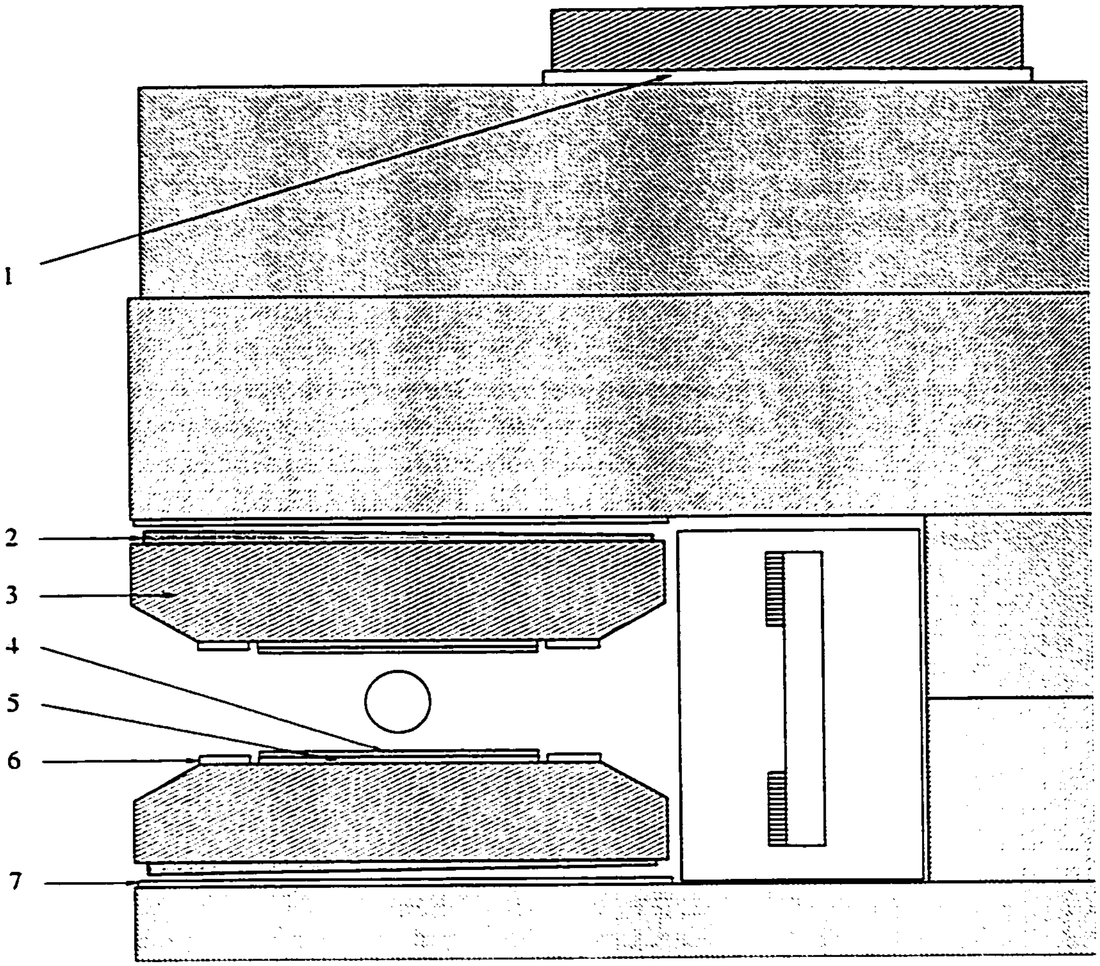

Figure 3.8: The shimming tools of the magnet. 1. aluminum or iron shims between top and bottom iron plates and the main body of the yoke: 2. iron wedges; 3. tilting poles: 4. iron strips sandwiched by aluminum boards: 5. surface correction coils: 6. edge shims: 7. dipole correction coils.

use of a well regulated low-voltage hing-current power supply: high L/R time constant value and hence low ripple currents: and thermal independence of the coils and the iron.

To achieve the required homogeneity of the magnetic field. many shimming methods were used as shown in Fig. 3.8.

- The aluminum shims between the main body of the yokes and the iron plates on them were adjusted to change the field in azimuth over a section of the yoke.

- The top poles are tilted by 200 μrad and the bottom poles are titled by 100 μrad with respect to the horizontal plane so that both the top and bottom poles would be horizontal after the magnet is powered to full current.

- In the air gap between the yokes and the poles, there are iron wedges, each of which is about 10 cm wide in the azimuthal direction and about 1 m long in radial direction. They can be individually moved in the radial direction to adjust the magnetic dipole moment. Measurement shows that 1 mm movement of the wedges leads to an 18 ppm FWHM change in dipole field over an azimuthal range of $\sim 10^\circ$.

- Dipole correction coils are also located in the air gaps for each 10° interval both above the top poles and below the bottom poles. The top and bottom coils at the same azimuth are connected in series to a single power supply. The 72 coils are powered by 36 independent power supplies. Both the iron wedges and the dipole correction coils significantly change only the dipole moment of the magnetic field and have an effect over a large azimuth of $\sim 10^\circ$.

- Removable edge shims, each of which is an iron strip 5 cm wide and 10° long in azimuth, are located on the pole surfaces. The thickness is machined to achieve the field homogeneity we needed. The edge shims are symmetrically located about the aperture center-line. Various symmetric perturbations of the shims produce predictable magnetic multipole moments.

- On the pole surfaces facing the storage ring gap, 240 wires on printboards run azimuthally around the ring in a full circle, half of them on the top poles and the other half on the bottom poles. They are called surface correction coils. These coils are next to each other in radial direction and the radial spacing between two neighbouring coils is 1/10 inch. Every 4 adjacent coils are connected in series. Currents up to 1 A can be applied to the coils to correct the low multipole moments and the field in radial direction.

- At the junctions between two ajacent poles, the magnetic field is typically smaller than at the centers of the poles. Iron strips, extended in radial direction and sandwiched by aluminum boards for mechanical stability, were glued on the poles near the junctions and on the junctions to increase the magnetic field.

To reduce the field fluctuation due to day-night temperature change, thermal insulation was installed to cover both the yokes and poles as shown in Fig. 3.6.

Vacuum chambers with a height of 18 cm were intalled in the storage ring gap between top and bottom poles. Muons orbit in those chambers during the data taking.

3.5 Magnetic Field Measurement

The magnetic field is determined by measuring the nuclear magnetic resonance (NMR) frequency in the magnetic field[50]. The Hamiltonian for a nucleus with magnetic moment $\vec{\mu}$ in a magnetic field $\vec{B} = (0, 0, B_0)$ is

$$H = -\vec{\mu} \cdot \vec{B} = -\gamma_I \hbar \vec{I} \cdot \vec{B} = -\gamma_I \hbar I_z B_0, \tag{3.9}$$

where γ_I is the gyromagnetic ratio and I is the spin of the nucleus. In the case of the proton with spin 1/2, there are two energy eigenstates separated in energy by

$$\Delta E = \hbar \omega_L, \qquad \omega_L = \gamma_I B_0, \tag{3.10}$$

where ω_L is the Larmor frequency. In a macroscopic sample of N nuclei the sum of the magnetic momenta in thermal equilibrium is

$$\vec{M}_0 = \sum_{i=1}^{N} \vec{\mu}_i = \frac{N\hbar^2\gamma_I^2 I(I+1)}{3kT} \cdot \vec{B}. \tag{3.11}$$

The time evolution of the expectation value $<\vec{M}>$ can be calculated using classical equations of motion since the value is a macroscopic quantity. In thermal equilibrium the magnetization $\vec{M}$ is aligned with respect to the external magnetic field to minimize the total energy. When a circular polarized high frequency field perpendicular to the static magnetic field is applied, the magnetic field exerts a torque on the particle

$$\vec{\tau} = \vec{M} \times \vec{B}, \qquad \vec{B} = (B_1 \cos(\omega t), \ -B_1 \sin(\omega t), \ B_0), \tag{3.12}$$

which changes the magnetization $\vec{M}$

$$\frac{d\vec{M}}{dt} = \gamma_I \vec{\tau}. \tag{3.13}$$

In a coordinate frame, x', y' and z' as shown in Fig. 3.9, which rotates with frequency $\vec{\omega} = (0, 0, -\omega)$, the change of the $\vec{M}$ is

$$\frac{\partial \vec{M}}{\partial t} = \gamma_I \vec{M} \times \left(\vec{B}_r - \frac{\vec{\omega}}{\gamma_I}\right) = \gamma_I \vec{M} \times \vec{B}_{eff}, \tag{3.14}$$

where $\vec{B}_r = (B_1, 0, B_0)$ and $\vec{B}_{eff} = (B_1, 0, B_0 - \frac{\omega}{\gamma_I})$. In the resonance case $\omega = \omega_I = \gamma_I B_0$, the z' component of $\vec{B}_{eff}$ vanishes and $\vec{M}$ rotates about the x'-axis with frequency $\omega_1 = \gamma_I B_1$. If a high frequency magnetic field is applied for a time t, $\vec{M}$ is rotated by an angle

$$\alpha = \gamma_I B_1 t. \tag{3.15}$$

For a pulse duration time $t = \pi/(2\gamma_I B)$, $\vec{M}$ is turned to along the y' direction. In the non-rotating frame, $\vec{M}$ then precesses with frequency $\omega = \gamma_I B_0$ around

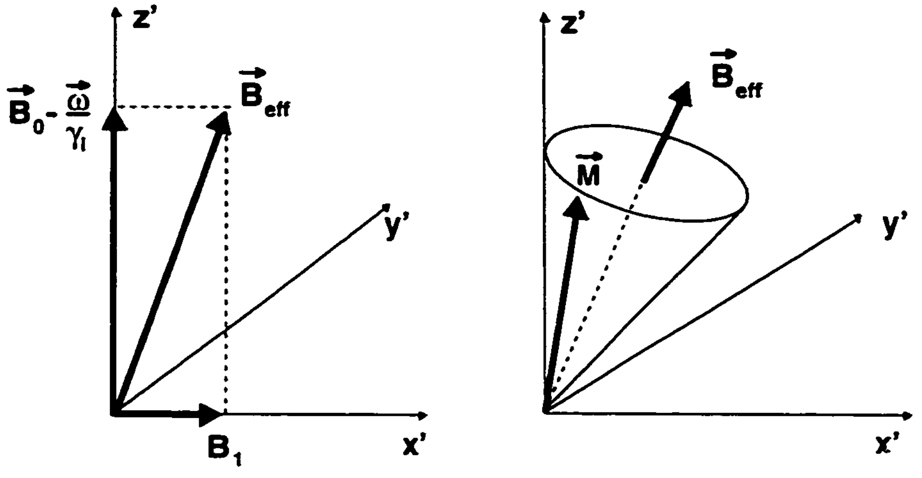

Figure 3.9: In a frame rotating with angular frequency ω, the effective magnetic field $B_{eff} = (B_1, 0, B_0 - \frac{\omega}{\gamma_I})$ as shown in the left plot. The magnetic momentum $\vec{M}$ rotates around $\vec{B}_{eff}$ as indicated in the right plot.

the static magnetic field $\vec{B} = (0, 0, B_0)$. In a complete description of the time evolution of $\vec{M}$, relaxation effects, which drive the magnetization back to its thermal equilibrium value, must be considered. The behavior of $\vec{M}$ is described by the Bloch equation

$$\begin{aligned} \frac{dM_z}{dt} &= \frac{M_0 - M_z}{T_1}, \\ \frac{dM_{x,y}}{dt} &= \gamma_I(\vec{M} \times \vec{B})_{x,y} - \frac{M_{x,y}}{T_2}, \end{aligned} \tag{3.16}$$

where T_1 and T_2 are time constants for the decay of parallel and orthogonal components of $\vec{M}$. For proton magnetization in pure water at room temperature, T_1 and T_2 are about 3 seconds which corresponds to a natural line width of $2\pi \times 0.1$ Hz[51]. Since a measurement of about 1 ms is sufficient to reach an accuracy of 0.05 ppm per measurement, the length of the NMR signals was reduced to increase the repetition rate by disolving $CuSO_4$ in the water sample[50]. A Cu^{2+} concentration of about 1.5×10^{19} cm^{-3} leads to relaxation times of about 30 ms. The NMR signals with frequency of $f_p \approx 61.79$ MHz in our experiment are mixed with a reference signal, which normally has a frequency of $f_{\text{ref}} = 61\ 740\ 000$ Hz, to obtain beat signals with a frequency of $f_p - f_{\text{ref}}$. The corresponding magnetic field to f_{ref} is called $B_{\text{ref}} \approx 1.45\ T$. Such a beat signal is referred to as a FID (free induction decay) signal in this experiment. An example of a FID signal is shown in Fig. 3.10. Because of the finite size of the NMR probe and field inhomogeneities, nuclei at different positions in the probe have different Larmor frequencies and precess out of phase. Hence, the envelope of the NMR signal deviate from an exponential function.

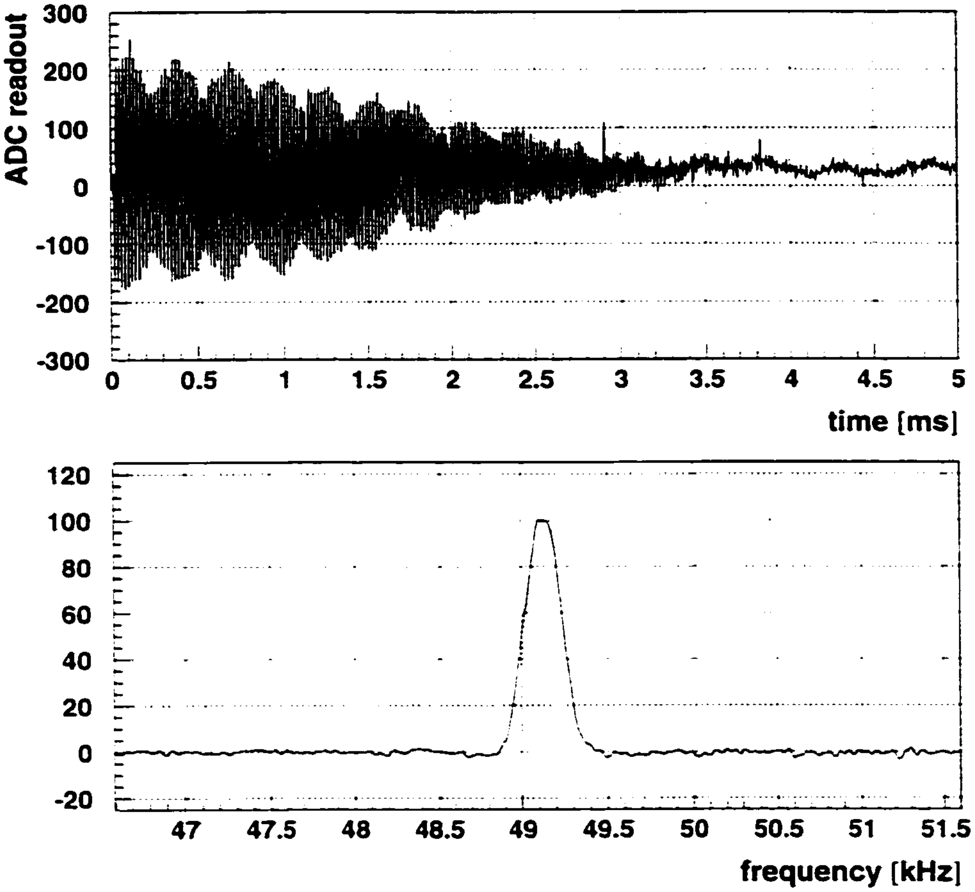

Figure 3.10: The top plot shows a digitized FID signal. The digitization rate is 200 kHz and the frequency of the signal is about 50 kHz. The beat between the FID signal and and digitization is seen. The bottom plot shows the Fourier transformation of the FID signal.

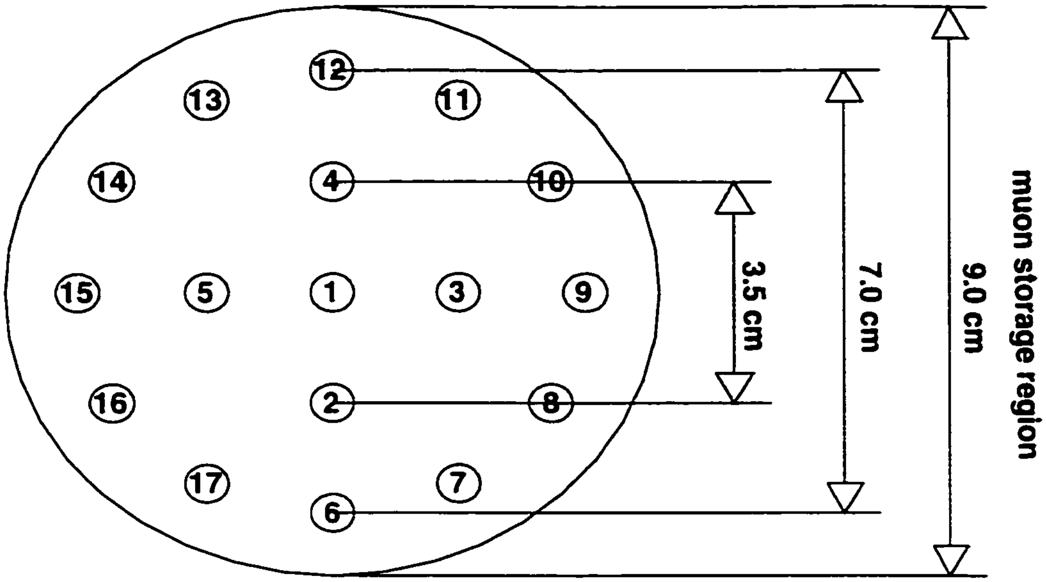

Figure 3.11: Cross sectional view of the trolley. The numbered circles show the positions of the 17 NMR probes in the trolley.

The frequencies of the FID signals are directly measured in our experiment. For convenience, the magnetic field in this experiment is defined relative to $B_{\rm ref}$ as follows

$$B = \frac{B_{\rm real} - B_{\rm ref}}{B_{\rm ref}} = \frac{f_{\rm FID}}{61.74\text{MHz}}. \qquad (3.17)$$

where $B_{\rm real}$ is the value of the magnetic field. The unit ppm(10^{-6}) is used for B.

The magnetic field measurement system consists of two parts. One is the trolley, a vacuum-tight vessel with cylindrical shape, and its calibration devices. The other is a system with 378 NMR probes embeded in the outer side of the vacuum chamber wall above and below the beam storage region.

The trolley[50] is ~ 0.5 m long, curved with the same radius as the storage ring. There are 12 wheels on the trolley which run on rails in the vacuum chamber. Seventeen NMR probes were placed in the trolley as shown in Fig 3.11 at same location along the trolley length axis. The construction of these NMR probes is shown in Fig. 3.12. The proton NMR frequency was measured by a pulsed NMR magnetometer described in detail in [52, 53, 50] and shown in Fig. 3.13. The nuclear spins of the water sample in the probe are excited by an RF-pulse of 5 W and 10 μs length applied to the resonance circuit formed by the 2 coils with inductances L_s and L_p and a capacitance C_s of the Al tube and a metal electrode. The RF-pulse produces a linearly polarized RF-field $\vec{H}$ in coil L_s. One of its circularly polarized components rotates the magnetization by 90°. The NMR signal from the processing magnetization was picked up by

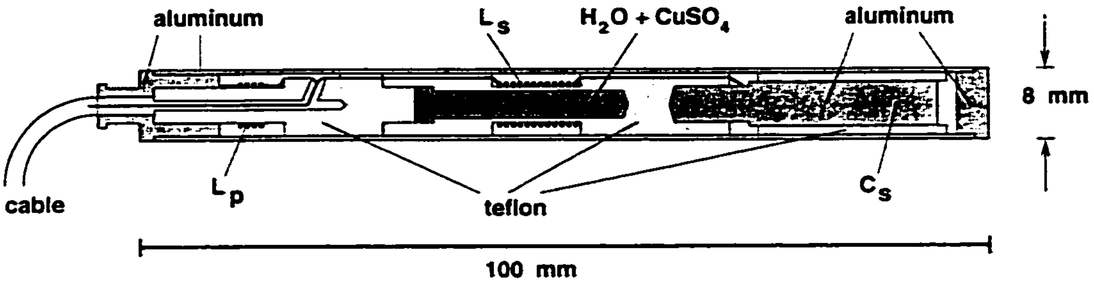

Figure 3.12: NMR probe.

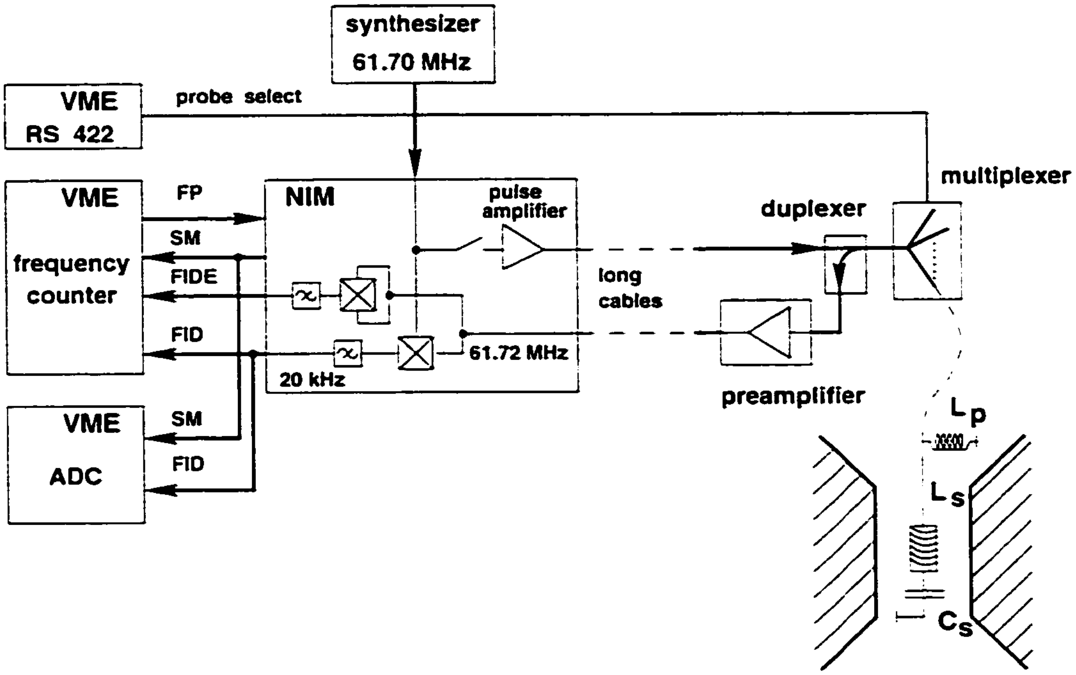

Figure 3.13: NMR magnetometer.

the same resonance circuit and transmitted by a duplexer to the input of a low noise preamplifier. The amplified NMR signal was mixed with the reference signal from a synthesizer and the beat signal was selected by a low pass filter and further amplified. The frequency f_{FID}, which is about 50 kHz, is measured with a frequency counter. The magnetic field values are determined in units of ppm as in Eq. 3.17 from the measurements of 17 probes. The NMR measurement gives the absolute value of the magnetic field B, not its direction. However, the radial and longitudinal components are less than 10^{-4} times the absolute value. Hence. $B = B_y$, where y refers to vertical direction. The error caused by this approximation is negligible in our experiment. The field can be expanded in 2-dimension

$$B(x, y) = B(r, \theta) = B_0 + \sum_{i=1}^{4} a_i \left(\frac{r}{r_0}\right)^i \cos(i\theta) + \sum_{j=1}^{4} b_i \left(\frac{r}{r_0}\right)^j \sin(j\theta), \quad (3.18)$$

where x is the radial direction in our ring, and (r, θ) are polar coordinates. The center of the storage region is at $r = 0$ and the direction pointing outward is $\theta = 0$. The value of r_0 is arbitary and to which both the normal multipoles. a_i, and the skew multipoles. b_i, are normalized. In our experiment. we choose $r_0 = 4.5$ cm which is the radius of the storage aperture in our ring. The 17 field measurements from the 17 trolley probes are used to determine the dipole moment B_0 and other multipoles a_i and b_i.

The trolley is pulled by two cables. one on each side. One cable is also used to send and recieve the signals to and from the electronics inside the trolley. The two cables extend out from the vacuum chamber through a thin pipe and were wound on two drums in an aluminum box. The box is located just downstream from the beam injection point into the ring and about 2 m from the storage region inside the ring. The drums are rotated by two motors in the box and pull the trolley in the azimuthal direction. Two potentiometers are attached to the drums. The measurements of the potentiometer resistances give the cable length and hence the azimuthal position of the trolley. The whole system is operated in vacuum. While muons are stored in the ring. the trolley can be parked at 270° downstream from injection point and away from the beam region but inside the vacuum. This enables us to make the trolley measurements frequently. In the 1999 run. the trolley was used to measure the magnetic field within the storage region about twice a week.

The calibration of the trolley probes was done with respect to a calibration probe shown in Fig. 3.14. This calibration probe can be mounted on a stand and plunged into the vacuum and moved in radial and vertical directions to measure the field at different positions and it is called the plunging probe. The plunging probe and some of the trolley probes were calibrated with respect to a standard NMR probe (Fig.3.15), which was constructed to measure the NMR frequency of protons in a spherical sample of pure water with a systematic uncertainty of 0.04 ppm[54]. The relation between the proton NMR frequency

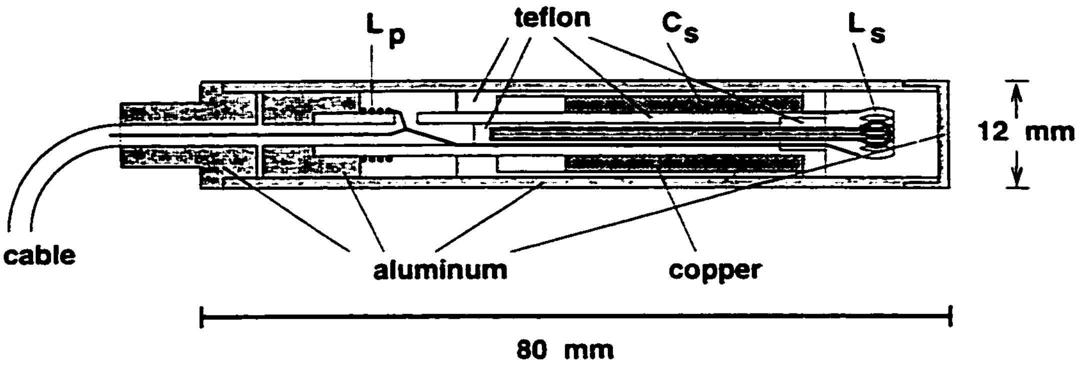

Figure 3.14: Calibration NMR probe.

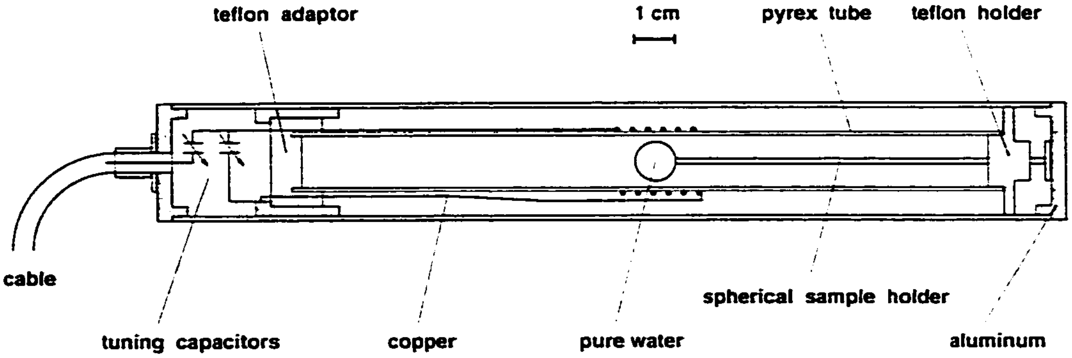

Figure 3.15: Standard NMR probe.

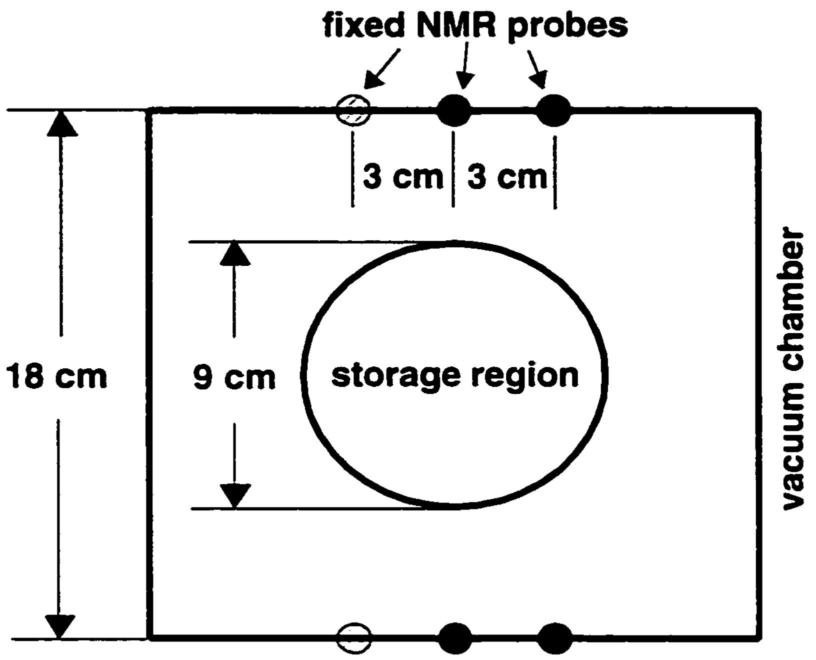

Figure 3.16: Positions of the fixed probes. At some azimuthal locations, the 6 probes are used. At other locations, only 4 probes (filled circles) are used.

in water and the free proton NMR frequency is

$$\omega_p(\text{spherical water}) = \omega_p(\text{free proton}) \times (1 - \sigma_{H_2O}) \qquad (3.19)$$

where the diamagnetic shielding factor of water $\sigma_{H_2O} = 25.790(15) \times 10^{-6}$ at $34.7°C$[55], and $d\sigma_{H_2O}/dT = 10.36(30) \times 10^{-9}\ °C^{-1}$[56].

Between trolley measurements, the change of the field is measured by 378 NMR probes (called fixed probes) which were embedded in the upper and lower walls of the vacuum chamber every 5° in azimuth. The radial and vertical positions of these probes at one azimuthal location are shown in Fig. 3.16. The structure and the magnetometer of the fixed NMR probes are the same as those of the trolley probes shown in Fig. 3.12 and Fig. 3.13. The RF-pulse used to rotate the nuclear spin is 10 W in power and 7 μs long in duration.

To reduce magnetic field fluctuations, the average readings of 36 uniformly distributed fixed probes are maintained to 0.1 ppm by feedback to the main magnet power supply. The feedback is turned off during the trolley measurements.

3.6 Muon Kicker

The particles injected into the ring through the inflector will come back to almost the same point and get lost by hitting the inflector. To avoid this loss, the particles need a "kick" to put them onto the storage orbit. In muon injection, a 10 mrad kick is provided by magnetic kickers[57]. Three identical 1.7 m long one-loop kicker sections, each consisting of 95 mm high paralled plates on either side of the beam, were put at about 90° downstream from the injection point (see Fig. 3.2). The current pulse through the plates was formed by an under-damped LCR circuit, which delivers a current pulse of 4500 A with a voltage of 95 kV. The magnetic field created by this current pulses was measured in a test setup using the Faraday effect : the phenomenon that a changing magnetic field will result in a time dependent rotation of the polarization vector of a laser beam when it transits a dielectric material. The result is shown in Fig. 3.17. Since the cyclotron period of the beam in our storage ring is $\sim$ 149 ns, the beam is kicked several times before the kicker pulse died out. The injection efficiency with the capacitor voltage at 95 kV is $\sim$ 7%, close to the ideal maximum injection efficiency of 7.5%. With muon injection, the number of detected positrons per hour was increased by an order of magnitude compare to poin injection. Furthermore, the injection-related background in the positron detectors was reduced by a factor of about 50 since most of the pions were removed from the beam before entering the storage ring. The perturbation on the fixed NMR probes readings caused by the the kicker currents is negligible. The residual eddy currents in the vacuum chamber walls has a small effect on the magnetic field and will be discussed in Sec. 5.8.

3.7 Electrostatic Quadrupoles and Colimators

The muon beam in the storage ring was focused horizontally by the uniform magnetic field and vertically by electrostatic quadrupoles[58] Q1, Q2, Q3 and Q4, which are distributed around the ring as shown in Fig. 3.2. The use of a muon beam with $\gamma = 29.3$ (magic gamma) eliminates the effect of electric field on ω_a. For vertical focusing we used an average field index

$$n = -\frac{r_{\text{magic}}}{\beta B}\frac{\partial E_r}{\partial r} = 0.137. \tag{3.20}$$

where $r_{\text{magic}} = 711.2$ cm is the radius of the central orbit, $\beta = v/c \approx 1$, $B = 1.45$ T is the magnetic field at the central orbit, and E_r is the radial electric field. For this n value, the wavelength of the betatron oscillation is $1/\sqrt{1-n} = 1.08$ turns (orbit circumference) for the horizontal motion and $1/\sqrt{n} = 2.72$ turns for the vertical motion.

The cross section of the vacuum chamber with the electrostatic quadrupoles is shown in Fig. 3.18. The aluminum electrode plates are 4.7 cm wide, and the

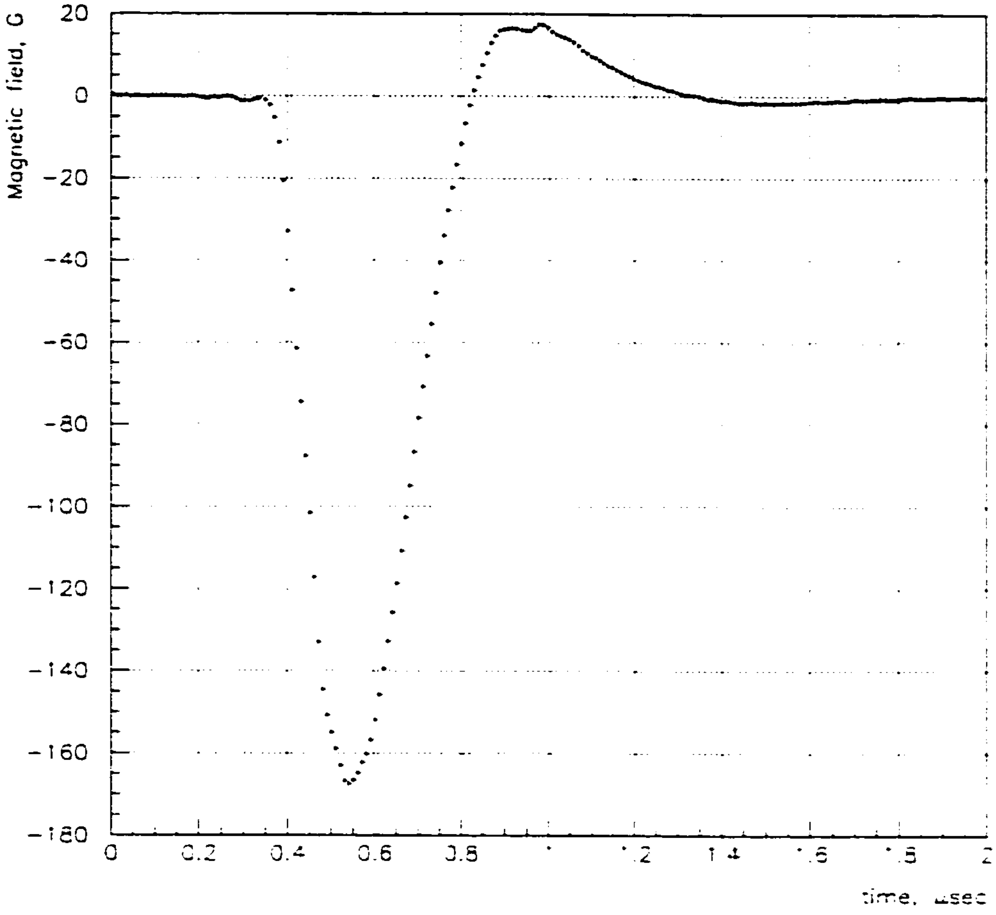

Figure 3.17: The magnetic field created by the pulsed current in the kicker. This magnetic field is measured by the Faraday effect.

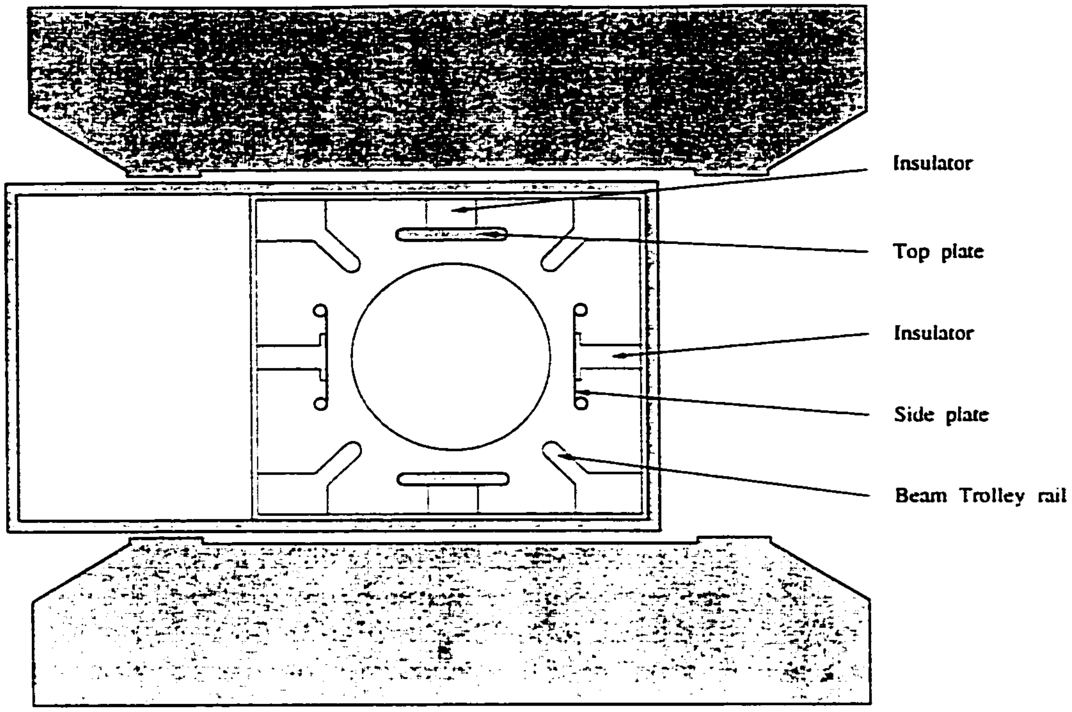

Figure 3.18: Cross-sectional view showing the electrostatic quadrupoles.

spacing between them is 10 cm. The positions of the vacuum chambers relative to the poles is accurate to about 0.5 mm. The field index $n = 0.137$ requires a voltage V=10.6 kV/f, where $f = 43\%$ is the fraction of the ring covered by the electrostatic quadrupoles, and hence V=24.5 kV. The high voltage is pulsed on only for $\sim$ 1 ms when muons are stored in the ring to avoid electrical breakdown.

In the vacuum chamber, eight copper rings (collimators) with inner radius of 4.5 cm, outer radius of 5.5 cm, and thickness of 3.2 mm, are used to scrape the edge of the muon beam. Six of them are full rings. The collimator which is located near 180° in azimuth away from the injection point is a half ring with the opening facing towards the storage ring center. The collimator which is located near the injection point is a half ring with the opening facing outwards from the storage ring center. The choice of half rings avoids scraping the beam in the first few turns when the beam is not yet fully kicked onto the storage orbit. The positions of collimators are accurate to 0.5 mm with respect to the vacuum chamber. The combination of collimators and electrostatic quadrupoles defines the position and shape of the beam. During the first 16 μs after injection, the voltages on the quadrupole plates are asymmetric and the muon beam is scraped on the edge. In vertical scraping, the lower quadrupole plates are charged to 17.5 kV, 7 kV lower than the voltage on the upper plates, and the beam is placed about 2.5 mm below the center of the collimator. In horizontal scraping, the voltages on the outer plate of quadrupole Q2 and inner plate of Q4 are charged to -17.5 kV, 7 kV lower than the normal voltage of 24.5 kV, and the beam is displaced sideways by 2.5 mm. The scraping leads to the loss of muons at the edge of the beam, which would likely be lost in an uncontrolled manner if the beam were not scraped prior to the start of the data collection. After the scraping ends, it takes 5 μs for the voltages to equalize.

To monitor the charging and discharging of the electrostatic quadrupole, the voltage pulses applied to the plates were digitized by wave form digitizer(WFD) and recorded. The collimators are moved out of the way for trolley measurements.

3.8 Detectors

The positrons from the decay $\mu^+ \rightarrow e^+\nu_e\bar{\nu}_\mu$ have an energy spectrum extending up to 3.1 GeV and are detected with 24 detectors[59] placed symmetrically at 24 positions around the inside of the storage ring as shown in Fig. 3.2. Each detector (Fig. 3.19) consists of a Pb-scintillating fiber electromagnetic calorimeter and a horizontal array of five scintillator paddles (Front Scintillation Detector. FSD) on the front face of the calorimeter. Not all FSDs were read out in the 1999 run.

The calorimeters are used to measure the arrival time and energy of the decay positrons. They are made of 1 mm plastic scintillator fibers embedded in a lead/antimony(6%) matrix (Pb/SCIFI). The fibers were oriented radially with respect to the storage ring such that high energy decay positrons enter the calorimeters nearly perpendicular to the fibers. The radiation length of the calorimeters is about 1 cm. Each calorimeter is 22.5 cm wide. 14 cm high, 15 cm deep, and consists of four separate segments glued together. These parameters were chosen to minimize the background from low energy side-entering decay positrons. while maximizing shower containment. To each segment was glued a Lucite light guide which transports the light to a photomultiplier. The energy resolution of the calorimeters is $\sigma_E/E = 6 - 9\%$ for the energy range $E = 1 - 3$ GeV.

The front scintillation detectors consist of five 2.8 cm wide. 23 cm long and 9.5 mm thick. radially oriented scintillator slabs. Together. five slabs cover the entire front face of the calorimeter and provide information about the times and vertical positions of the incidence of positrons, muons or protons.

To measure any timing shift during the measurement, a N_2 laser system was implemented. A UV laser pulse (337nm) can be delivered to each calorimeter segment through quartz fibers and produces a signal comparable in shape. but slightly narrower. to that produced by decay positrons. The same laser pulse is also sent to a reference detector. The comparison between the time and energy data from calorimeters and from the reference detector provides a timing standard and also tests the PMT gain stability. The timing calibrations by laser were done about three times per day in the 1999 run. and timing shifts over the first 200 μs were measured to be less than 20 ps on average.

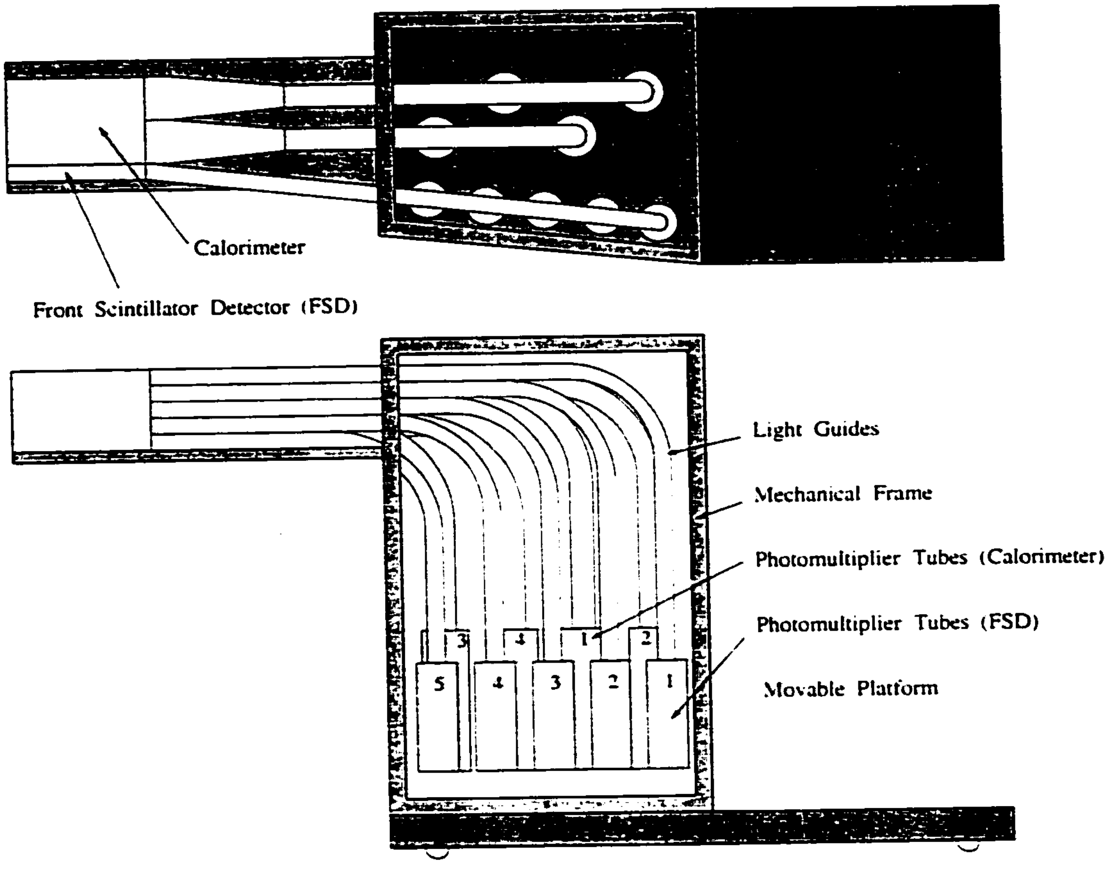

Figure 3.19: The top plot is the top view of the detector and the bottom is the side view of the detector.

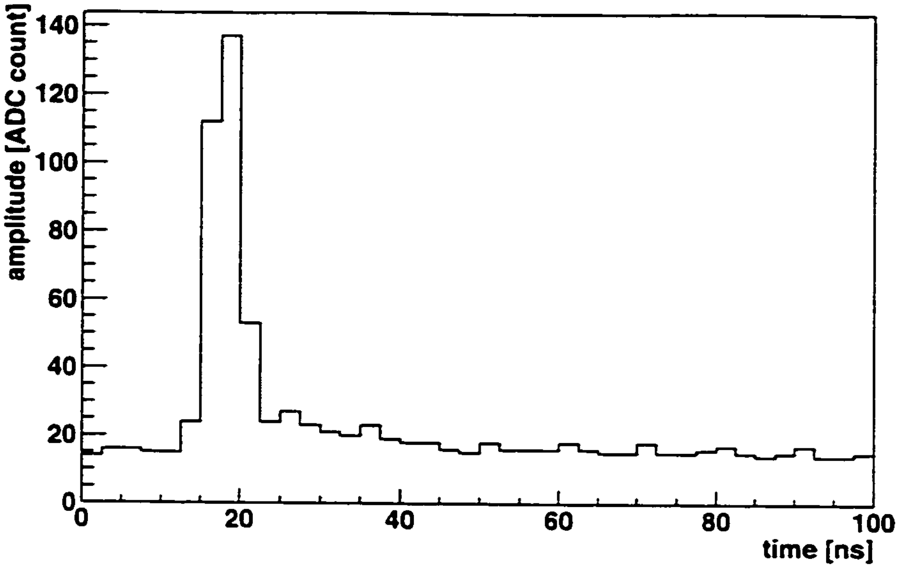

Figure 3.20: An example of a WFD signal of a positron pulse.

3.9 Detector Electronics and Data Acquisition System

The calorimeter pulses were continuously sampled by custom WFDs. The WFD is a VME bus module designed to digitize and store analog input data at a rate up to 200 MHz. With a pair of WFDs operating 180° out of phase on the same analog pulse, we can effectively sample at 400 MHz. A marker pulse was input to the WFD at the beginning of each injection to align the two WFDs. Each WFD channel has four analog inputs, corresponding to four PMTs on each calorimeter. Each of the four inputs is separately discriminated and the sum of the four is digitized by two 200 MHz, 8 bit Flash ADC. The data are transferred to the on-board memory only if the summed analog signal exceeds a programable threshold, which corresponds to 1 GeV in the absence of a baseline or so in positron energy in 1999 run. For each waveform digitized, the WFD provides at least four time bins before the threshold is crossed to permit pedestal determination and at least 32 time bins afterwards to record the whole pulse shape. An example of WFD signal of a positron pulse is shown in Fig. 3.20.

The data acquisition system consists of six front-end VME crates, containing the detector readout electronics and one central VME crate–event builder. The front-end crate CPUs read out the data from the on-board memory between each fill of the storage ring and store the data until the end of each AGS cycle. The central crate CPU reads out the data from the front-end crate

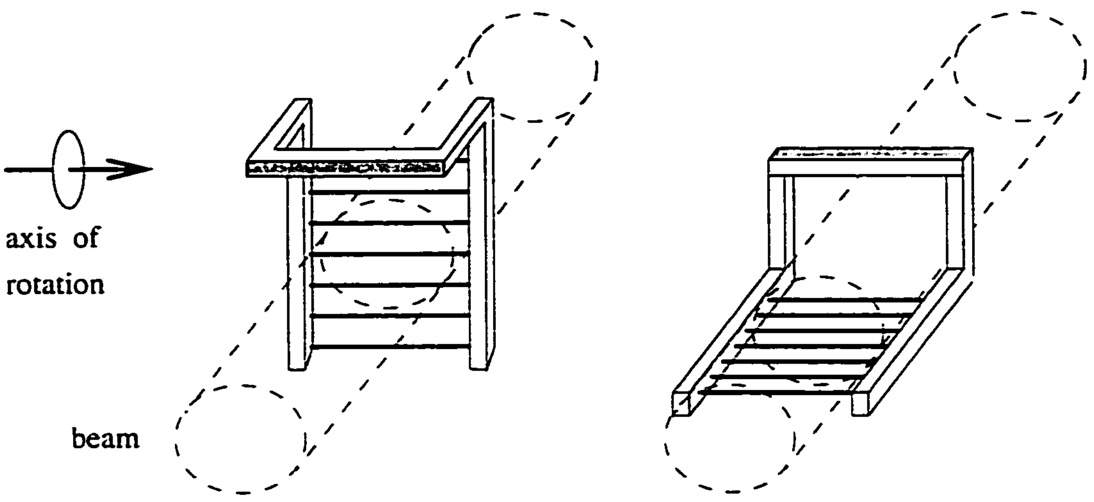

(a) measuring position (b) calibration position

Figure 3.21: Scintillating fiber detector.

between AGS cycles and writes it onto tapes.

3.10 Muon Distribution Measurement

The knowledge of the muon distribution in the storage ring is important because it is the average magnetic field weighted by the muon distribution that is needed for determining ω_p.

The decay positrons arrival times at the calorimeters shortly after the injection are used to measure the radial distribution of the beam. The muons beam are injected in 50 ns pulse and have 0.6% momentum width. Because the higher momentum muons have larger orbital radii and hence longer cyclotron periods, the beam debunches with a decay time of about 20 μs and finally fills the ring uniformly in azimuth. The positron time spectrum shortly after the injection is used to determine the muon momentum distribution which in turn determines the radial distribution of the muon beam.

Two scintillating fiber detectors are located at 180° and 270° downstream from the injection point. Each detector has two sets of seven 0.5 mm diameter fibers spaced by 10 mm in a "harp" configuration as shown in Fig. 3.21. One set of fibers is aligned in the radial direction and the other in the vertical direction. Each fiber is connected to a separate photomultiplier. The scintillating fiber detectors can be moved in and out of the storage region when muons are stored in the ring. To calibrate the fibers and PMTs with respect to one another, the "harp"s were rotated by 90° to place the fibers just downstream of each other. In this configuration, all the fibers measure the beam at the same radial and

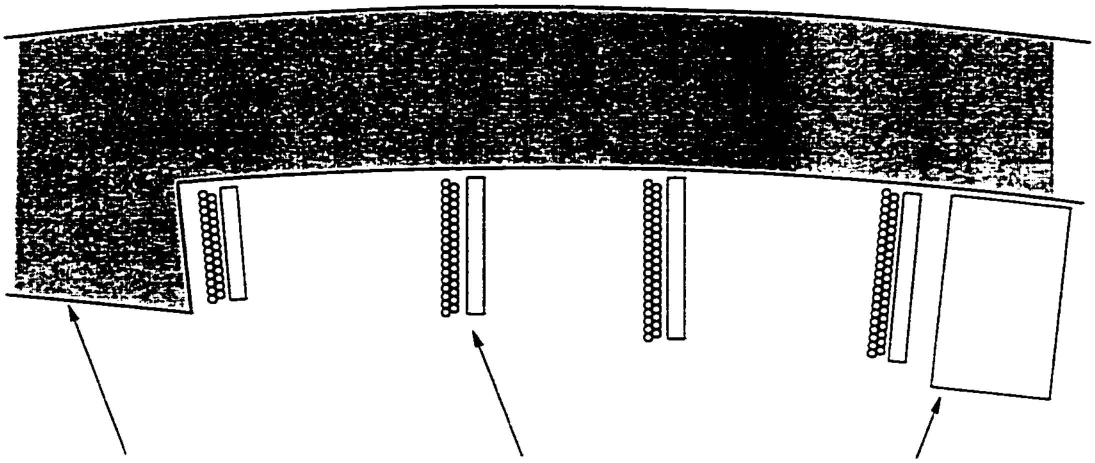

Figure 3.22: Traceback system.

vertical position as shown in Fig. 3.21(b).

The traceback system was constructed to measure the muon spatial distribution. It consists of four wire chambers (Fig. 3.22), separated by about 25 cm and measures the trajectory and momentum of decay positrons at about 300° downstream from the injection point. Each chamber consists of two layers of vertical and radial drift tubes which have a diameter of 10 mm each and are made of 25 μm thick aluminum mylar and are filled with CO_2-iso C_4H_{10} gas. The trajectory of apositron measured by the system was traced back to the point where its radial component of motion is zero. The point is typically within 1 mm in radial and vertical directions from the position of the muon decay. The traceback system was not fully operational in the 1999 run.

Chapter 4

The 1999 $g-2$ run

The cryogenic system had been operational since November 1998 and the superconducting coils were cooled down. The magnet was powered up to the full current of about 5200 A and the inflector was commissioned with a maximum current of 2800 A. The electrostatic quadrupoles and the kicker were successfully commissioned at a vacuum of 10^{-7} Torr. All the detector stations were calibrated and the data acquisition system were tested. The fiber monitors and traceback systems were installed. Data-taking started on December 19, 1998 with the magnetic field measurement. Several trolley measurements and calibrations of trolley probes were done. From December 29 1998, protons were delivered to the target in six bunches per AGS cycle and the dedicated proton beam from AGS began at the turn of the New Year of 1999. The beamline was carefully tuned to maximize the number of stored muons and minimize the background. Care was also taken in tuning the AGS ejection system to minimize background from any extraneous proton beam extracted later during the muon storage time. Online analysis of the data was made to ensure the detectors and data acquisition system operated properly. Magnetic field measurements with the trolley were taken about twice per week. The fixed probes were used to measure the field at all times. The six-bunch beam stopped on Feburary 16, 1999 and we have totally about 2000 data-taking runs. From Feburary 24 1999, proton beam was delivered in 12 bunches per AGS cycle for studies which would help us improve our statistics and systematics in future runs. The proton beam stopped on March 8, 1999. More trolley runs and calibrations of the field measurement system were done. Special trolley measurements were made covering the region near the inflector.

4.1 ω_p Measurement

The quench electronics systems of both the main magnet and the inflector were tested. The main superconducting magnet was powered up to full current, 5175 A, on December 11, 1998 after a one month long cooling precedure. The superconducting inflector was cooled down and powered up to a full current of

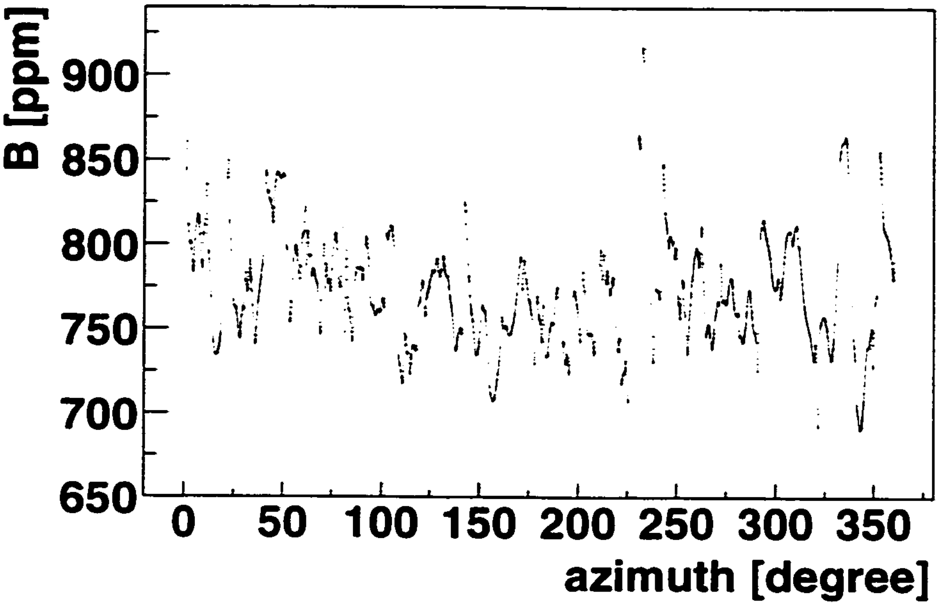

Figure 4.1: The magnetic field vs. azimuth, measured by a trolley probe. It shows a first order harmonic variation of about 50 ppm.

2700 A. The surface coil currents were applied. The current in each coil was set in a range from about -1 A to 1 A. The magnetic fields were measured by the trolley at the position of the plunging probe stand with different current settings. From the calculations and trials, an empirical formula was obtained to calculate the multipole moments of the magnetic field created by the surface coil currents, which was later used to set the surface coil currents according to our needs.

The trolley probes and plunging probe were calibrated with respect to the standard probe. The results of the calibrations were compared to the calibrations made after the 1998 run. All trolley probes except probes 3 and 8 had results which agreed within 0.2 ppm with the calibrations done after the 1998 run. Probe 3 has a difference of 0.3 ppm. Probe 8 was known to produce erroneous readings and was never used in the analysis.

Several trolley runs were taken to measure the average magnetic field over azimuth. The surface coil currents were set so that the multipole moments, especially the quadrupole moments, of the average magnetic field in azimuth were minimized. The quadrupole moments were about 2.3 ppm at the aperture of the storage region, 4.5 cm away from the center. The trolley runs shortly after the power-up showed a large first harmonic variation of the magnetic field in azimuth as shown in Fig. 4.1. This is caused by the small movement of the superconducting coils of the magnet during the warming up and cooling down, and by the temperature distributions over the iron yoke. This variation moves our muon beam. Under the assumption that the field has an Nth harmonic field variation in azimuth, let b_0^N be the amplitude of this variation as a fraction of the main field, and x denotes the radial distance of a muon from its equilibrium orbit of radius ρ_0. Then

$$\frac{d^2x}{d\theta^2} + (1-n)x = -b_0^N \rho_0 \cos(N\theta) \tag{4.1}$$

gives

$$x = \frac{b_0^N \rho_0}{N^2 - 1 + n} \cos(N\theta), \tag{4.2}$$

where θ is the azimuthal angle and n is the field index determined by the focusing electric field of the electrostatic quadrupoles. If the normal quadrupole moment of the field, dB/dx, has the same order harmonic variation with amplitude b_1^N, measured at the edge of the aperture $r_0 = 4.5$ cm as a fraction of the main field, then the field seen by the muon will differ from the main field by

$$dB = b_1^N \frac{x}{r_0} \cos(N\theta). \tag{4.3}$$

Substitution of Eq. 4.2 gives the change in the average field

$$\Delta B = \frac{b_0^N b_1^N \rho_0}{2r_0(N^2 - 1 + n)}, \tag{4.4}$$

where the factor 2 in the denominator comes from averaging $\cos^2(N\theta)$ around the azimuth. Because of the N^2 in the denominator, the first harmonics are most important. The above calculation holds when both harmonics are in phase. The calculation shows that 50 ppm of the first harmonic field variation in azimuth will move the beam by 1 mm. In our experiment, the normal quadupole moments are in the range of ±30 ppm at the aperture of 4.5 cm. To eliminate this field variation, the iron wedges located at $150^\circ - 360^\circ$ downstream from the injection point were moved on January 3 and 6. The trolley runs taken afterward show a first harmonic variation in the field less then 20 ppm.

During the data-taking period from January to early March, 17 successful trolley runs were made, typically every 3 data-taking days apart. During the trolley runs, the 17 trolley probes were read out typically every 2 seconds during which the trolley moves about 1 cm. Two cables attached to either side of the trolley allow us to pull the trolley in both directions. In most of the trolley runs, the trolley was moved in the same direction as the beam because it moved more smooth in this direction. The opposite direction was also used to check possible errors on the readings of the trolley position due to the force on the cables. The trolley runs normally took 2 hours to complete and another hour to move the trolley out of and back to the trolley garage. Due to the fringe field of the inflector, there is a large magnetic field inhomogeniety in the region near the inflector. This large inhomogeniety makes the NMR signal decay so rapidly that the signal decayed below the threshold before we start the measurement. For the outer part of the storage region, the inflector fringe field decreases the field so much that the NMR signals have roughly the same frequency as the normal reference frequency of 61.74 MHz instead of about 50 kHz higher. Hence, the beat between the NMR signal and the reference has a too long period and cannot be measured before it decays away. Hence, all trolley probes failed to measure the field in some parts of the inflector region during normal trolley runs. The outer probes, which are closer to the inflector, failed in a larger region than the inner probes did. To measure the magnetic field in this inhomogeneous field region, nine of the 17 trolley runs were immediately followed by a separate inflector measurement which only measured the field in the region close to the inflector with special electronic settings applied to the trolley probes. This setting started and stopped the NMR frequency measurement earlier, and hence the readings covered most of the region which could not be measured in normal trolley runs. A separate inflector measurement normally took one half hour. However, there are regions in which the field could not be measured even in the separate inflector runs, as was typically the case for probes 1, 3, and 7-12. At the end of the 1999 run, we made a special inflector region measurement in air with a different set of probes connected to one of the fixed probe NMR units. The fixed probe unit allows us to use a larger amplitude for the excitation pulse and earlier starting times for the measurement than the settings possible with the trolley in vacuum. We also changed the reference frequency and got beat signals with frequencies of about 50 kHz. This special inflector measurement covers the whole inflector region for all probes. The separate inflector measurements and the special measurement at the end of the run were both used to supplement the normal trolley runs in the analysis.

Between trolley runs, the magnetic field was measured by 378 fixed probes embeded in the outer top and bottom walls of the vacuum chambers as shown in Fig. 3.16. The fixed probes were divided into 20 groups according to their azimuthal positions. Each group consisted of 14–20 probes. The signals from the fixed probes in one group were sent to one of 20 multiplexer modules. The probes connected to one module measured the field in a sequence which is repeated every 20 measurements. Hence, some probes in a module which reads fewer than 20 probes could measure the field more often. The time interval between two consecutive measurements was set to be 0.5 second during the normal data-taking periods and it took 10 seconds to measure the field with all the fixed NMR probes. Since sizable fluctuations of the field take at least several minutes, ten seconds is short enough to measure the field to the required accuracy. During the trolley run, the magnetic field is perturbed by the trolley passage, and the time interval between two consecutive fixed probe measurements was set to be 0.2 second so that it took 4 seconds to measure the field with all probes. This time setting allows us to measure the perturbation on the fixed probe measurements when the trolley passes. Thirty-six fixed probes, one probe at the center of each of the magnet poles, were selected and the average of their readings were maintained to 0.1 ppm by feedback to the main magnet power supply. The feedback was always turned off during trolley runs because of the perturbation on the fixed probe measurements by the passage of the trolley. After the data-taking ended, we repeated the calibration of the trolley probes with respect to the plunging probe and the standard probe.

During the run, the main magnet was ramped down to zero current five times and partially ramped down to 1500 A once to fix the trolley drive or as precautions for approaching thunderstorms. The main magnet was finally turned off on March 15 1999.

4.2 Beam Tuning

The AGS began to deliver dedicated 24 GeV proton beam to our nickel target on January 1, 1999. The period of one AGS cycle was 2.5 s and each cycle had six bunches (also called fills) separated by 33 ms. The intensity of the proton beam increased during the startup period and reached a maximum of 4×10^{13} protons(40TP) per cycle two weeks later. A secondary emission chamber (SEC) was located just before the target to measure the secondary emission due to the proton beam. This gave us a rough measurement of the beam intensity. Another secondary emission chamber was located after the target to measure the number of particles produced by the proton beam. and this measurement was sensitive to the location where the proton beam hit the target.

The pions, produced in the collisions, were selected by the dipole magnets D1 and D4 and the colimators K1 and K2, where K1 determines the upper limit on the momentum of selected pions and K2 the lower limit. In the 1999 run, we selected the pions with momenta 1.7% higher than the magic momentum of 3.093 GeV/c. The selected pions entered a 116 m long secondary beamline(as shown in Fig. 3.3), in which a fraction of $\sim$ 50% decays into muons. Along the beamline. seven segmented wire ionization chambers(SWIC) measure the beam profiles. Collimators K3-K4 select the muons with magic momentum. 1.7% lower than the pion momentum. K3 determines the upper limit on the momentum of accepted muons and K4 the lower limit. Due to parity violation, the decay muons are polarized. The polarization of accepted muons is longitudinal and about 95% in our experiment.

At the end of the beamline and just upstream of the inflector magnet. the beam composition was measured by a Čerenkov counter in the 1998 run. during which the beamline settings were similar to those in the 1999 run. The condition for the Čerenkov light production is

$$\beta = \frac{v}{c} > \frac{1}{n}. \tag{4.5}$$

where v is the speed of the particle, c is the speed of light, and n is the refraction index. For gas, the refraction index

$$n = \sqrt{\frac{1+2K\rho}{1-K\rho}}, \tag{4.6}$$

where $K = 0.3627\mathrm{cm}^3/\mathrm{g}$ for isobutane and ρ is the density of the gas. Hence, the gas density threshold for a particle to produce Čerenkov light

$$\rho_{\mathrm{th}} = \frac{1}{K}\frac{1-\beta^2}{1+2\beta^2}, \tag{4.7}$$

By stepping the pressure of isobutane from 0 to 1.2 atm, the thresholds for e^+, then μ^+, and finally π^+ with magic momentum to produce Čerenkov light were crossed. The threshold for protons is too high to be reached by our Čerenkov detector. In case of $K\rho \ll 1$ and $m^2 \ll p^2$, the yield of the Čerenkov photons

$$\frac{dN_\gamma}{dx d\lambda} = N\frac{2\pi q^2\alpha}{e^2\lambda^2}\left(3K\rho - \frac{m^2}{p^2}\right) = N\frac{2\pi q^2\alpha}{e^2\lambda^2}\left(\frac{3KM_{\mathrm{mol}}}{RT}P - \frac{m^2}{p^2}\right). \tag{4.8}$$

where λ is the wavelength of the light, and x is the track length. N is the number of charge particles passing through, q is the charge of the particle, $M_{\mathrm{mol}} = 58.1234\mathrm{g/mol}$ for isobutane, T is temperature, and P is the gas pressure. Fig. 4.2 shows the measurements of the yield of the Čerenkov light at different gas pressures. Eq. 4.8 means the slopes of the linear fits to the Čerenkov response are proportional to the number of particles which produce Čerenkov light at that gas pressure. From the measurements, the beam was found to consist of almost equal parts of positrons, muons, and pions, consistent with Monte Carlo predictions. While this measurement is not sensitive to protons in the beam because of the large mass of the proton, the calculation predicts the number of protons to be about one third of the pions. The Čerenkov counter was moved out from the beam path during the normal data-taking period to optimize the beam emittance. Downstream of the Čerenkov counter, a small wire ion chamber and photodiodes measure the beam profile at the inflector entrance.

The muons were injected into the storage ring through the inflector. The inflector current, which cancelled the magnetic field from the main magnet, was varied to achieve the best injection efficiency. In the first few turns after injection, the muons were kicked by three magnetic kickers onto stable orbits. The timings of the kicks were set with respect to the signals from AGS. This signal was linked to the RF in the AGS and therefore linked to the time when the proton beam was extracted into our beamline. The vertical position of the equilibrium orbit of the muons is determined by the balance of the electrical and magnetic force

$$f_\perp = e\beta cB_r + eE_\perp = 0. \tag{4.9}$$

where B_r is the radial component of the magnetic field and $E_\perp$ is the vertical eletrical field at the position of equilibrium orbit. The vertical electrical field

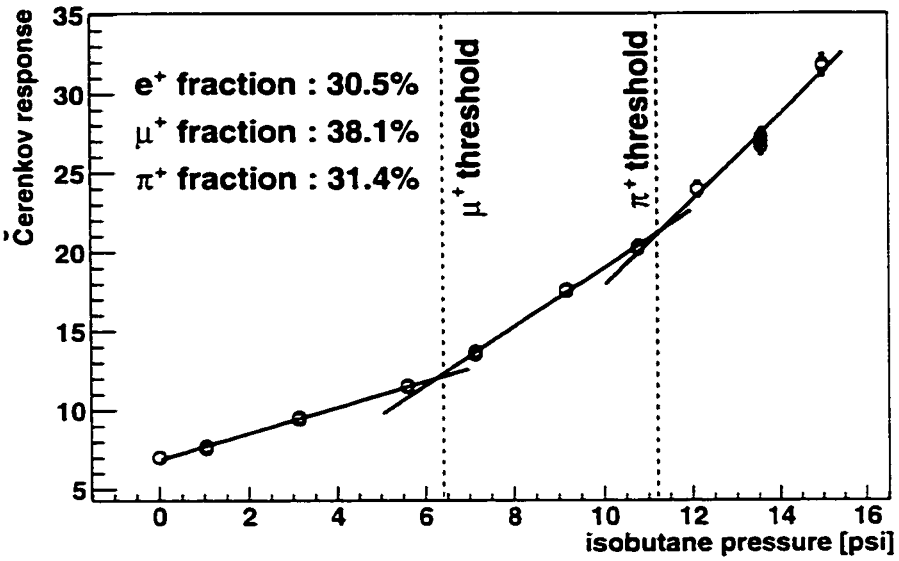

Figure 4.2: Čerenkov response (proportional to the yield of the light and in arbitrary units) versus the isobutane pressure. The dashed lines indicate the expected pressure thresholds for μ^+ and π^+ to produce Čerenkov light. The slopes of the linear fits determine the number of the particles which produce Čerenkov light, and hence the fractions of e^+, μ^+ and π^+.

was determined by the eletrostatic quadrupoles voltages set to avoid beam and spin resonances. The radial magnetic field was adjusted to move the vertical beam position.

Detectors 12 through 24, which were more than 150° downstream away from the inflector, were used to counted coincidences of signals from any two of the four segments of each calorimeter. This count, called CTAG, is regarded as a monitor of the number of stored muons. The purpose of the beam tuning was to increase the ratio of the CTAG and the beam intensity measured by the secondary emission chamber while keeping the background under control. Studies of the currents of the beamline magnets and the opening of the colimators were done and the beam profiles from the ion chambers at the optimum setting were recorded. Unexpected changes in the AGS or in our beamline magnets could significantly change the beam profiles, reduce the number of injected muons, and increase the background. The beam profiles, measured by wire ion chambers, were monitored continually and maintained at the same shapes by the tuning beam. Scans of the inflector current were done to optimize the injection efficiency. It was found that the optimum current was 2700 A with an acceptable variance of 10 A. The timing of the three kicker modules were set individually to maximize the number of stored muons. The amplitude the radial magnetic field was also optimized by adjusting the currents in the surface coils so as to maximize the number of stored muons. To minimize uncontrolled muon losses during the data collection periods, we scraped about 10% of the muon away during the first $16 + 5 = 21$ μs after the injection by setting the voltage of the quadrupole plates in an asymmetrical pattern by 7 kV (see Sec. 3.7). After beam tuning, 5×10^4 muons were stored per AGS cycle, which means 1 stored muon per 8×10^8 protons from AGS. The ratio between the CTAG and SEC was monitored online to ensure that there were no unexpected changes in the beam line and the storage ring. The beam was fine tuned many times during the run.

4.3 AGS Background

Background with the AGS period of 2.7 μs was occasionally observed in the time spectra of decay positrons. This kind of background is caused by so-called flashlet and is shown in Fig. 4.3. The AGS stored six bunches of protons and extracted one at a time. Sometimes the proton bunch was not fully extracted due to mistiming of the extraction pulse with respect to the proton bunches. The protons left in the AGS were extracted after an integer number of AGS cyclotron periods(2.7 μs)when those protons came back to the extraction point. It also happened that the proton bunches, which had not been extracted, spilled out some protons when they passed the extraction point because the extraction pulse, which extracted the previous bunch, had not yet decayed to zero. Hence, some extraneous proton beam was extracted from AGS during our muon storage time. Since we measured the time spectra of the decay positrons

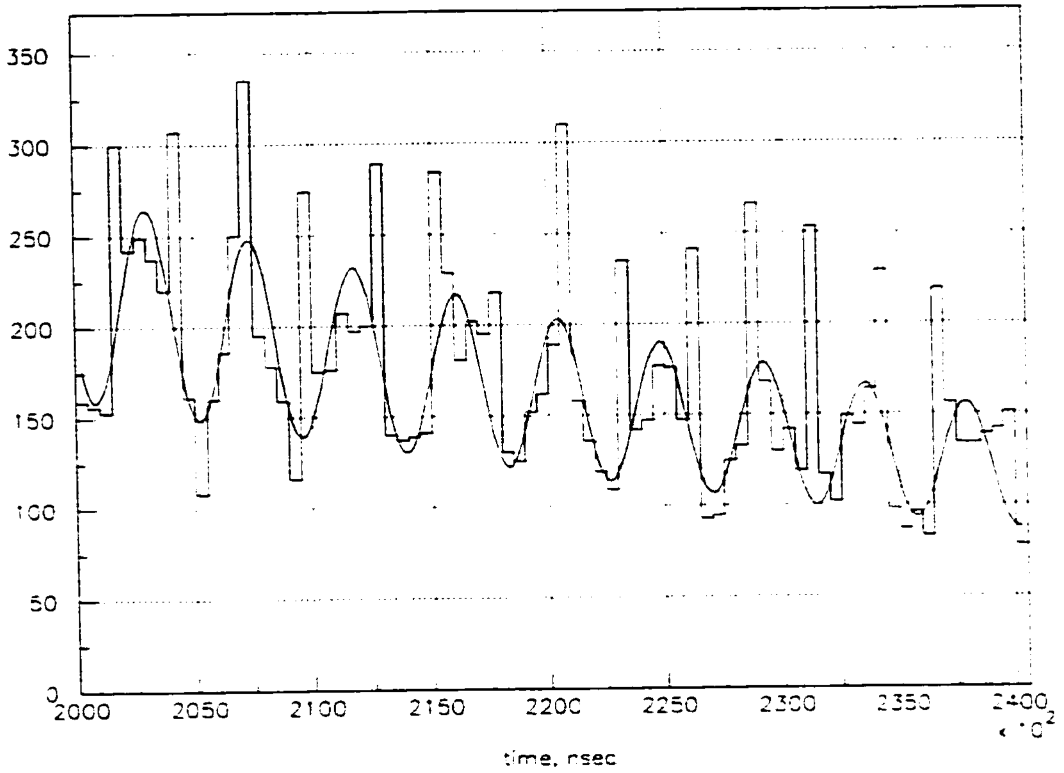

Figure 4.3: Time spectrum of the decay positrons from one data-taking run. The extraneous decay positrons due to the flashlets, which have a period of 2.7 μs, are seen in addition to the $g-2$ oscillation of period of 4.3 μs. This run has extremely high flashlet conttamination and doesn't represent a normal run.

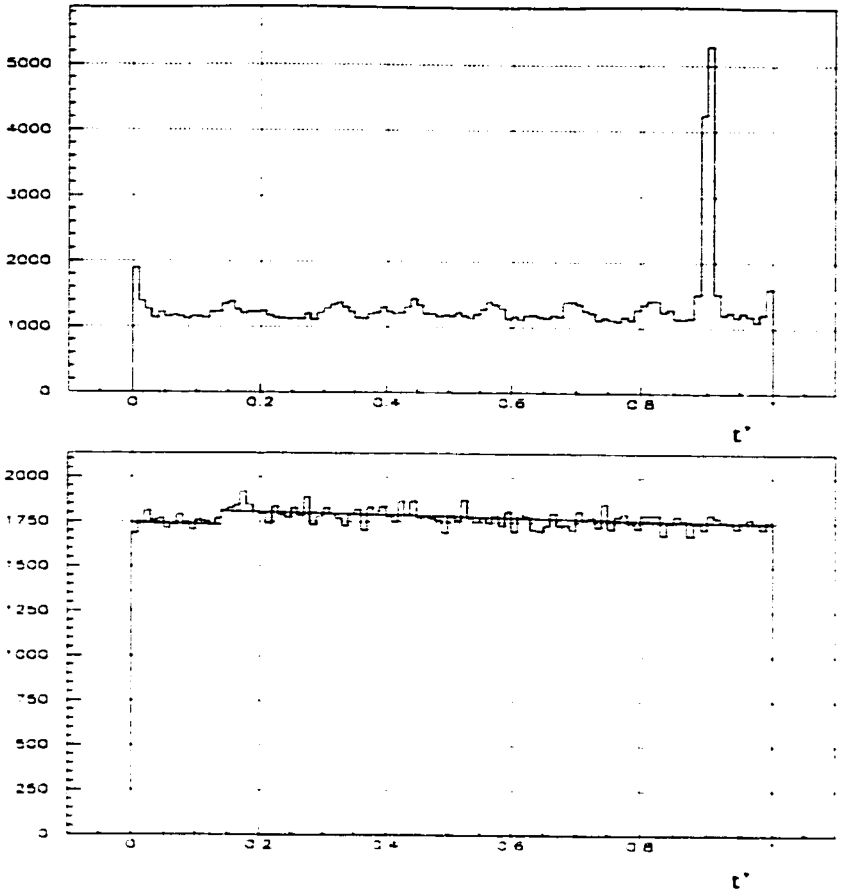

Figure 4.4: t' distribution. The top plot shows the result from a data-taking run with large flashlet contamination and the bottom plots shows the result from a run without flashlet contamination above the statistical fluctuation.

to determine the muon spin precession frequency ω_a, flashlets introduce an error into our measurement. Hence, it is important to monitor the presence of these flashlets. A sensitive way to monitor the them is to fold all the data into one AGS cyclotron period of 2.7 μs[60]. The transformation

$$t' = \frac{t}{T_{AGS}} - \text{integer}\left(\frac{t}{T_{AGS}}\right) \tag{4.10}$$

was applied to the data, where t is the time of the decay positron with respect to the time of injection and T_{AGS} is the AGS cycletron period which is 2.7 μs in our case. Fig. 4.4 shows the t' distributions from one data-taking run with flashlets and one data-taking run without flashlets. The $g-2$ oscillation is averaged out and the slope is due to the muon decay with a dilated time life of 64.4 μs.

As soon as flashlets were observed, AGS tuned the extraction timing to remove most of the flashlets. However, after the AGS started to store 12 bunches of protons on Feburary 24 1999, the period between two ajacent bunches was smaller and the flashlets level increased significantly. None of the data taken after Feburary 24 was not used for the $g-2$ measurement. The studies of the 12 bunches mode in the AGS helped to collect more muons in the 2000 and 2001 runs. More studies on flashlets were done in the analysis and will be discussed in Sec. 6.3.

4.4 $g-2$ oscillation

After the beam is injected into the storage ring, many particles collide with the vacuum chamber, inflector, electrostatic quadupoles, etc., and produce an intense background, called flash, in the detectors at early times. To protect PMTs from the flash, all PMTs were turned off during the beam injection and for 5 to 25 μs afterwards. The amount of the flash varied around the ring, and it was necessary to set individually the time for each PMT to be turned on. The time varied from 5 μs to 25 μs after the injection in the 1999 run. We took data until 700 μs after the injection. This is more than 10 times larger than the dilated muon life time of 64.4 μs in our experiment. The data-taking was stopped and restarted when any data-taking condition changed or about every half hour to keep the size of the data stored in one file under 1 GBytes to avoid the inconveniences in the offline analysis. A continuous data-taking period is called a data-taking run. Fig. 4.5 shows the time and energy spectra of the decay positrons in a typical data-taking run. Thesse spectra were checked for each calorimeter immediately after the data-taking run was ended. In total 1280 data-taking runs were recorded onto tapes in 1999 run and about 2.9×10^9 positrons are collected.

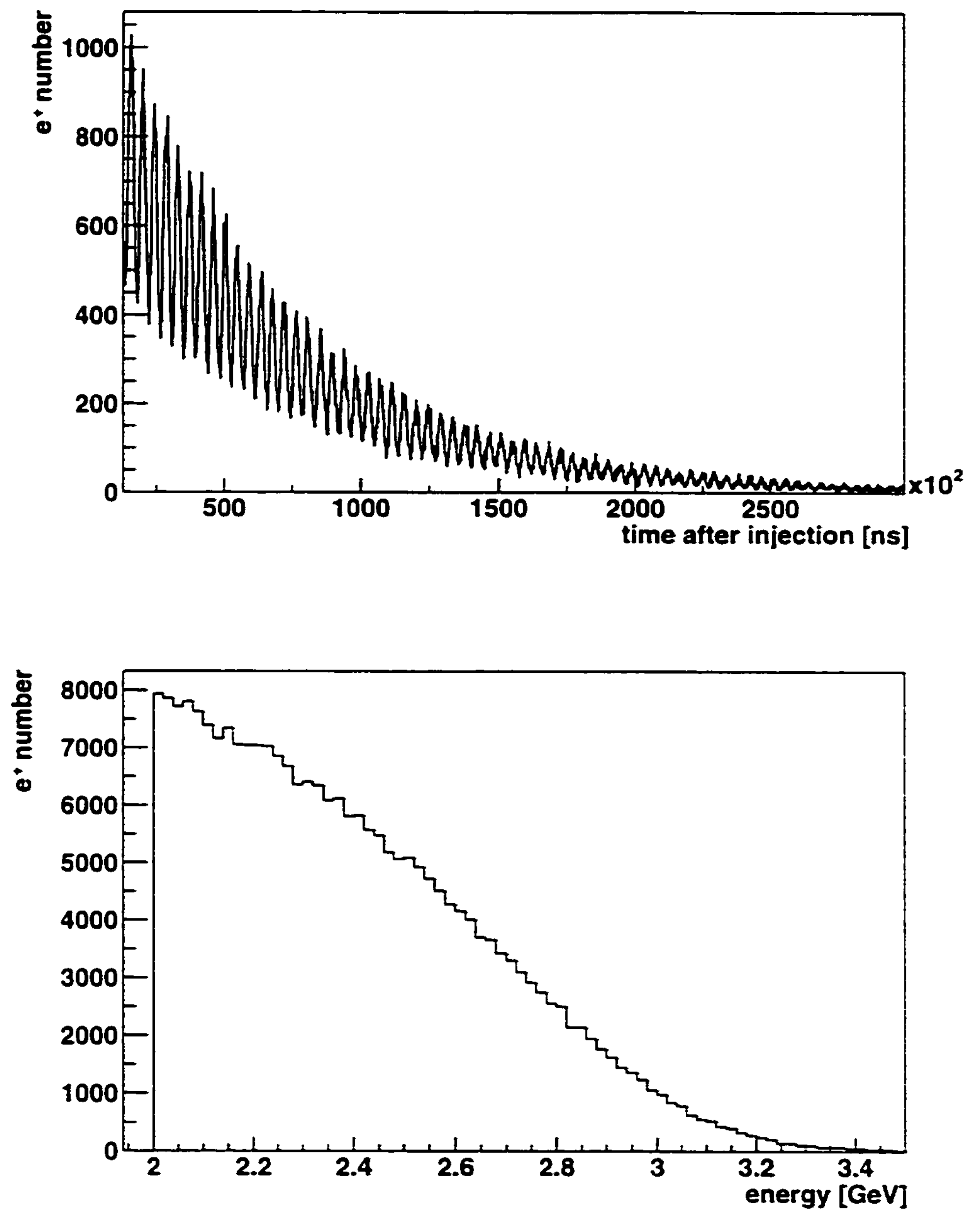

Figure 4.5: The top plot shows the time spectrum of the decay positrons in a data-taking run and the bottom plot shows the correspondant energy spectrum. A cut on energy, E >2GeV, is used.

Chapter 5

ω_p analysis

5.1 Introduction

The measurements of the magnetic field at sub-ppm lever is done with NMR probes and is expressed relative to the free proton NMR frequency ω_p.

The NMR frequencies are measured with respect to a standard probe, which is a spherical water sample. The calibration of the standard probe with respect to the free proton is obtained from other experiments[54].

A trolley with 17 NMR probes, calibrated with respect to the standard probe, was used to measure the field around the storage ring seventeen times from January to early March 1999.

The field between trolley runs was measured by a fixed probe system. The average measurements from more than 120 fixed probes during the trolley run is calibrated with respect to the trolley measurements.

The muon distribution is taken into account by using the field value at the center of the muon distribution. The muon distribution is measured by fast rotation and FSD studies.

5.2 NMR probe measurement

As mentioned in Sec. 3.5, the magnetic field is determined by measuring the frequency of the FID signals from the NMR probes relative to 61.74 MHz. The method of measuring the frequency is shown in the cartoon plot Fig.5.1. Due to the residual of the excitation pulse, the FID signal is superimposed on a decaying baseline. To avoid the influence from the excitation pulse, we did not start the frequency measurement before time t_1. Since the oscillating FID signal also decays, t_1 was set to be 20 μs. After the time t_1, the FID signal is compared to a DC threshold. When the signal voltage is increasing and crosses the threshold, we get a so-called up zero crossing. A down zero crossing happens when the voltage of the signal is decreasing. The time of the first up zero crossing after t_1 is labeled as t_{10}. The time of the first up zero crossing after the time t_2 is label as t_{20}, where the time t_2 is either when

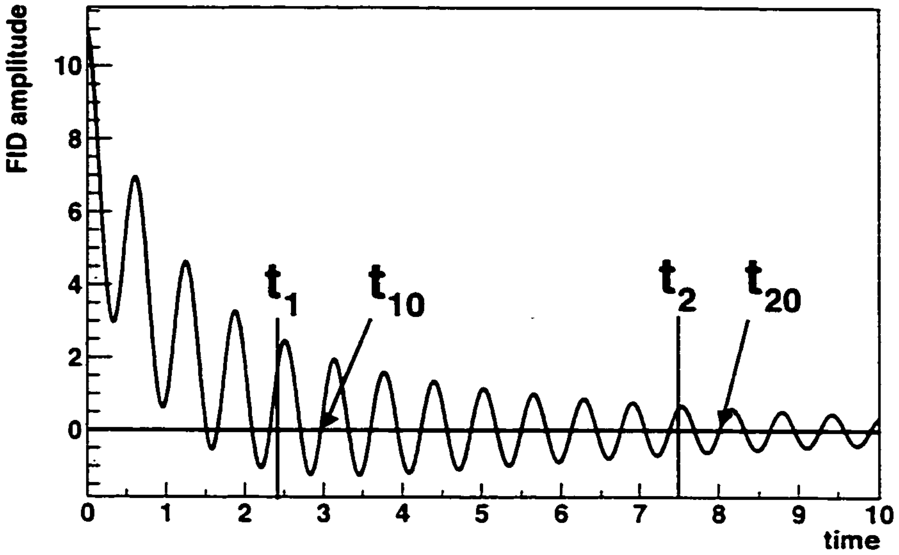

Figure 5.1: The measurement of the frequency of the FID signal.

the amplitude of FID signal decays lower than a threshold or a preset time, whichever occurs first. The FID signal is sent to both a trigger electronics system and a zero crossing counter. The trigger system starts and stops the zero crossing counter at t_{10} and t_{20}, respectively. FID signals sent to the zero crossing counter are delayed by 20 ns compare to those sent to the triggle system. Hence the counting of zero crossings starts and stops at $t_{10} - 20$ ns and $t_{20} - 20$ ns, respectively. The frequency of the FID signal $f_{\rm FID}$ is determined as

$$f_{\rm FID} = N_0/(t_{20} - t_{10}), \tag{5.1}$$

where N_0 is the number of either the up or the down zero crossings between t_{10} and t_{20}. For the trolley probe measurements, the down zero crossing are counted. For the fixed probe measurements, the up zero crossing are counted. In this case, the up zero crossings at t_{20} is not counted due to the 20 ns delay mentioned above. However, the zero crossing at t_{20} was occasionally counted due to the electronic malfunctions and noise. Hence the number of zero crossings between t_{10} and t_{20} is miscounted by one. The miscount affects the frequency measurement by

$$\Delta f_{\rm FID} = f_{\rm FID}/N_0, \tag{5.2}$$

where N_0 is the real number of the zero crossings. $\Delta f_{\rm FID}$ varies, depending on N and $f_{\rm FID}$. A program is used to search for and correct the miscount. When the program calculates the frequency of the FID signals, it compares the value to the average of the previous 10 readings. If the difference is larger than 5

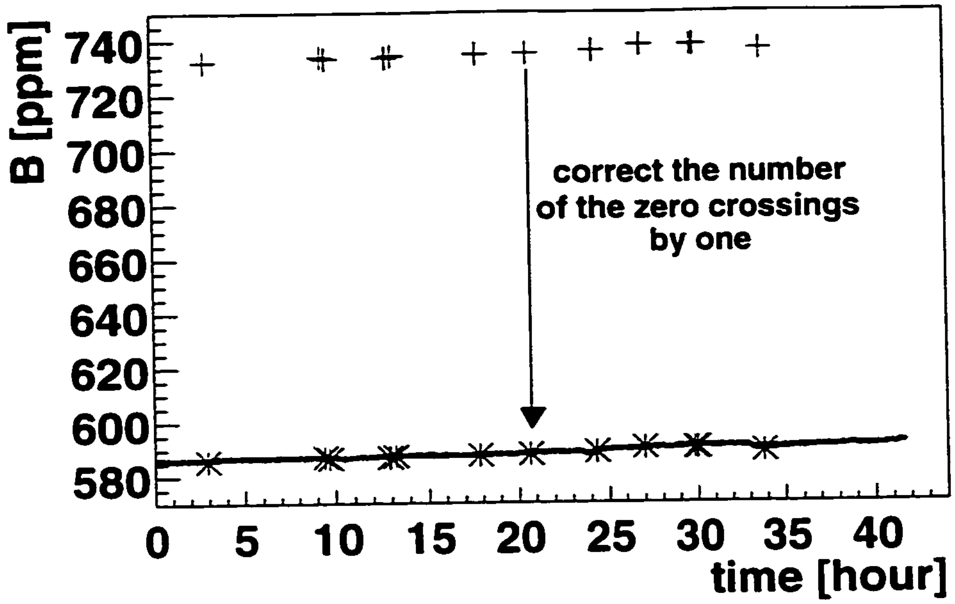

Figure 5.2: Corrections of the miscount of the zero crossings. The black curve shows the measurements of the magnetic field with the correct number of zero crossings. The crosses show the measurements with the number of zero crossings miscounted by one as explained in the text. The stars show that the corrected values agree with the normal measurements.

times the root mean square of the previous 10 readings, the program corrects the zero crossing count by one and recalculates the frequency. If the new value agrees with the average of the previous 10 readings, it is confirmed that this is a reading with miscount and the FID frequency is calculated with the correct number of zero crossings. Otherwise, the value is used as the frequency measurement but not used to calculate the average or rms for the next reading. If more than two consecutive readings differ from the average of the previous readings by more than 5 times the rms of the previous readings, we assume there is a real field change and the average of the previous reading is not used any more, and the next 10 readings will be used to calculate a new average. Fig. 5.2 shows some examples of such corrections. About 0.7% of the fixed probe readings need the zero crossing correction.

5.3 Temperature influence on magnetic field

To achieve the required stability of the magnetic field, the magnetic field dependence on the yoke and the environment temperature were studied carefully by using data taken in 1997.

Temperature was measured every 15 minutes. On each of the yokes C, D,

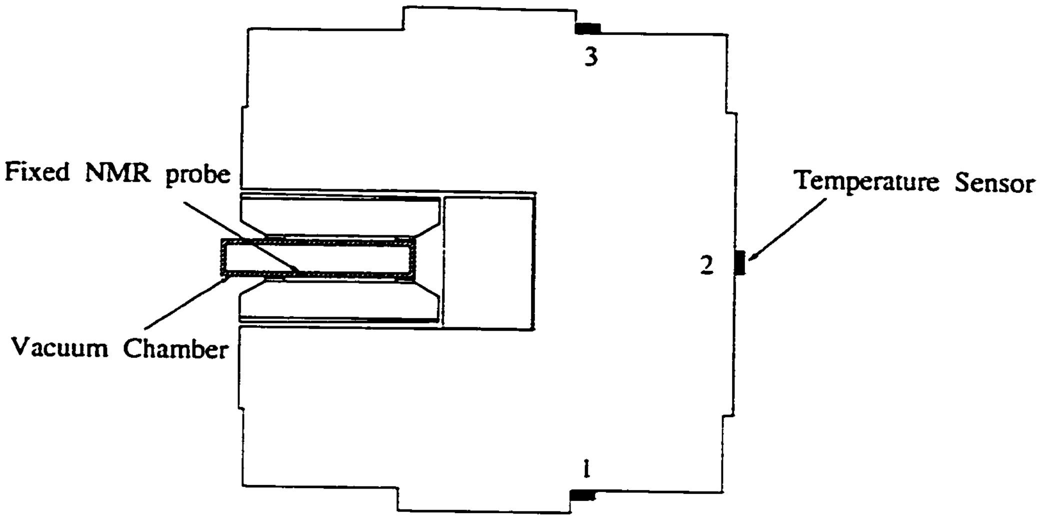

Figure 5.3: The locations of the temperature sensors on the iron yoke.

E, F, G, there are three temperature sensors. Sensor number 1 is located on the bottom of the yoke, sensor number 2 is mounted on the back of the yoke and sensor number 3 is on the top of the yoke as shown in Fig. 5.3. Yokes A, B, H, I, J, K, L each has only one sensor mounted on the back of the yoke, sensor number 2. In addition there are two temperature sensors, O1 and O2, which measure the temperature of the magnet cryostat box. This temperature is regarded as the environmental temperature. The accuracy of the temperature measurement is about 0.12°C.

The temperature measurements from May 8 1998 to July 7 1998 are shown in Fig. 5.4. The cryostat box temperature displays the expected day-night oscillation. The day-night oscillations of the temperature of yokes are much smaller due to the large heat capacity of the iron yokes. For the same reason, the long-term temperature change of the yokes is about 3 days behind such change in the environment. The largest observed rate of the yoke temperature change is about $0.1°C$ per hour. The temperature of yoke E and F, which are close to a roll-up entrance door to the experimental hall, shows the largest fluctuations.

The dipole moment of the magnetic field at the azimuthal position of the temperature sensors was determined by the average of the readings of all fixed probes at that azimuthal location. The normal quadrupole is determined by the difference of the readings from the fixed probes at different radial positions, and the skew quadrupole is determined by the difference of the readings from the fixed probes at the top and bottom poles. Since the change of magnetic field is the concern, the absolute value of the field need not be calibrated. Figure 5.5 shows the dipole and multipoles of the magnetic field as a function of time. Because the temperature sensors are located on the surface of the

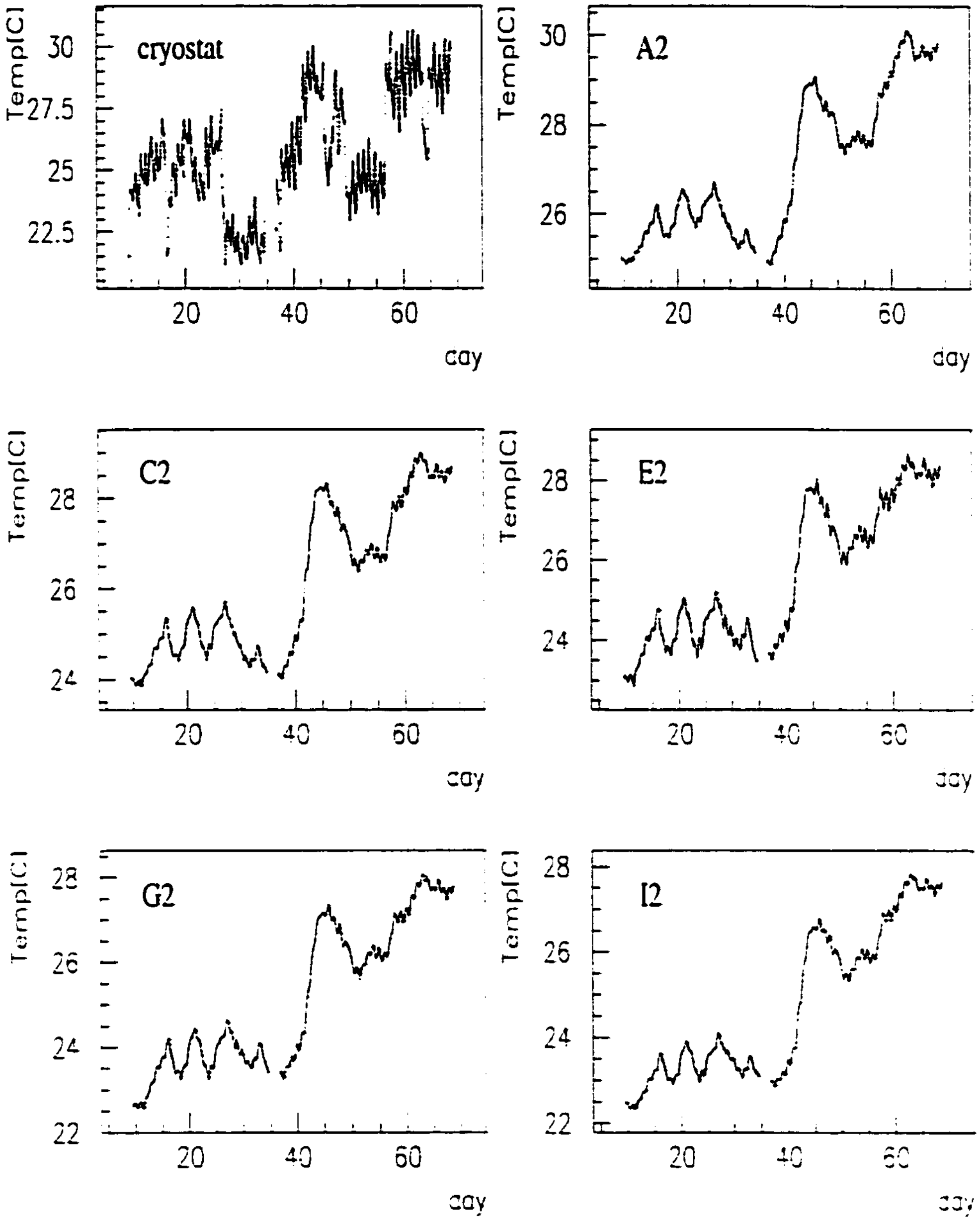

Figure 5.4: Temperature readings from some sensors. The data covers the period from 5/8/1998 to 7/7/1998.

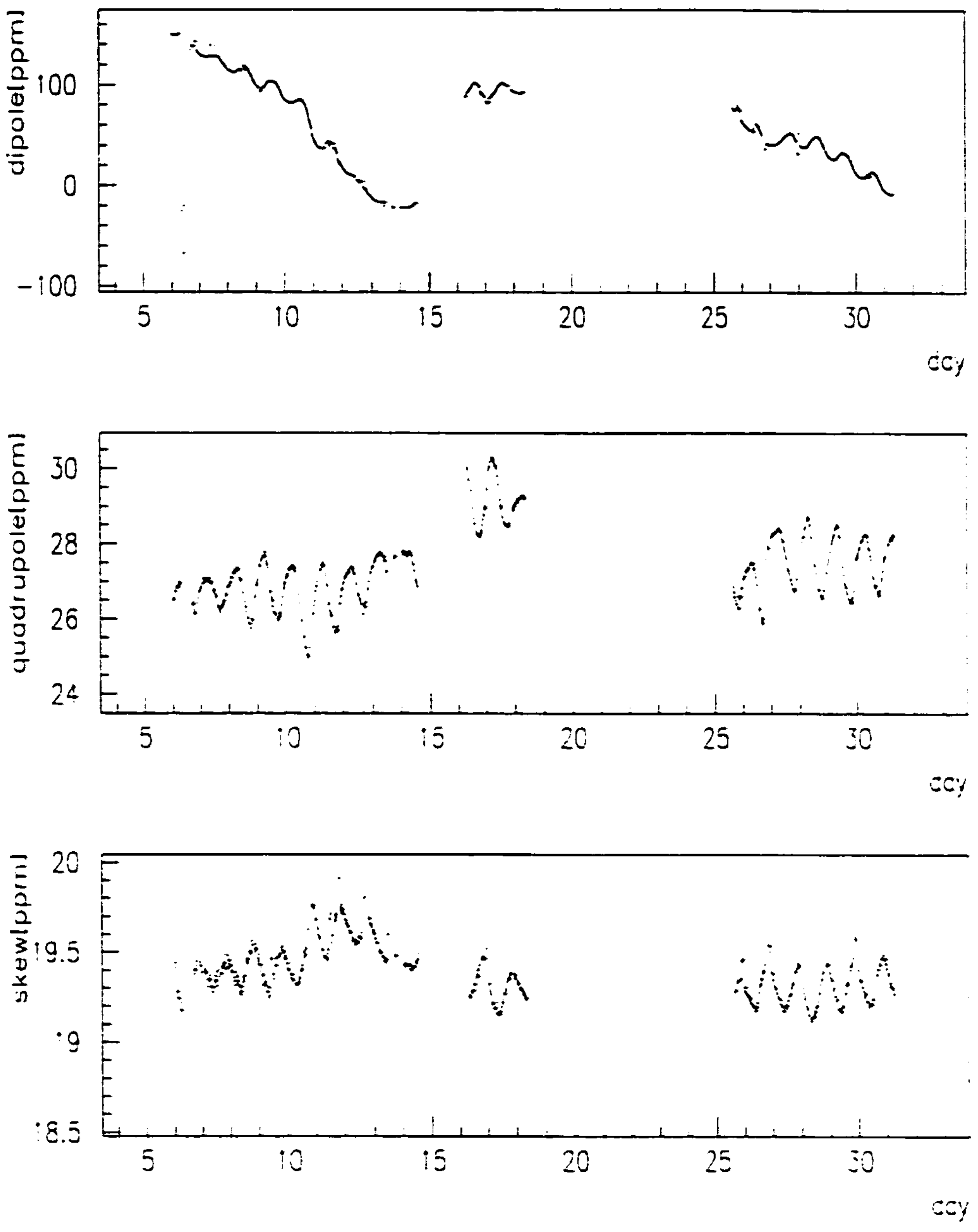

Figure 5.5: The lowest multipole of the magnetic field during the 1998 run.

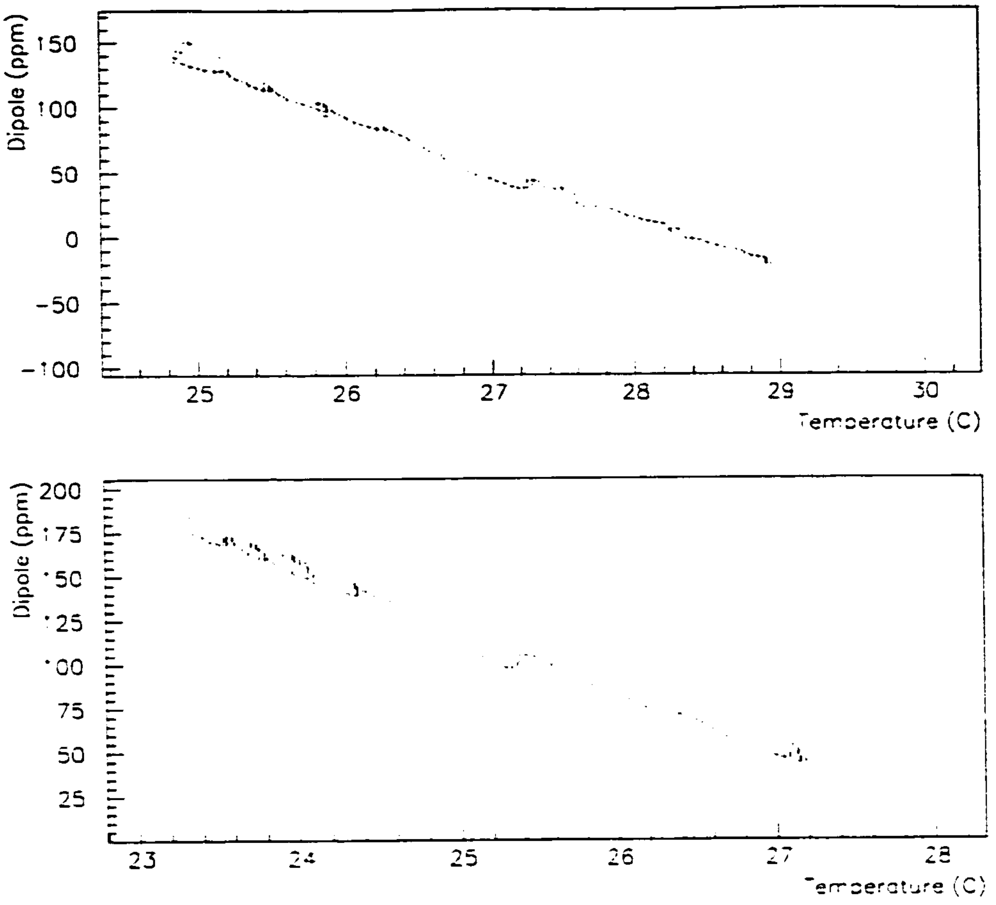

Figure 5.6: The dependence of the dipole moment of the magnetic field on the yoke temperature. The top plot corresponds to an azimuthal postion of 5° downstream from the injection point and the bottom plot is at 185°.

iron yoke, the temperature change of the yoke itself lagged that measured by the sensors. Hence, the change in the magnetic field lagged the temperature change measured by the sensors. We determined this time delay from data by comparing the times of the sharp change of the temperature and that of the dipole moment. This time delay was found to be about 2.2×10^3 seconds. For the following figures of the magnetic field dependence on the temperature, the temperature data are shifted by -2.2×10^3 seconds with respect to the magnetic field data. Fig. 5.6 shows the dipole of the field versus the temperature at two different azimuthal positions, 5° and 185° from the injection point. The dipole moment changes by about 35 ppm/°C. The negative slope is caused by the thermal expansion of the yoke which increases the gaps between top and bottom poles and hence decreases the magnetic field. However, the quadrupole moments do not have a direct dependence on the temperature as shown in Fig. 5.7. This is because the changes of the quadrupole moments

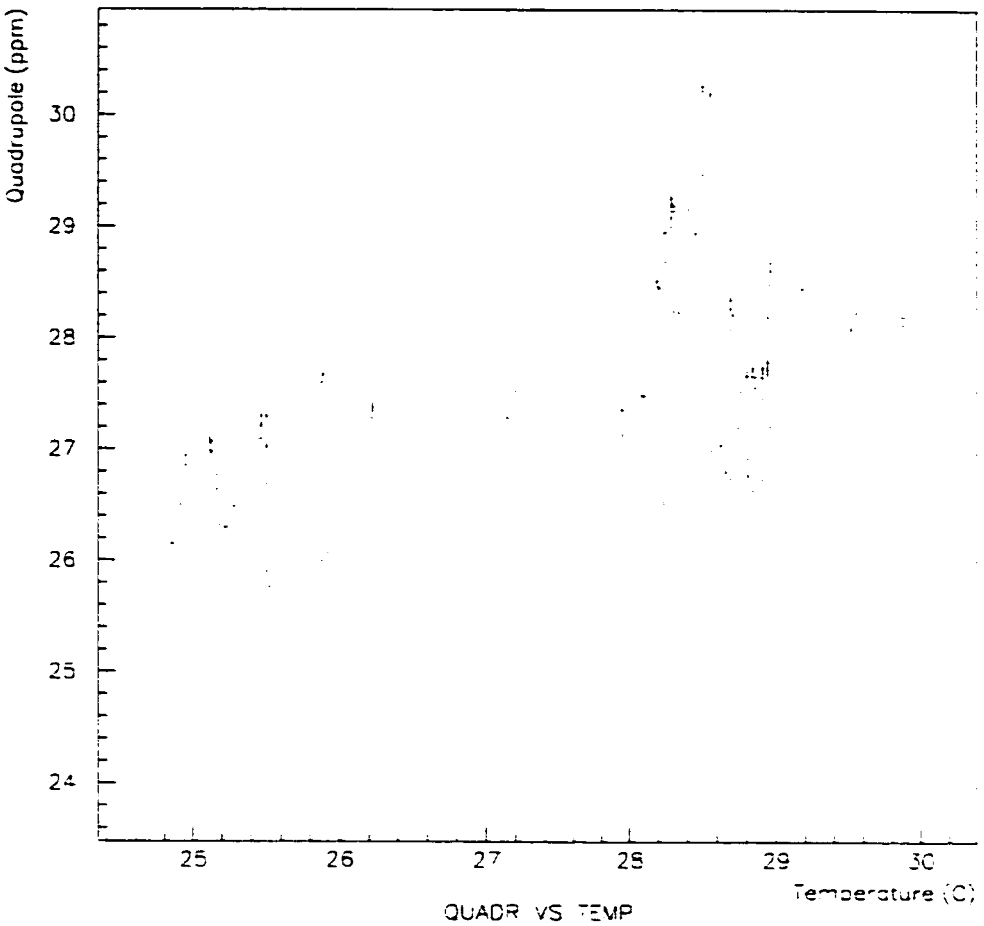

Figure 5.7: Relation between normal quadrupole moments. normalized at 4.5 cm, and the temperature.

are caused by tilts of the magnetic poles rather than the distance of between top and bottom poles. The tilts of the magnetic poles, however, are related to the temperature gradients across the yoke. Hence the quadrupole moments are related to the rate of the temperature change as shown in Fig. 5.8. The normal quadrupole moment changes by about 25 ppm/°C/hour and the skew quadrupole changes by about 6 ppm/°C/hour. Both quadrupole moments are normalized at 4.5 cm as mentioned in Section 3.5. The magnetic field changes due to the temperature effect are large and hence thermal insulation was put on to cover the yoke after the 1997 run and before the 1998 run. Additional insulator was used to cover the magnet pole after the 1998 run and before the 1999 run. The day-night fluctuation of the temperature of the yoke is less than 0.1 C° as shown in Fig. 5.9. To reduce the magnetic field fluctuation, a feedback system was implemented between the 1998 run and the 1999 run. This system maintained the average readings of 36 uniformly distributed fixed probes to 0.1 ppm by feedback to the main magnet power supply.

5.4 Calibration

5.4.1 Calibration of the standard probe

The quantity ω_p is the proton resonance frequency for a free proton in the magnetic field B being measured. A standard NMR probe (Fig. 3.15) is required for which the ratio of ω_p(std) to ω_p (free proton) is known. The standard probe we used is a spherical sample of pure water and we take

$$\omega_p(\text{spherical water}) = \omega_p(\text{free proton}) \times (1 - \sigma_{H_2O}) \tag{5.3}$$

where the diamagnetic shielding factor $\sigma_{H_2O} = 25.790(14)$ ppm at $34.7^\circ C$[55], $d\sigma_{H_2O}/dT = 10.36(30)$ ppb/$^\circ C$[56].We did the calibration at $24 \pm 2^\circ C$ and hence $\sigma_{H_2O} = 25.68(2)$ ppm[4].

The standard probe of spherical water was designed and consturcted with great care in the choice of material and with strict mechanical tolerances. It was studied and tested by mechanical and optical measurements. The conclusion was that it had an uncertainty of 0.034 ppm[54].

Since the same standard probe was used the the muonium experiment[45], a check of the accuracy of the standard probe is provided from the comparison of the value of μ_μ/μ_p obtained from (1) the experimental and theoretical values of the hyperfine structure interval $\Delta\nu$ in muonium[4, 45, 61] and from (2) the Zeeman effect in muonium[45].

The value of

$$\lambda = \frac{\mu_\mu}{\mu_p} = 3.183\,345\,39(10)[4] \tag{5.4}$$

used in the determination of a_μ (see Eq. 3.6) is obtained by the first method. It involves equating $\Delta\nu$(theory) and $\Delta\nu$(expt.) which determines m_μ/m_e, the

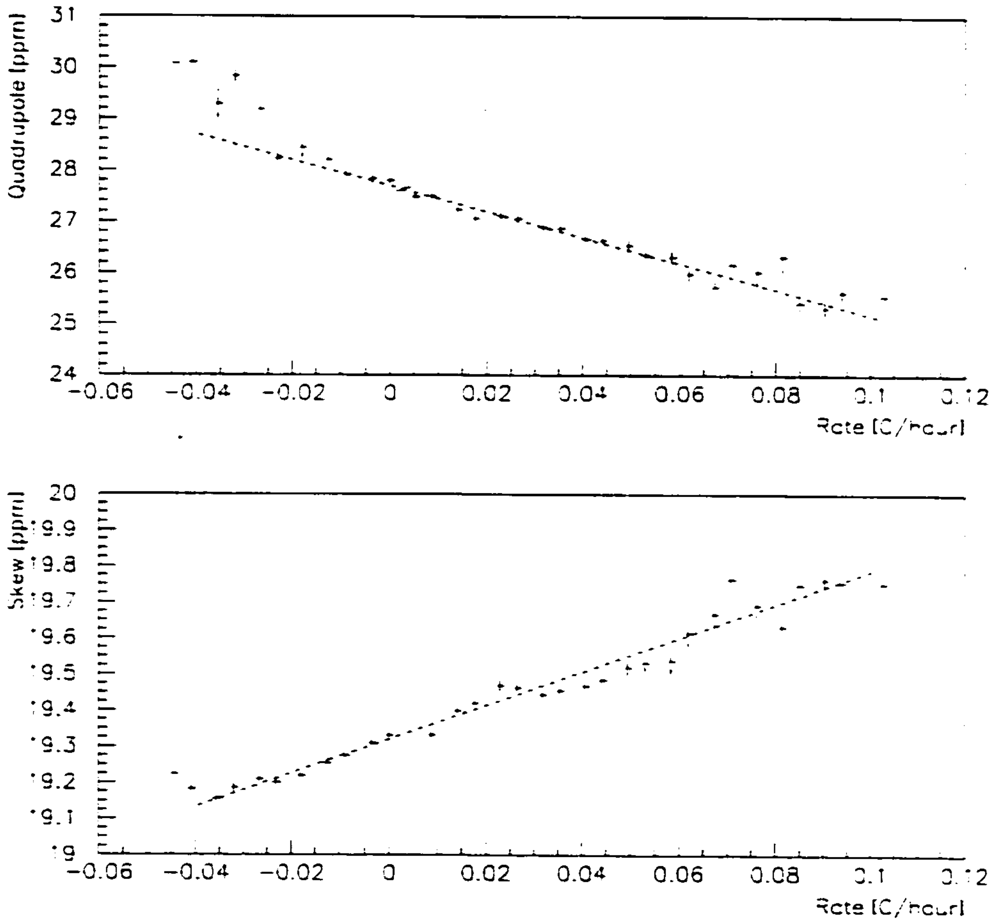

Figure 5.8: The dependence of the normal(top) and skew(bottom) quadrupole moments, normalized at 4.5 cm, on the rate of temperature change. The dash lines are linear fit to the data between -0.02 and 0.1 °C/hour

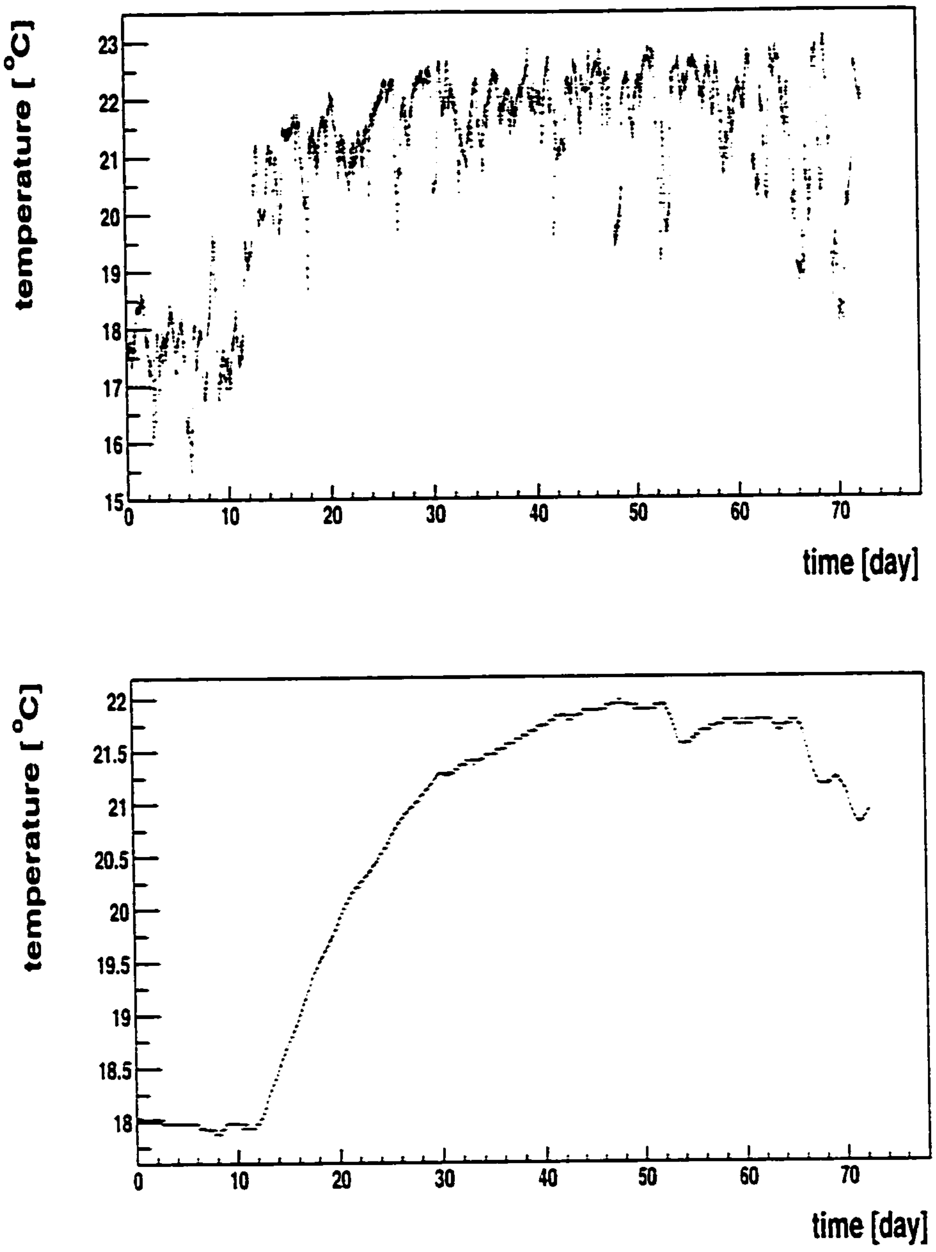

Figure 5.9: The top plot shows the cryostat temperature during 1999 run and the bottom plot shows the temperature measured at the back of one yoke. The short term fluctuation of the yoke temperature is small due to the thermal insulation.

least well known constant in $\Delta\nu$(theory). Hence, use of the equation

$$\frac{m_\mu}{m_e} = \frac{\mu_e}{\mu_p}\frac{\mu_p}{\mu_\mu}\frac{g_\mu}{g_e} \tag{5.5}$$

allows the determination of

$$\lambda = \frac{\mu_\mu}{\mu_p} = 3.183\ 345\ 39(10)\ (30\ ppb[4,\ 45]. \tag{5.6}$$

This determination of λ does not involve the standard probe.

An alternative determination of λ can be made from the measured Zeeman transition frequencies in muonium, in which the magnetic field is measured with the standard probe. This value of λ is

$$\lambda = \frac{\mu_\mu}{\mu_p} = 3.183\ 345\ 24(37)\ (120\ ppb). \tag{5.7}$$

The equality of these two determinations checks the accuracy of the standard probe to about 0.1 ppm.

The error of the calibration of the standard probe is estimated to be 0.05 ppm.

5.4.2 Calibration of the trolley probes

The calibrations of the trolley probes were done by comparing the NMR readings of the trolley probes to the readings of the standard probe at the same position in the magnet. The feedback control of the field was turned off during the calibrations. Because the dimensions of the standard probe make it impossible to reach the positions of all 17 trolley probes (Fig. 3.11), we did the calibration of the trolley probes with respect to the standard probe through a calibration probe called the plunging probe (Fig.3.14), which was mounted on a stand and can be moved in radial and vertical directions to reach the positions of all trolley probes. The standard probe can reach the positions of trolley probes 1, 5, and 15(see Fig. 3.11) and direct calibrations of these probes were also done.

The 17 trolley probes are calibrated with respect to the plunging probe by comparing the NMR readings of the plunging probe and the trolley probes at the azimuthal position of the plunging probe stand. The errors come from the position uncertainties of the trolley probes and of the plunging probe, and from the B field inhomogeneity,

$$\sigma_{\text{calib}} = \sqrt{\left(\sigma_x \times \frac{dB}{dx}\right)^2 + \left(\sigma_y \times \frac{dB}{dy}\right)^2 + \left(\sigma_z \times \frac{dB}{dz}\right)^2}. \tag{5.8}$$

where σ_{calib} is the error of the calibration and x, y, z are the radial, vertical and azimuthal positions.

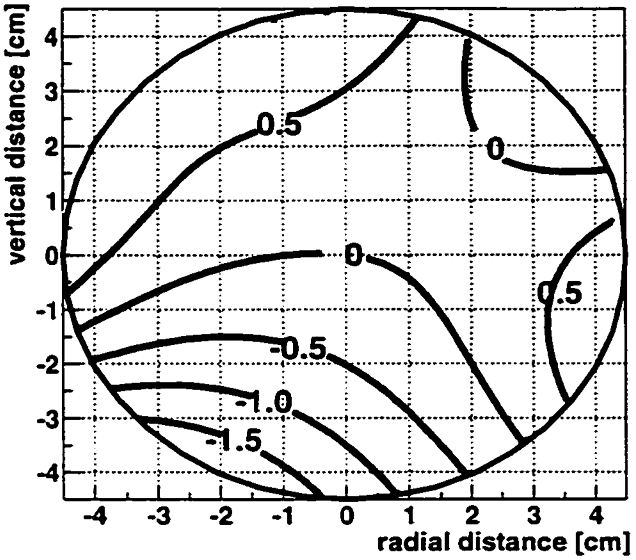

Multipoles [ppm]

	normal	skew
Quad	0.11	0.85
Sext	0.52	-0.77
Octu	-0.11	-0.31
Decu	0.32	-0.02

Figure 5.10: The half ppm contour plot of the B field and the multipoles at the azimuthal position of the plunging probe stand. The surface correction coils were used to improve the homogeneity of the field.

In 1999 we adjusted the surface correction coil currents to minimize the local B field gradients in the vertical and radial directions at the position of the plunging probe stand. The contour plots and the multipoles of the B field at this location, as determined from the plunging probe measurements, are shown in Figure 5.10. The largest multipole is the skew quadrupole, which is 0.85 ppm at 4.5 cm. To estimate the position uncertainties associated with the radial and vertical directions, a relatively large sextupole field of about 7 ppm at 4.5 cm was applied with the surface correction coils. The change of the field is measured by both the trolley probes and the plunging probe as shown in Fig.5.11. The results from both measurements were compared to determine the vertical and radical displacements between the positions of the trolley probes and the positions of the plunging probe. The radial and vertical position uncertainties are about 1 mm, which gives an error of 0.02 ppm in the calibration of the trolley probes.

There are two sources of position uncertainty for the trolley probes in the azimuthal direction. One is the uncertainty of the trolley shell position with respect to the plunging probe position. This uncertainty is about 1 mm for the average of the several calibrations repeated by different people. The other is the position uncertainty of the active volume of the NMR probes inside the trolley with respect to the trolley shell. This uncertainty can not be reduced by repeated measurements because the probes are fixed inside the trolley. The NMR probes are about 10 cm in length and 7 mm in diameter, with coils

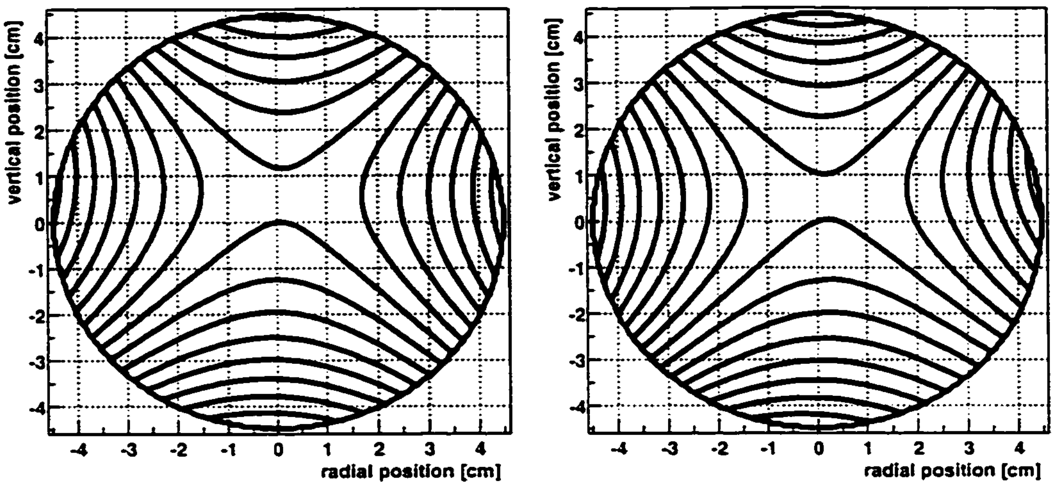

Figure 5.11: One ppm contour plot of the sextupole field introduced by the surface coil currents. The left plot is from the plunging probe measurements and the right plot is from the trolley measurements. The small difference of the position of the sextupole pattern gives the position displacement of the trolley probes with respect to the plunging probe positions in radial and vertical directions.

of 2 cm in length. We estimate this position uncertainty to be 2 mm along the length axis of the trolley. The field gradients in the azimuthal direction were evaluated by moving the trolley to the left and right of the calibration position. Figure 5.12 shows the result of one of the measurements, in which the trolley was moved away from the calibration position by 4 mm to one side and 5 mm to the other. For most trolley probes, the change of calibration was less than 1 ppm when the trolley was moved over 9 mm. We know the azimuthal position of the NMR probes inside the trolley to about 2 mm inaccuracy, which gives an error of 0.2 ppm for each probe. The dipole field is determined from a combination of the trolley probe readings.

After the 1999 run, the trolley probes were calibrated with respect to the plunging probe seven times in total, by different people. The calibrations agree with one another except for probe 8, which is a known bad probe and is discarded in the analysis.

On March 9, 1999, the trolley center probe and the plunging probe were calibrated with respect to the standard probe at the center of the storage region, about 1 m away from the plunging probe stand. The field gradient in this position is 0.64 ppm/cm as measured during the trolley run on March 8 1999, whereas the field gradient at the plunging probe stand was -0.53 ppm/cm as shown in Figure 5.12. A 2 mm uncertainty in the trolley probe positions thus results in an error of 0.13 ppm for this calibration. In addition to the direct

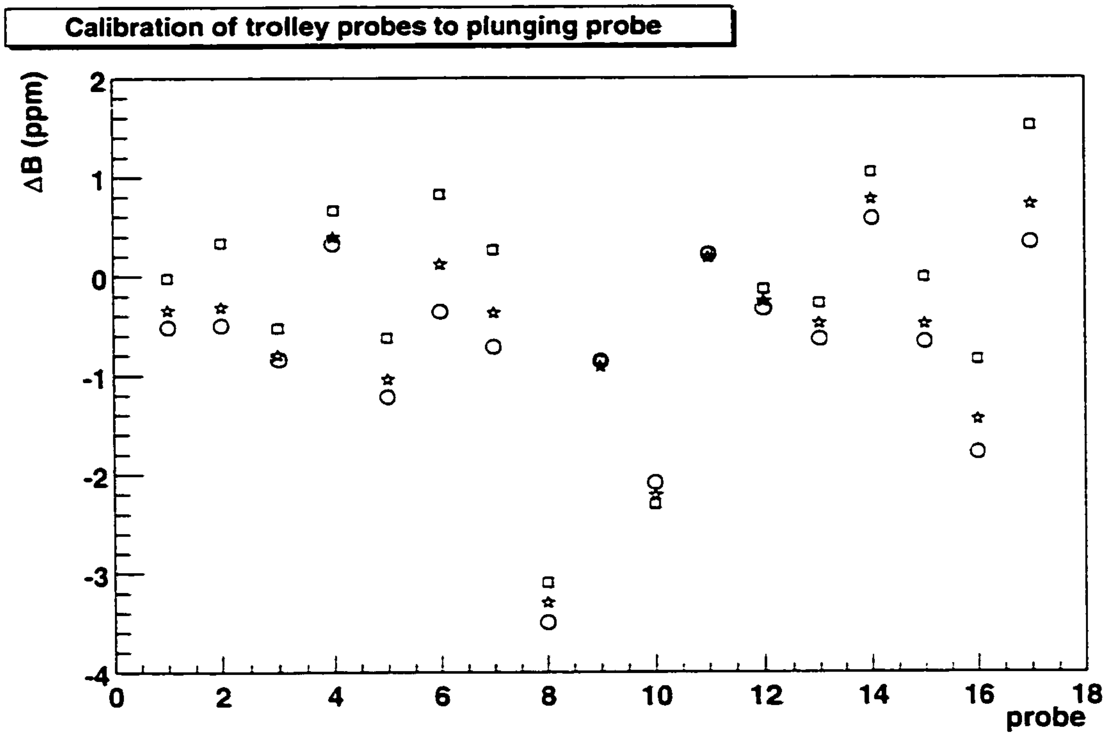

Figure 5.12: The differences between the field measurements with the trolley probes and with the plunging probe. The stars are the data taken when the trolley was at the azimuthal position of the plunging probe stand. The circles are the data taken with the trolley displaced 4 mm to one side of the calibration position, and the boxes are with the trolley displaced 5 mm to the other side.

calibration of the trolley center probe with respect to the standard probe, an indirect calibration was made, which involved the calibration of the trolley center probe with respect to the plunging probe at the plunging probe stand and the calibration of the plunging probe with respect to the standard probe. It is found that these two calibrations of the trolley center probe differ by 0.2 ppm. Position offsets of the trolley probes can contribute to this difference and we designate 0.2 ppm as systematic error in the calibration.

The calibration is also compared to the calibration done in 1998 run. A 0.3 ppm difference is found for probe 3. we have therefore discarded probe 3 in the analysis.

A further cause of systematic error is the frequency counter inside the trolley. When we start the measurement of the NMR frequency, the NMR signal is superimposed on a decaying baseline as mentioned in Section 5.2. The frequency measured by counting zero crossings varies with the voltage supplied to the trolley and with the frequency itself. Both dependencies have been studied by changing the voltage and the reference frequency. The effect on the frequency measurements due to the temperature of the electronics was also studied by runing the trolley in vacuum for a long period. In the range of our operating values. their effects on the field measurements are smaller than 0.1 ppm. which is included in the "Others" systematic error in Table 5.1.

5.5 Measurement of azimuthal field average with trolley probes

From January to early March 1999. 17 successful trolley runs were made. In each trolley run. the trolley covered the whole 360° in azimuth during a period of about 2 hours. As the trolley moves around the ring, NMR readings are continually taken in succession with all the probes. The readings for all 17 trolley probes requires about 1 second during which the trolley moves 1 cm. Each NMR frequency reading has a statistical precision of about 0.05 ppm.

The position of the trolley is determined from the potentialmeters' resistance. as mentioned in Section 3.5. Due to the nonlinearity of the potentiometers, the elasticity in the cable. nonuniform friction along the trolley rails and rail gaps, this measured position of the trolley can differ from the true position by up to 20 cm. This difference changes slowly around the azimuth. To reduce this difference, an improved determination of the trolley position is made based on the perturbation of the fixed NMR probe readings due to the passage of the trolley during the trolley runs. This perturbation is shown in Fig. 5.13. Since the exact positions of the fixed probes are known. we calibrate the trolley position measurements from the potentiometers with respect to the position of 36 selected fixed probes. The 36 fixed probes are 10° apart in azimuth. Fig. 5.14 shows the corrections to the trolley azimuthal position measured by the potentiometers. A linear interpolation between the 36 calibrated positions is

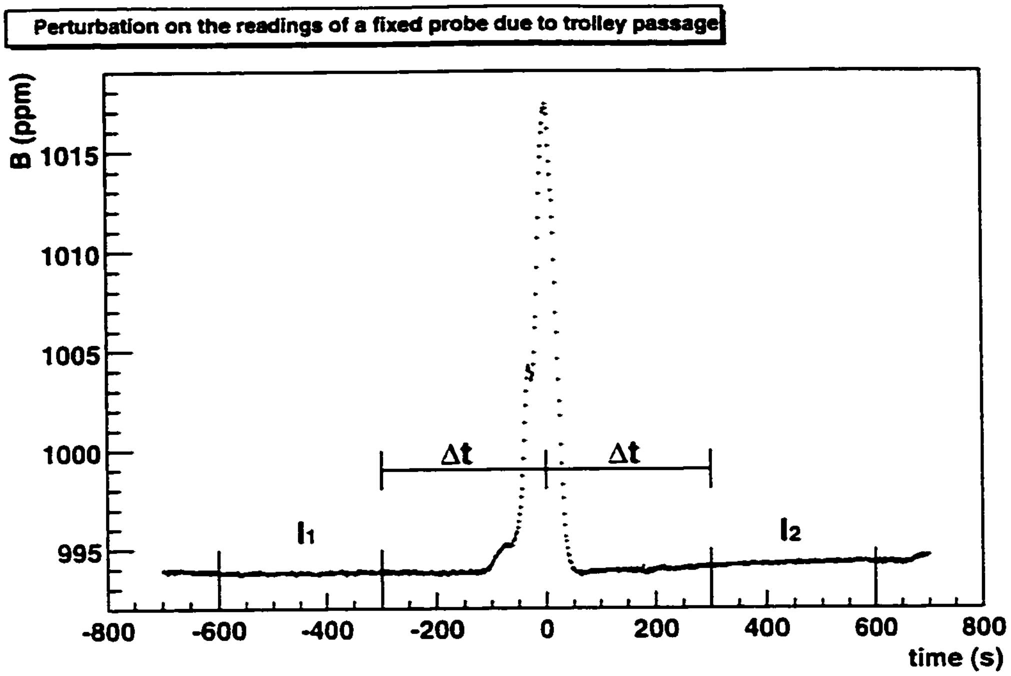

Figure 5.13: The perturbation of the NMR readings of a fixed probe due to the passage of the trolley. The readings in the time intervals I_1 and I_2, lasting 300 s each, are used to obtain the average field.

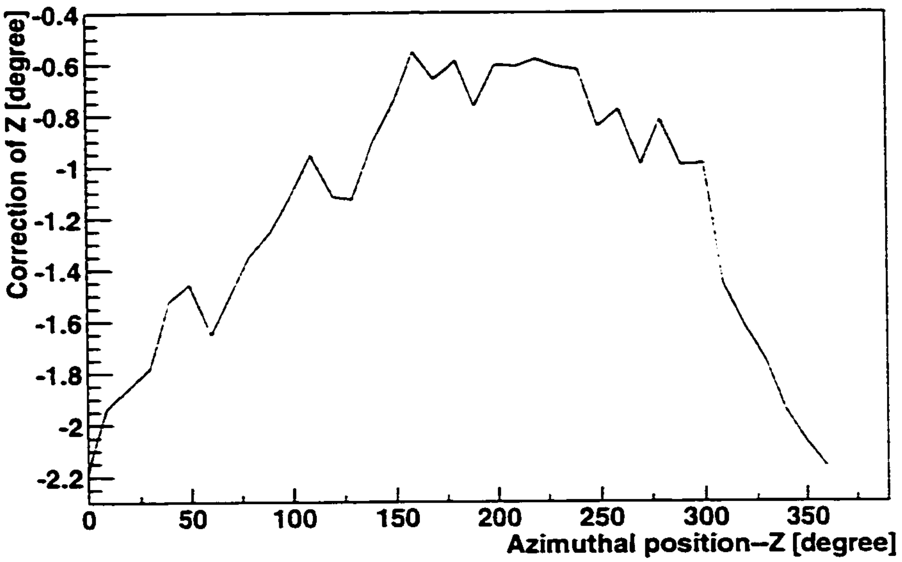

Figure 5.14: Corrections to the trolley azimuthal position measured by the potentiometers using the perturbation of the fixed NMR probe readings due to the passage of the trolley.

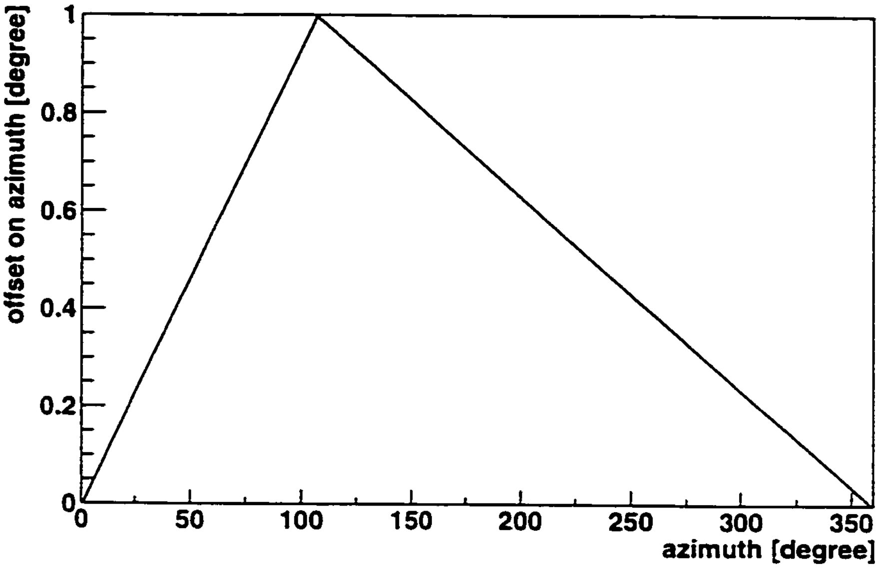

Figure 5.15: Non-linearity in azimuthal position readout versus azimuth.

used to correct the trolley positions. With this position correction the calculated average field differs by about 0.15 ppm from the average field calculated with the trolley positions only based on the readings of the potentiometers. This correction improves the uncertainty on the trolley position to 2 cm. In studies, we introduced a triangle-shaped position offset as shown in Fig.5.15 with a height of 1°, which corresponds to about 12 cm. Different shapes of the triangle were used and the field values averaged over azimuth before and after putting in the position offsets were compared. The largest difference in the field value was found to be 0.1 ppm.

There is a short time jitter of ±1 cm in the trolley position measurement due to the cable pulling mechanism. The azimuthal average field B_{aver} determined by any one of the 17 probes has an uncertainty due to this jitter together with the average field inhomogeneity of 5 ppm/cm. However some 6000 to 10000 readings are taken with each probe so the overall uncertainty for these B_{aver} values is expected to be less than 0.1 ppm. Since different probes jitter independently, the average dipole moment B_0 is estimated to have an uncertainty due to jitter of less than 0.02 ppm. We assign an error of 0.1 ppm to the field averaged over the azimuth due to the trolley position uncertainty.

One of the measurements of the magnetic field with the trolley center probe is shown vs. azimuth in Figure 5.16. For most of the ring, the magnetic field varies about ±50 ppm. At about 220° in azimuth, the field was $\sim$ 150 ppm higher than the average over the azimuth after the shimming. At the region close to the inflector (at $\sim$ 350° in Fig. 5.16), the residual inflector fringe field, as mentioned in Sec 3.3, reduces the storage ring central field and creates so

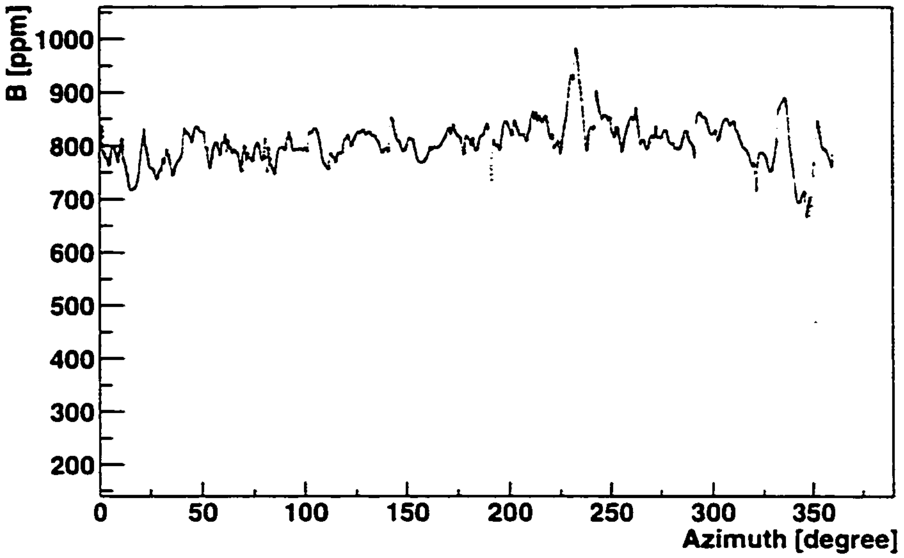

Figure 5.16: The magnetic field measured with the trolley center probe, probe 1, versus azimuth for the measurements taken on February 5 1999. The dip at 350° is due to the inflector fringe field.

large a field inhomogeneity that the NMR signals decay too rapidly to allow a frequency measurement. The regions where the field could not be measured in normal trolley runs extend over about 1° in azimuth for the trolley center probe and about 6° for the probes closer to the inflector. The measurements from probe 1 and 9 are shown in Fig. 5.17. To measure the field in these regions, 9 of the 17 trolley runs were followed by a separate inflector region scan. In these scans, we started the NMR frequency measurement earlier than for the normal trolley run and used shorter time intervals for the measurements. However, the quality of the measurements is not as good as those in the normal trolley runs. Data from these inflector region scans are matched to the normal trolley measurements to provide field measurement in this region. Fig. 5.18 shows the measurements from an inflector region scan.

For 10 trolley probes we have good data through the inflector region from the inflector region scans. However, for probes 1, 3, 7, 8, 9, 10, 11, 12(see Fig. 3.11), there were parts of the inflector region where the measurements failed as shown in Fig. 5.18 for probe 1 and 9. After the 1999 run, we made a special inflector region measurement with a different set of probes connected to one of the fixed probe NMR multiplexer units. Those probes were mounted on a spare trolley which was pulled by hand. The fixed probe NMR units allow us to send a stronger excitation signal to the NMR probes and start the frequency measurement earlier. Therefore we have more time to measure the frequency before the signal decays away. The reference frequency of 61.74 MHz

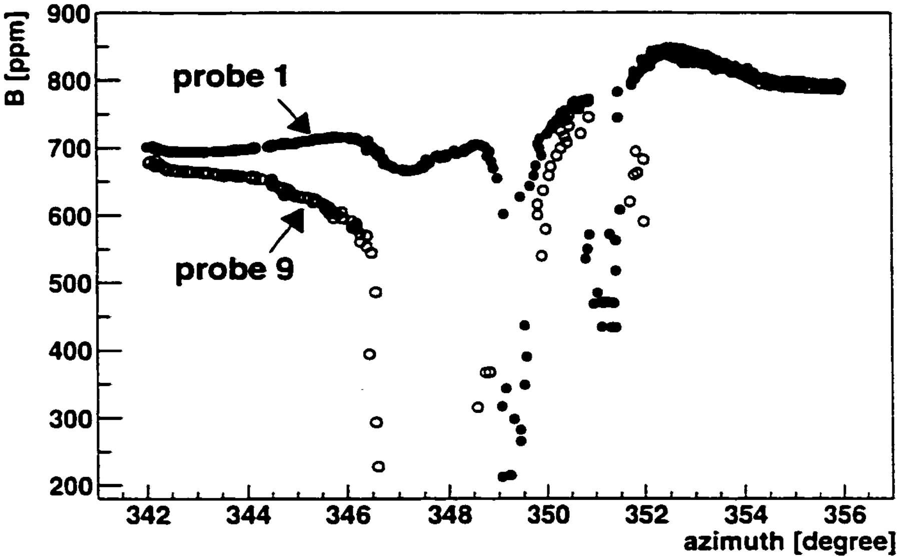

Figure 5.17: The field measurements of two trolley probes in the region near the inflector from a regular trolley measurement. Probe 1 is at the center of the storage region. Probe 9 is 3.5 cm away from the center in the radial direction and is the probe closest to the inflector.

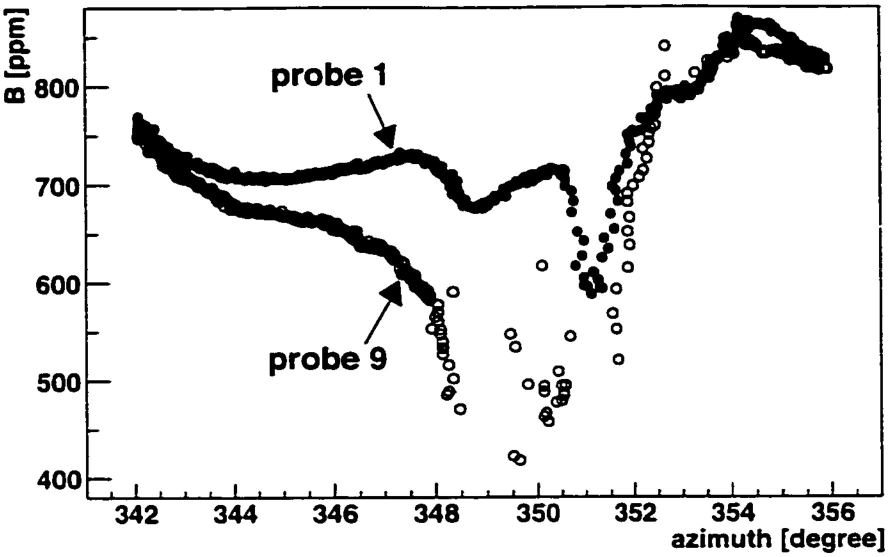

Figure 5.18: The field measurements of two trolley probes from an inflector region scan. Probe 1 is at the center of the storage region. Probe 9 is 3.5 cm away from the center in radial direction and is the probe closest to the inflector.

was also changed. This is because the magnetic field at several locations is more than 1000 ppm lower than its normal value. The NMR frequency of the measurements at these locations is close to and sometimes even lower than 61.74 MHz. Hence, the beat between the NMR signal and the reference frequency has such a long period that the zero crossings cannot be counted before the signal decays away. In this special measurement, the whole region close to the inflector is covered for probes 1, 3, 6, 7, 8, 9, 10, 11, 12 and 15. Probes 6 and 15 are used to compare the measurements from this special measurement and those from the inflector region scan. Because the spare trolley was pulled by hand, the azimuthal positions of the probes can not be determined by the potentiometers. The comparison of the measurements (see Fig. 5.19) from probe 6 in the special measurements and the inflector region scan provides the azimuthal positions for all probes. The field measurements from two probes in the special measurements are shown in Fig. 5.20. The data in the special measurement are used to provide field measurements only in the region in which the field could not be measured in the inflector region scans.

The field measurements are averaged over azimuth for all 17 probes individually.

$$B_{\text{ave}} = \frac{\int B dz}{360} = \frac{\sum_i (B_{i+1} + B_i) \cdot (z_{i+1} - z_i)/2}{360}. \tag{5.9}$$

where the B_i is the field measurement at azimuthal position z_i in degrees and z_i increases as i increases. Then a multipole expansion (Eq. 3.18) is made

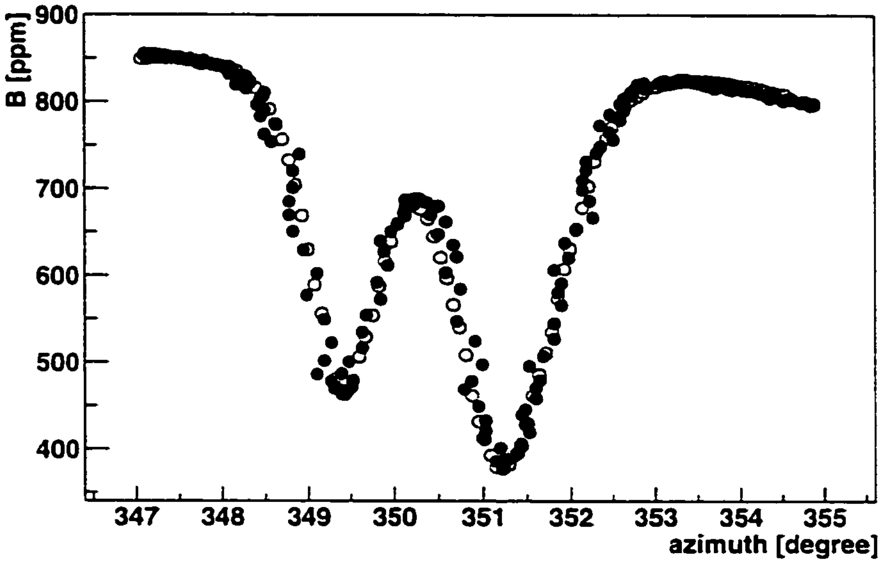

Figure 5.19: The magnetic field measurements by probe 6 in both the inflector region scan and the special measurement with the fixed probe unit. The filled dots are the data from the inflector region scan and the circles are the data from the special measurement with the fixed probe unit. This comparison provide the azimuthal positions for the special measurement.

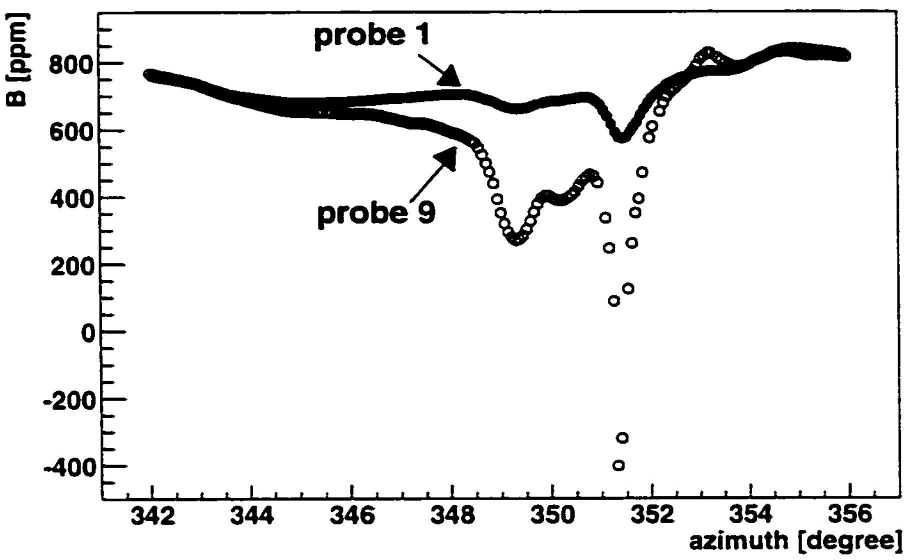

Figure 5.20: The field measurements of two trolley probes from the special inflector measurement. Probe 1 is at the center of the storage region. Probe 9 is 3.5 cm away from the center in radial direction and is the probe closest to the inflector.

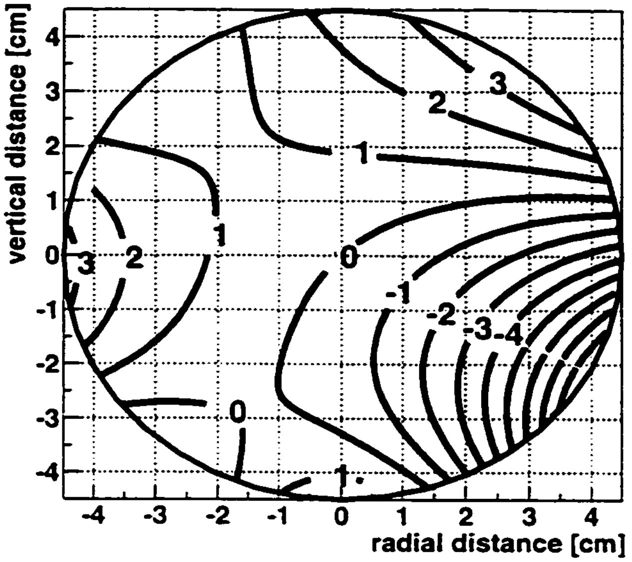

Multipoles [ppm]

	normal	skew
Quad	**-2.23**	**2.17**
Sext	**-1.15**	**2.52**
Octu	**-1.33**	**1.85**
Decu	**0.92**	**0.95**

Figure 5.21: The one ppm contour plot and the multipoles of the azimuthal average of the field measured in a trolley run.

from the average field measurements of 15 trolley probes. Data from probes 3 and 8 are discarded for the reasons mentioned before. A one ppm contour plot and the multipoles of the azimuthal average of the field measured in one trolley run are shown in Figure 5.21. On average over all trolley runs, the dipole moment B_0 is 0.04 ppm lower than the average field measured by the trolley center probe. This is due to the errors of the calibrations of the trolley probes.

The trolley measures the magnetic field in the muon storage region outer to a radius of 3.5 cm. The magnetic field beyond 3.5 cm radius is obtained by extrapolating the measured moments up to and including the decupoles. Data obtained in 1998 with the shimming trolley, which has 25 NMR probes and measures the field outer to 4.5 cm radius (Fig. 5.22), are used to evaluate the field in the outer region and the higher multipoles. The multipole expansions of the shimming trolley data at six azimuthal positions, some at the edges of poles and others at the pole centers, all give less than 8 ppm at 4.5 cm for 12th and 14th order multipoles. One example of the multipole expansion of the shimming trolley measurement is shown in Fig. 5.23. The structure of our magnet does not have high order symmetries so that the magnetic field does not have significant high order multipole moments. If we assume a 8 ppm 12th order multipole at 4.5 cm and multiply its radial dependence by the muon distribution (see Sec. 5.9), we find a maximum effect of 0.03 ppm on the field averaged over the muon distribution. Hence, the error on the field due to the neglect of high order multipoles is negligible. Calculations of the field of the

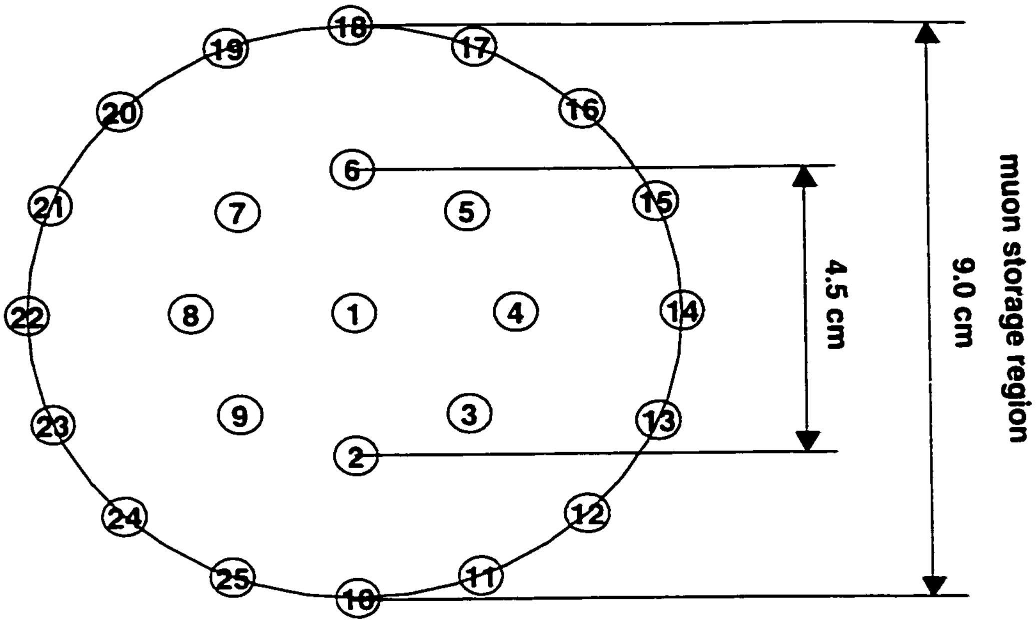

Figure 5.22: The positions of probes mounted on the shimming trolley.

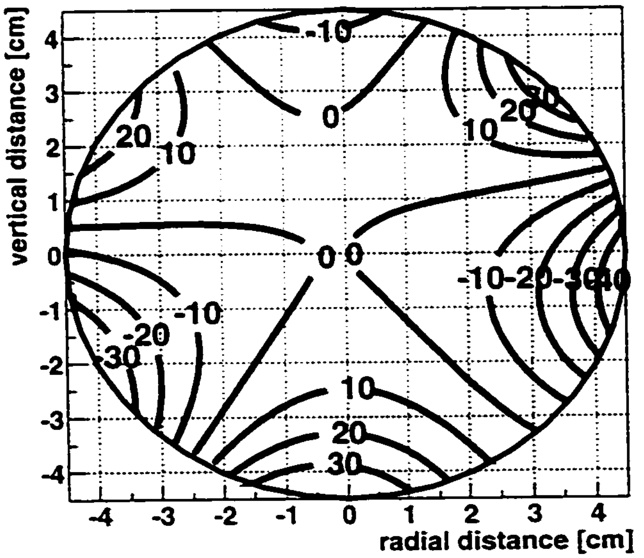

Multipoles (ppm)

	normal	skew
Quad	-1.89	28.58
Octu	-19.20	-5.15
Sext	-9.45	-8.14
Decu	-7.96	-4.27
12th	-7.02	-2.56
14th	-3.32	-2.15

Figure 5.23: The 10 ppm contour plot and the multiples of the field measurements from the shimming trolley at an azimuthal location.

magnet gives the same conclusions[62].

5.6 Tracking of the field with the fixed probes

The magnetic field between trolley runs is determined by measurements with the fixed probes. The determination of the NMR frequency from the probes is discussed in 5.2.

After the determination of the NMR frequencies from the fixed probes, we separate the fixed probes into three groups according to the qualities of the measurements, good probes, suitable probes, and bad probes. Fig 5.24 shows the readings from a typical probe from each group.

The average magnetic field over the ring is determined by the weighted average of the measurements from the selected good and suitable fixed probes,

$$B_{\mathrm{fp}} = \frac{\sum w_z B_z}{\sum w_z}, \tag{5.10}$$

where w_z is the weight assigned to the set of fixed probes at the azimuthal location z and B_z is the average of the measurements from the selected fixed probes at that location. The magnetic field near the azimuthal center of the magnet poles changes with the distance and the angle between the top and bottom pole. The magnetic field near the edge of the magnet poles is sensitive to the change of the gaps between two adjacent poles, and the distance and the angle between top and bottom poles. However, the field change due to the change of the gaps is a local effect. Hence, the field change measured by the probe at the edges of the poles should have less weight in calculating the average field compared to the field change measured by the probes at the azimuthal center of the poles. In Eq. 5.10, the weight, w_z, can have two values, w^1 if the probe set is located near the azimuthal centers of the magnet poles or w^2 if the set is located near edges of the magnet poles. The sum of all weighting factors, w_z, is set equal to one and the determination of the ratio between w^1 and w^2 will be discussed in next two paragraphs. The total weight on the probes above the storage region is the same as that on the probes below the storage region in the probe selection.

We calibrate B_{fp} with respect to the dipole moment, B_0, from the trolley measurements. It takes 1–2 hours for the trolley to run around the ring and the magnetic field without feedback can change by up to several ppm during this duration. The field measurements of each fixed probe has to be taken at the time when the trolley passed that probe. Since the trolley perturbs the field readings of nearby fixed probes, we use the average of the fixed probe readings before and after the perturbation peak. This is shown as time intervals I_1 and I_2 in Fig. 5.13. The durations of I_1 and I_2 are 300 seconds. The time interval, Δt in Fig. 5.13, was varied. Fig. 5.25 shows the average field from the fixed probes versus this time interval. The peak at early times and the dip around 110 seconds are caused by the trolley passage. For $\Delta t > 250$ seconds, the

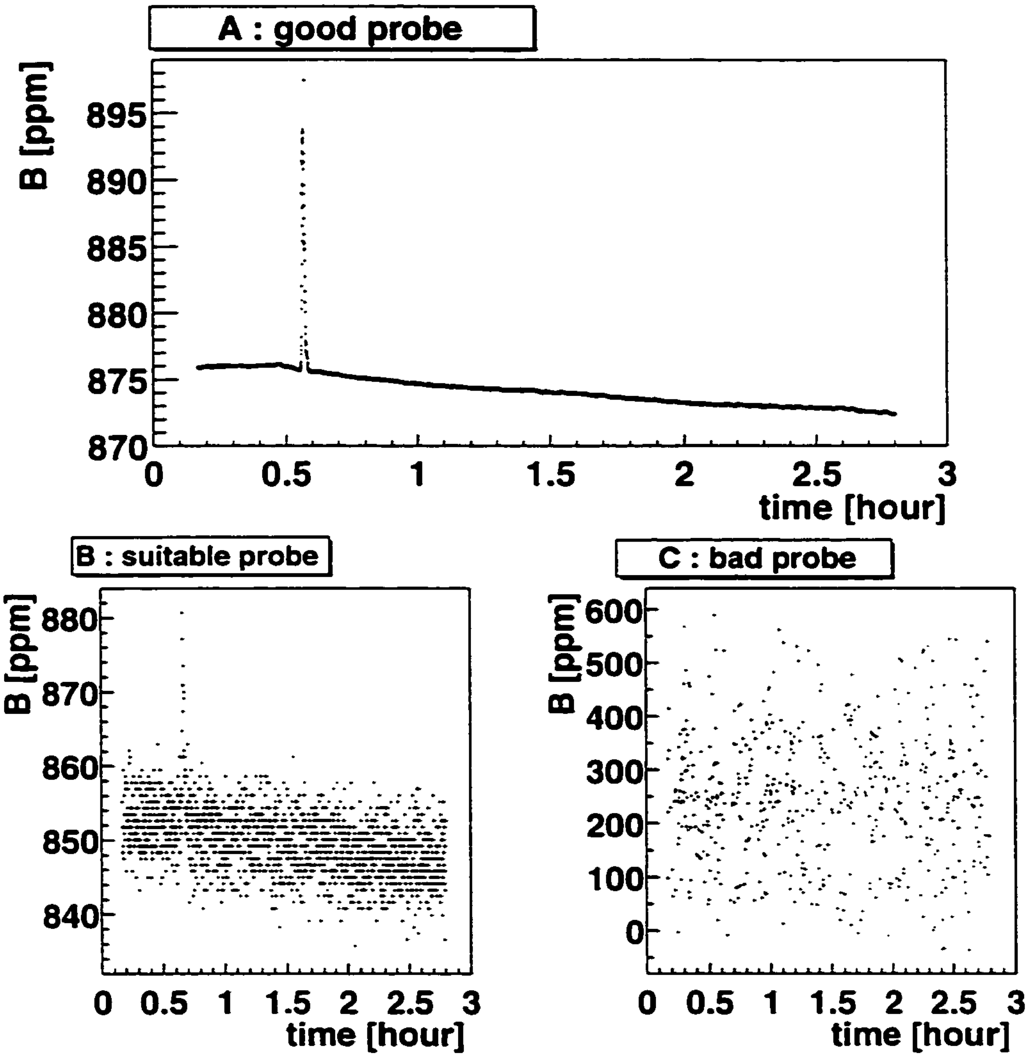

Figure 5.24: In A the readings of a good probe during a trolley run are shown vs. time. The spike occurs when the trolley passes the location of the probe. In B the readings of a suitable but less good probe are shown. In C the readings of an unusable probe are shown.

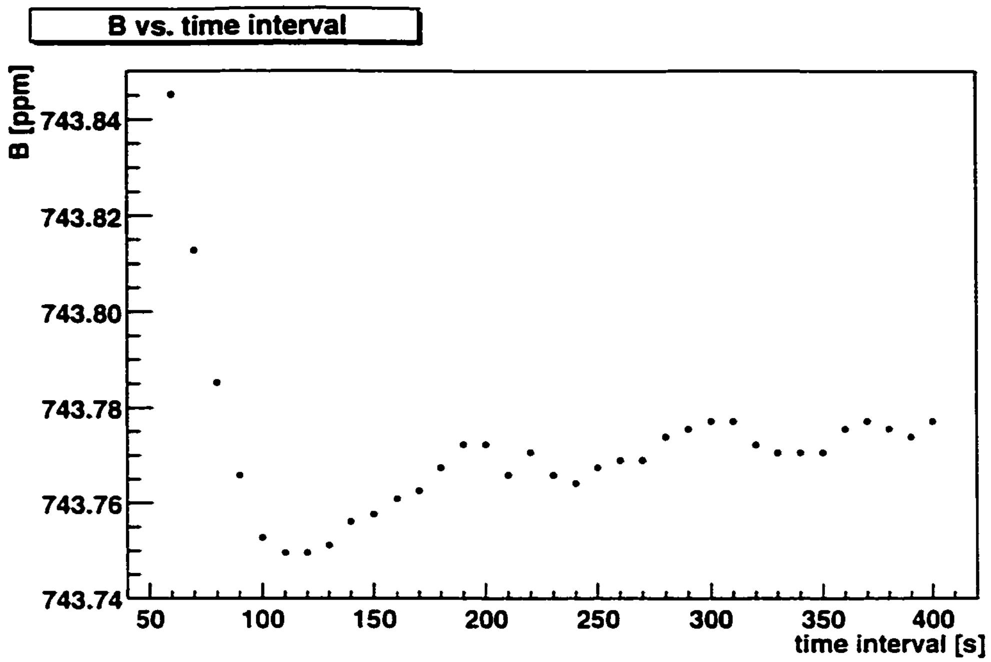

Figure 5.25: The average field from fixed probes versus the time interval, Δt in Fig. 5.13. The peak and the dip at early times are caused by the trolley nearby.

fixed probe average is not inflenced by the trolley and is constant to within 0.02 *ppm*. We use a time interval of 300 seconds as shown in Figure 5.13.

Ideally, $B_{\rm fp}$ and B_0 from the trolley measurement are fully correlated. Therefore, the difference between the two values, the calibration of $B_{\rm fp}$, would be a constant. Ramping of the magnet, however, can change this calibration because of the residual eddy currents in the yoke. To achieve the best correlation, we calculated the differences of the calibrations for pairs of adjacent trolley runs taken in the same magnet-on period. There are 11 such pairs in the 17 trolley runs in 1999, and the distribution of the 11 differences is shown in Fig. 5.26. The ratio of the weighting factors, w^1 and w^2, for the fixed probes are chosen to minimize the root mean square (*rms*) of these differences. Figure 5.27 shows the *rms* vs. the total weighting factor for all probes which are at the pole centers. A minimum *rms* of 0.21 ppm is reached for a weighting factor of 0.57 for the probes at the pole centers and 0.43 for the probes at the edges of the poles. A weighting factor larger than 0.5 for the probes at the center of the poles was expected because the field changes near the edges of the poles are more localized than the field changes near the center of the poles. Since the shapes of the poles and the yokes change with the temperature and with its gradient in the magnet as discussed in section 5.3, the optimal weighting factors may change when the temperature or its gradient changes. We estimated the temperature effect on the weighting factor by using data

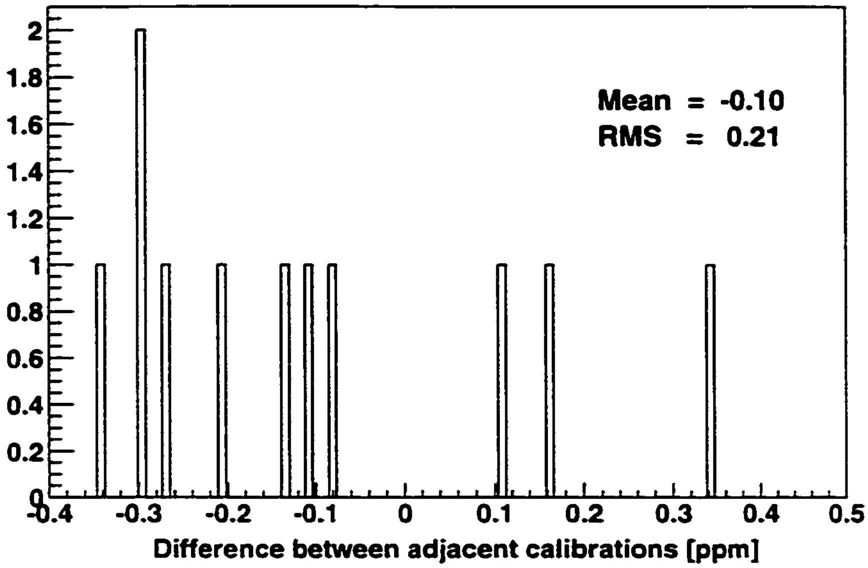

Figure 5.26: The distribution of the differences of the calibrations of B_{fp} with respect to B_0 for 11 pairs of adjacent trolley runs taken in the same magnet-on periods.

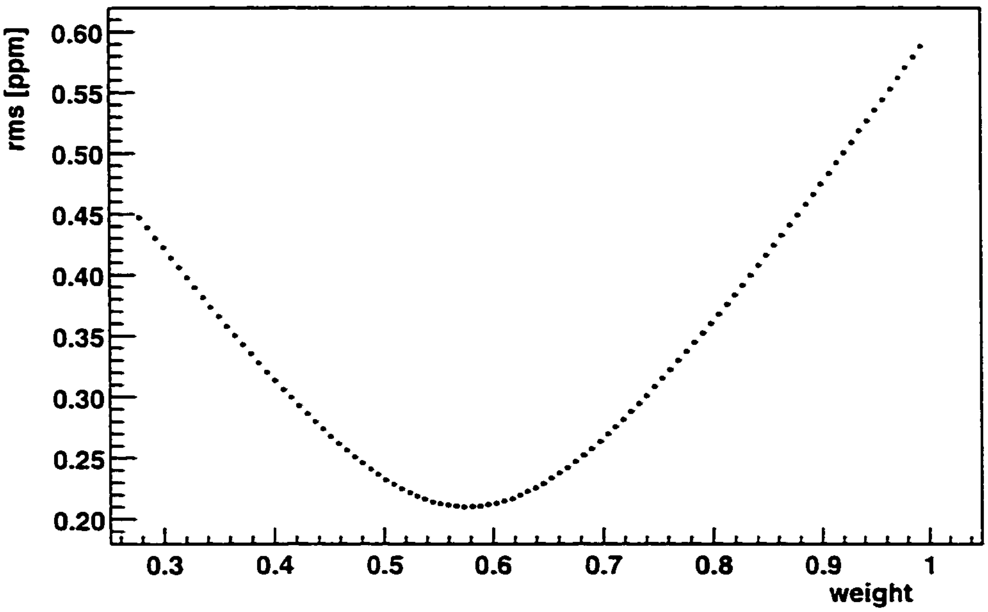

Figure 5.27: The *rms* of the difference of the calibration of the average field measured with fixed probes vs the weighting factor given to the probes at the center of the poles. The minimum of 0.21 ppm is reached for a weighting factor of 0.57.

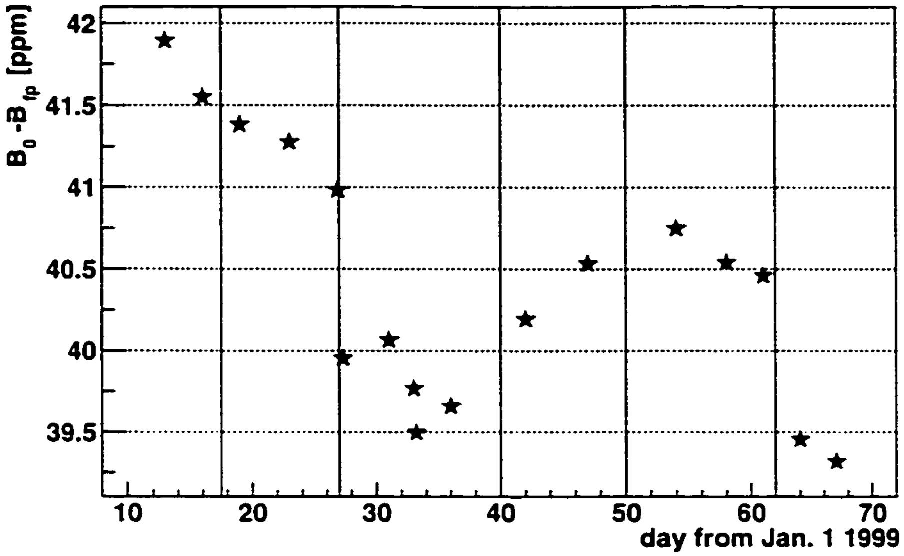

Figure 5.28: Calibrations of $B_{\rm fp}$ with respect to B_0 from the trolley measurements for the 17 trolley runs in 1999. The vertical lines indicate the time when the magnet was ramped.

from trolley runs taken at different temperatures and assuming that

$$w^1 = w_0^1 + a(T - T_0), \qquad w^2 = 1 - w^1. \tag{5.11}$$

where w_0^1 is the value for w^1 at temperature T_0 and a is a coefficient which can be changed to achieve the minimum *rms* of the differences of the calibrations of $B_{\rm fp}$. The minimum *rms* is reduced by 0.005 ppm, which is negligible. The temperature gradient effect is estimated by using the values of the normal quadrupole field component from the trolley measurements, which depends linearly on the temperature gradient as discussed in section 5.3. The minimum *rms* changes by 0.01 ppm, which is negligible as well. The optimum *rms* value of 0.21 ppm stems from the difference of paired calibrations. Hence, the error on individual calibrations amounts to $0.21/\sqrt{2} = 0.15$ ppm. Figure 5.28 shows the calibration of the average field measured by the fixed probes, using the optimal weighting factors. To interpolate the calibration between the trolley runs in the same magnet-on period, we use both a linear interpolation and an average value of all calibrations in that period. The results from the two methods agree with each other to within 0.1 ppm.

There is a special period in our 1999 run on Feb. 15 and 16, during which the surface coil currents were different from the normal settings due to a failure of one of the surface coil power supply modules. The field $B_{\rm fp}$ changed, as shown in Figure 5.29. The calibration of $B_{\rm fp}$ with respect to B_0 also changed because the fixed probes are much closer to the surface coils than the trolley

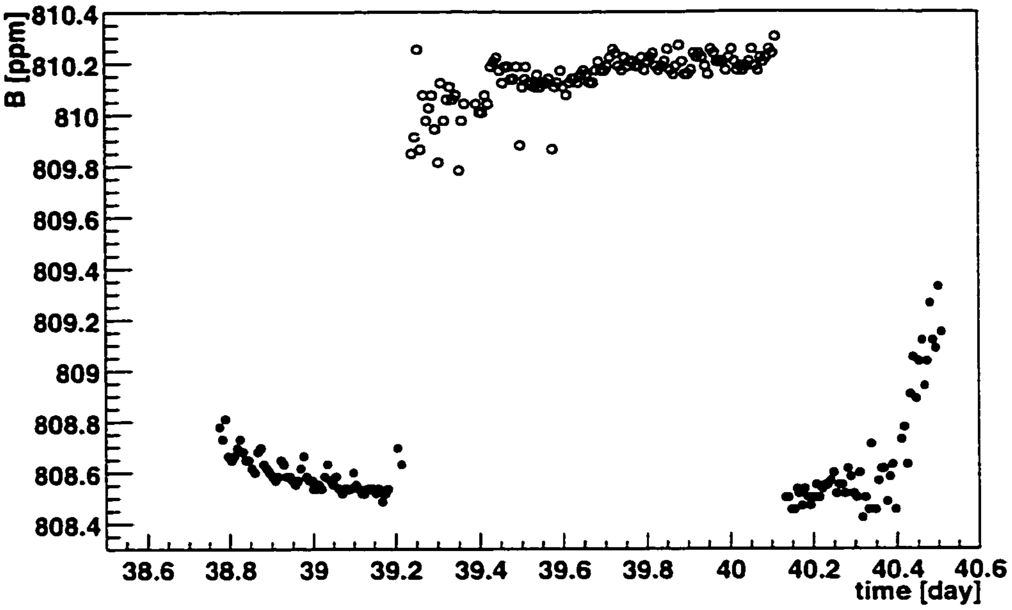

Figure 5.29: The field B_{fp} over 10 minutes versus time. The circles are the data taken when the surface coil currents were different from the normal settings.

probes. We don't have a complete trolley run with these special surface coils currents. We obtain the calibration from a trolley measurement which covers about one half the storage ring in azimuth taken on Feb. 10 when the same surface coil power supply module failed in the same way, as illustrated in Figure 5.30 from measurements with a pair of fixed NMR probes. Since the surface coil currents flow around the ring in azimuth at the same radius, their effect on the field measured by the trolley should be almost the same at different azimuthal locations. This feature allows us to obtain a reasonably accurate calibration value of B_{fp} with respect to the B_0 by using the trolley measurement over only part of the ring. The calibration is found to be increased by 9.3 ppm when the surface coil power supply module failed. The error in this calibration is estimated to be 0.5 ppm, rather than 0.15 ppm for the normal calibrations. Since 4.8%, 53.5 million, of the analyzed decay positrons were collected in this period, the total correction on the average field weighted by the positron number is 0.45 ± 0.02 ppm.

The multipoles of the field also changed when the surface coil power supply module failed as shown in Figure 5.31. The largest change is that of the normal quadrupole, which increased by 6.23 ppm at 4.5 cm. The radial displacement of the equilibrium muon distribution from the center of the storage ring is 3.7 mm as discussed in detail in Sec. 5.9, and hence the contribution from the change of the normal quadrupole to the average field weighted by positron number is $6.2 \times 3.7/45 \times 4.8\% = 0.024$ ppm.

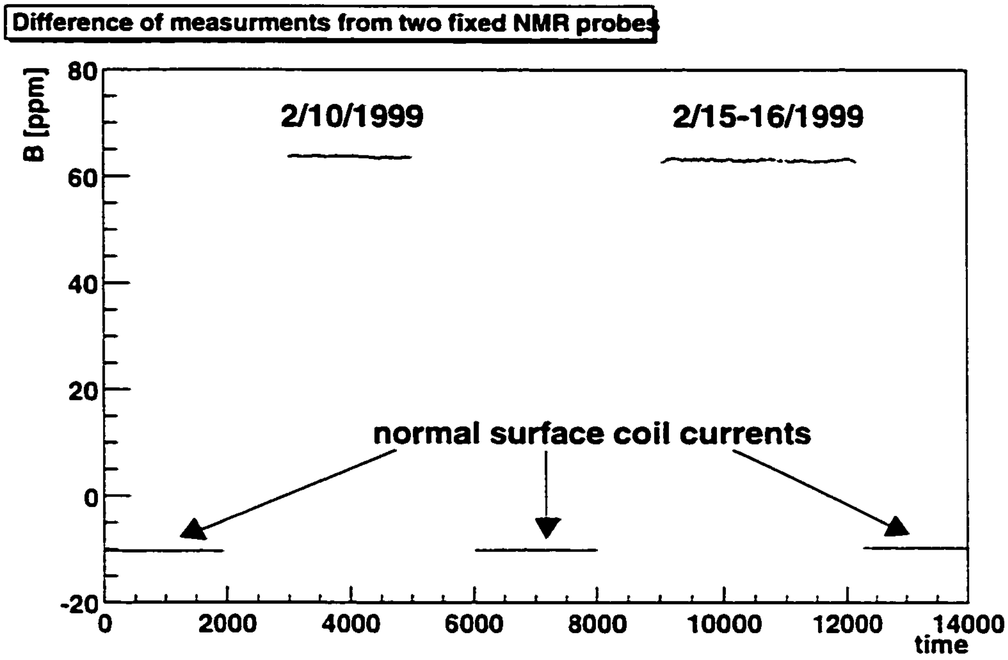

Figure 5.30: The difference between the measurements from two fixed NMR probes. These probes were located on a top pole at the same azimuthal position. The radial distance between the probes was 3 cm. The surface coils connected to the failing module were located between the probes. As expected, this same behavior was found at other azimuthal positions. The time axis is in an arbitrary units.

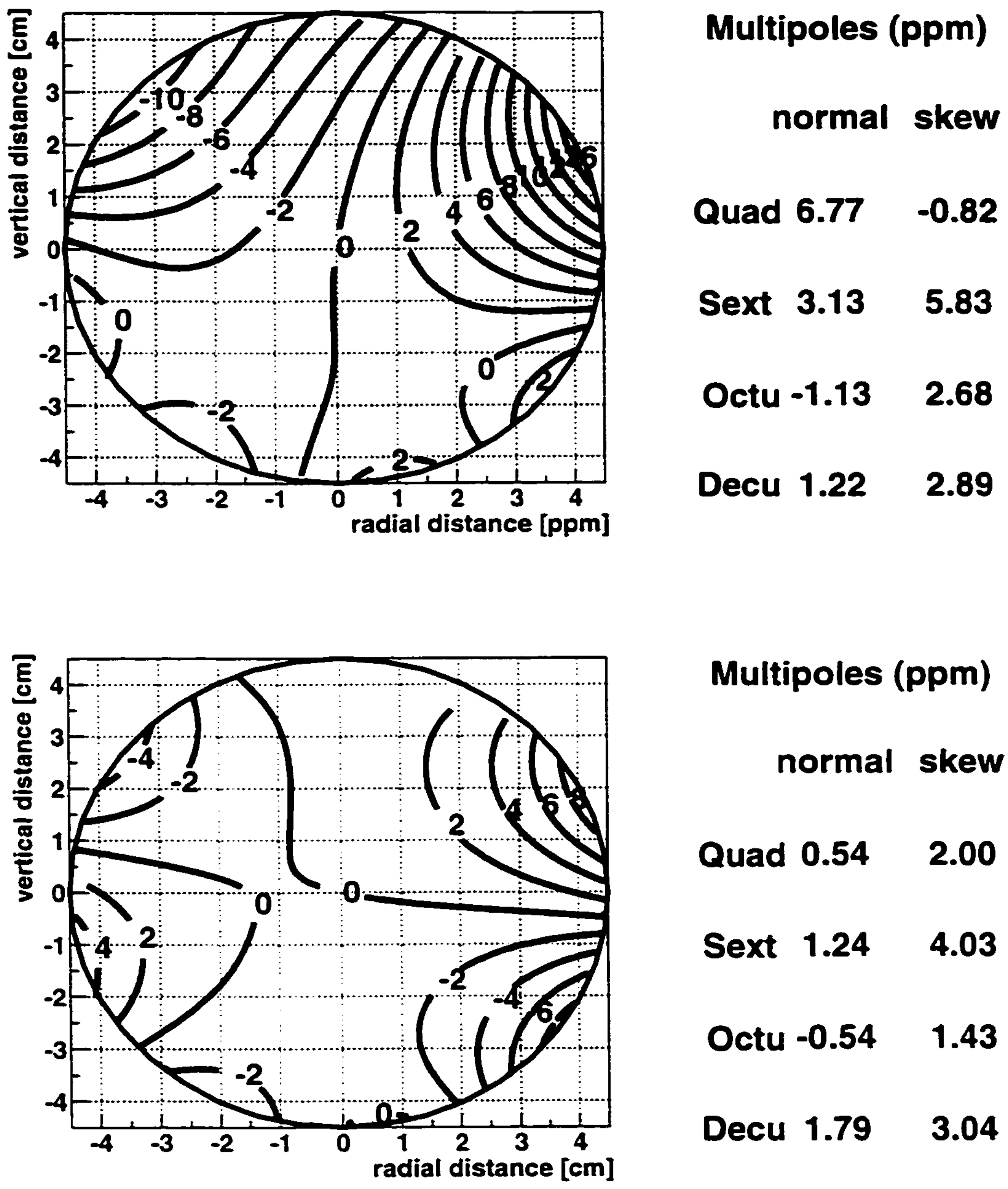

Multipoles (ppm)

	normal	skew
Quad	6.77	-0.82
Sext	3.13	5.83
Octu	-1.13	2.68
Decu	1.22	2.89

Multipoles (ppm)

	normal	skew
Quad	0.54	2.00
Sext	1.24	4.03
Octu	-0.54	1.43
Decu	1.79	3.04

Figure 5.31: The multipole expansions of the field averaged over about half of the storage ring in azimuth. The top plot shows the measurements from the trolley run on Feb. 10 1999 when the surface coil currents were away from the normal setting. The bottom plot shows the measurements from the trolley run on Feb 12 1999 with the normal surface coil currents setting.

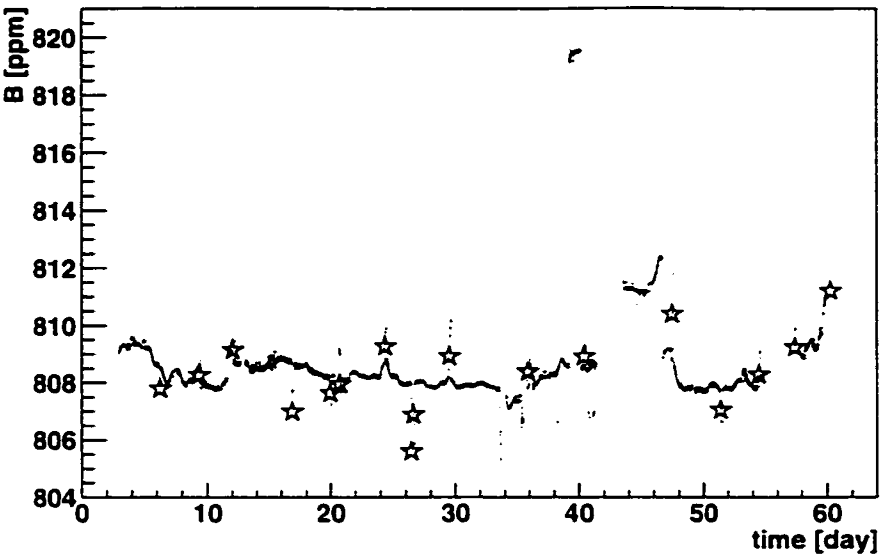

Figure 5.32: The magnetic field averaged over 10 minutes vs. time. Between days 15 and 40 positron data-taking took place. The spikes in B on days 38 and 39 are due to a change of currents in the surface coils. The stars show B_0 from trolley runs.

Fig. 5.30 shows that the difference of the measurements from individual probe changed by about 70 ppm when the average field only changed by about 2 ppm as shown in Fig.5.29. Since the individual fixed probe measurements are more sensitive to this type of magnetic field change than the average, individual probes measurements were used in checking for other such field changes. The magnet logbook was also checked. No other unexpected field change were found.

Figure 5.32 shows the time dependence of the field average for every ten minutes of the 1999 data. The spikes on days 38 and 39 are due to a change of currents in the surface coils mentioned above.

5.7 Cross checks on the analysis

Two largely independent analyses, I and II, of the magnetic field were made for 1999 to verify the calculations and to cross check several other aspects. Analysis I is discussed above. In the following, we detail the different choices made by two determinations of the field values, and compare the results. The assessment of systematic errors is common to both analyses.

Trolley measurements

- Unlike analysis I, analysis II averages the trolley position readings over a time interval of typically 10 s during which the trolley moves by about 6 cm. This improves the position resolution and reduces noise, but may introduce a bias if the trolley speed varies.

- Analysis I uses the inflector region scan matching the trolley run to fill in the data gap caused by the inflector fringe field, whereas analysis II uses one representative inflector scan. In addition, the angular intervals filled with the inflector scans are different.

- Analysis II excludes data from trolley probe 12 after observing that a multipole expansion up to the decupoles provides a better fit to the data without this probe. Although this changes the amplitude of some of the multipoles, the change in the average field seen by the muons is at the 0.01 ppm level.

- Analysis I corrects the trolley position measured by cable lengths using fixed probe data collected during the corresponding trolley run. Analysis II averages over all trolley runs to determine the position correction and thereafter applies its result to each run. Analysis II is the preferred choice if the accuracy of the correction for a single run is worse than the reproducibility of the effect; Analysis I is the preferred choice if the position correction varies significantly with time.

Figure 5.33 shows the comparison of the dipole moments, B_0, from the two analyses. The results agree within 0.05 ppm for all trolley runs.

Fixed probe measurements

- Analysis I and II independently select a subset of the fixed probes for tracking. The selection of 122 probes in analysis I has a better geometrical symmetry, whereas the selection of 148 probes in analysis II contains more probes.

- Since the trolley body perturbs the readings of a fixed probe while it passes, the field readings of the fixed probe are interpolated to obtain its calibration. Analysis I uses time intervals around the peak of the perturbation, whereas analysis II uses angular intervals symmetric with respect to the angle at which trolley probe passes the fixed probes.

Analysis II independently analyzed the surface coil current change due to the failure of one surface coil module. Two analyses select different sets of fixed probes to calculate B_{fp}. Different fixed probes observed different field changes depending on their locations. Hence, two analyses have different correction to the calibration of B_{fp} with respect to to B_0. The values of B_{fp} before and after the correction are shown in Fig. 5.34. The results agree with each other after the correction.

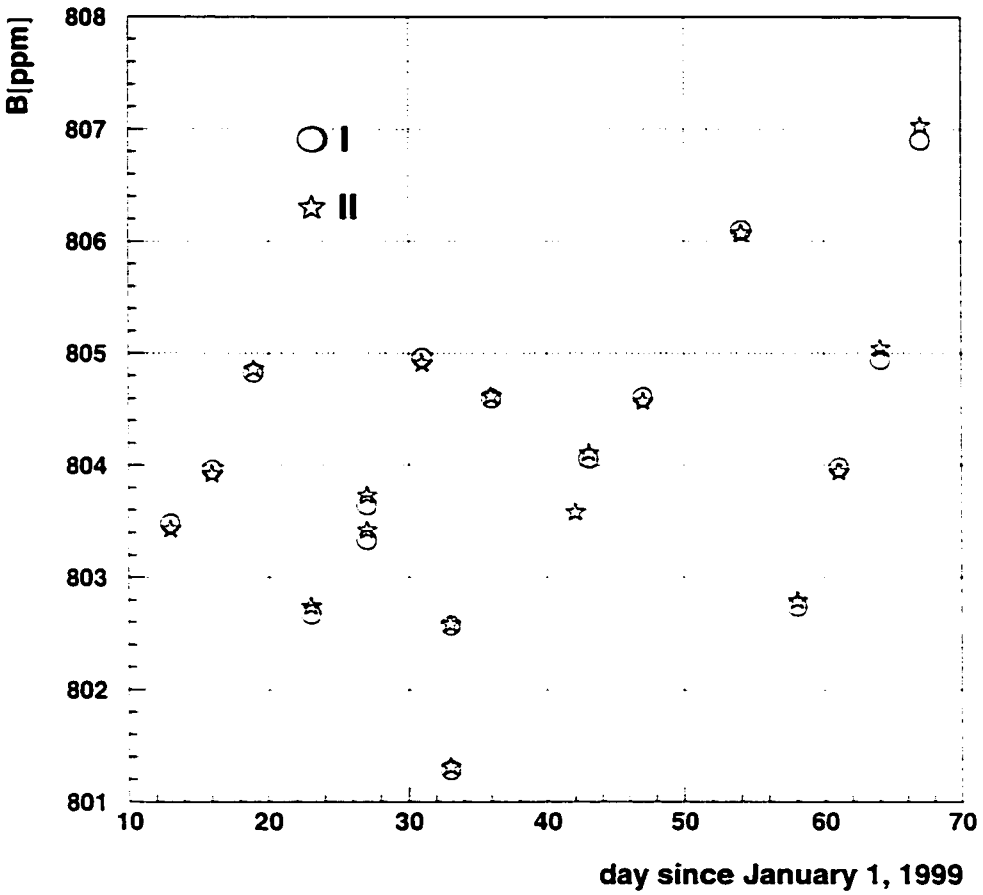

Figure 5.33: The comparison of the dipole moments, B_0, from trolley measurements between two independent analyses I and II. The trolley run on day 42 is not used in analysis I.

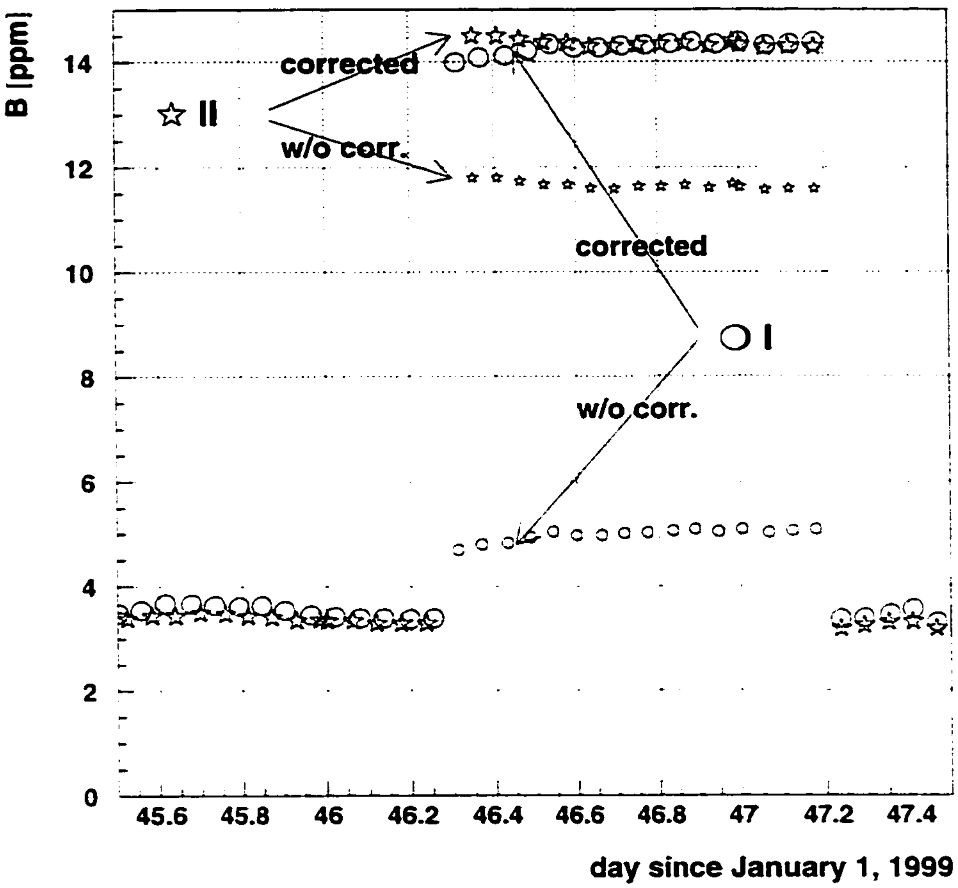

Figure 5.34: The comparison of the magnetic field determined by two analyses during the period of the surface coil power supply failure. The large difference between two analyses before the correction is because the two analyses use different sets of fixed probes to determine average field and different probes observed different field changes depending on their locations. Only representative samples of the average fields are shown in the figure.

5.8 AGS stray field and the kicker eddy currents

Because of the high precision required in the measurement of the magnetic field, the stray field from the AGS magnets was considered. When protons were injected into the AGS, the magnets in AGS were ramped to full current. The protons were sent to our experiment and the muons were stored and measured. The AGS magnets were ramped down after all proton bunches were extracted. The period of a full cycle is 2.5 s in the 1999 run and the time between two adjacent extractions of protons was 33 ms. From the first extraction to the last extraction, the AGS magnets were kept on to store the protons. Hence, the AGS magnets were on with full currents for about $0.033 \times 6 = 0.198$ s during the 2.5 s period. The stray field from the AGS magnets may change our magnetic field directly. The change of the magnetic flux of the stray field through our storage ring introduce currents which also influence our magnetic field.

Our NMR system measured the average magnetic field over the AGS period of 2.5 s because the measurements were not synchronized to the AGS cycle. However, muons were only stored in our storage ring when the AGS magnets were on with full current. Hence, there potentially is a difference between the magnetic field we measured with the NMR system and the magnetic field in which the muon spin precessed.

We have a so-called T0 counter in front of the inflector entrance to record the time when the muons entered the storage ring. The T0 counter used the same clock as the measurements of the magnetic field. Hence, we know whether a magnetic field measurement was taken between the time of the first and last injection of the muons in one AGS cycle when the AGS magnets were on. We calculated the difference between the magnetic field measurement with the most recent previous measurement when the AGS magnets were on. Figure 5.35 shows this difference of the field obtained by averaging the data from one fixed probe over about 2.3×10^5 AGS cycles. The effect varies depending on the location of the fixed probe. The largest effect is about 30 ppb. The total effect on the B field due to the AGS stray field is about 0.01 ppm.

The magnetic field of the kicker eddy currents, which are created in the vacuum chamber wall, decays after the kickers are turned off. The measured eddy current effect is shown in Fig. 5.36. The residual eddy current effect, measured locally by Farady effect(see Sec. 3.6), was slightly higher than 0.1 ppm level at 20 μs on the field averaged over azimuth, B_0. Because we start our measurement of $g-2$ after 30 μs, this effect is less than 0.02 ppm[57].

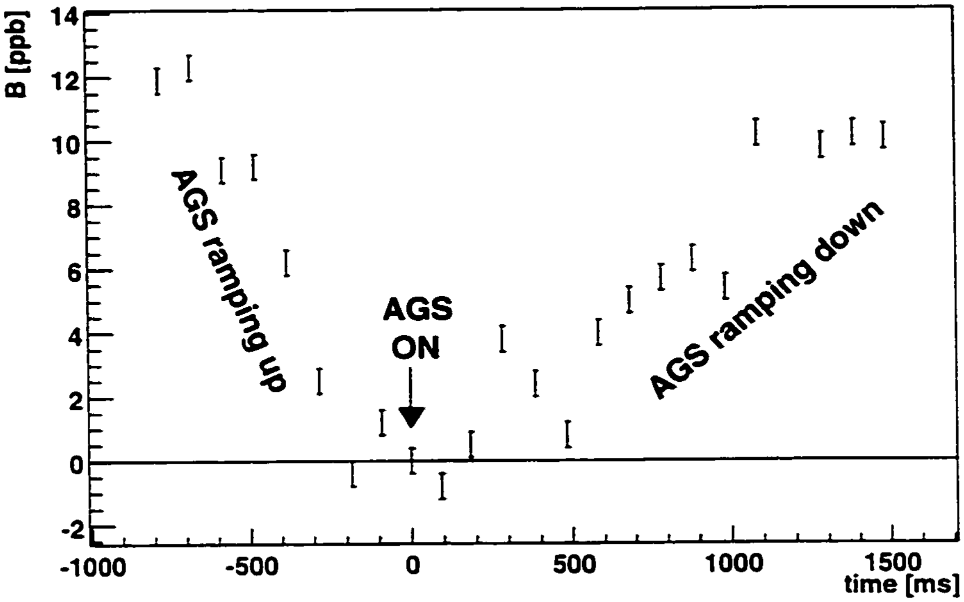

Figure 5.35: The change of the magnetic field measured by one fixed probe during an AGS cycles. These results were obtained by averaging over about 2.3×10^5 AGS cycles. Within one AGS cycle, the magnetic field changed by about 10 ppb for this probe.

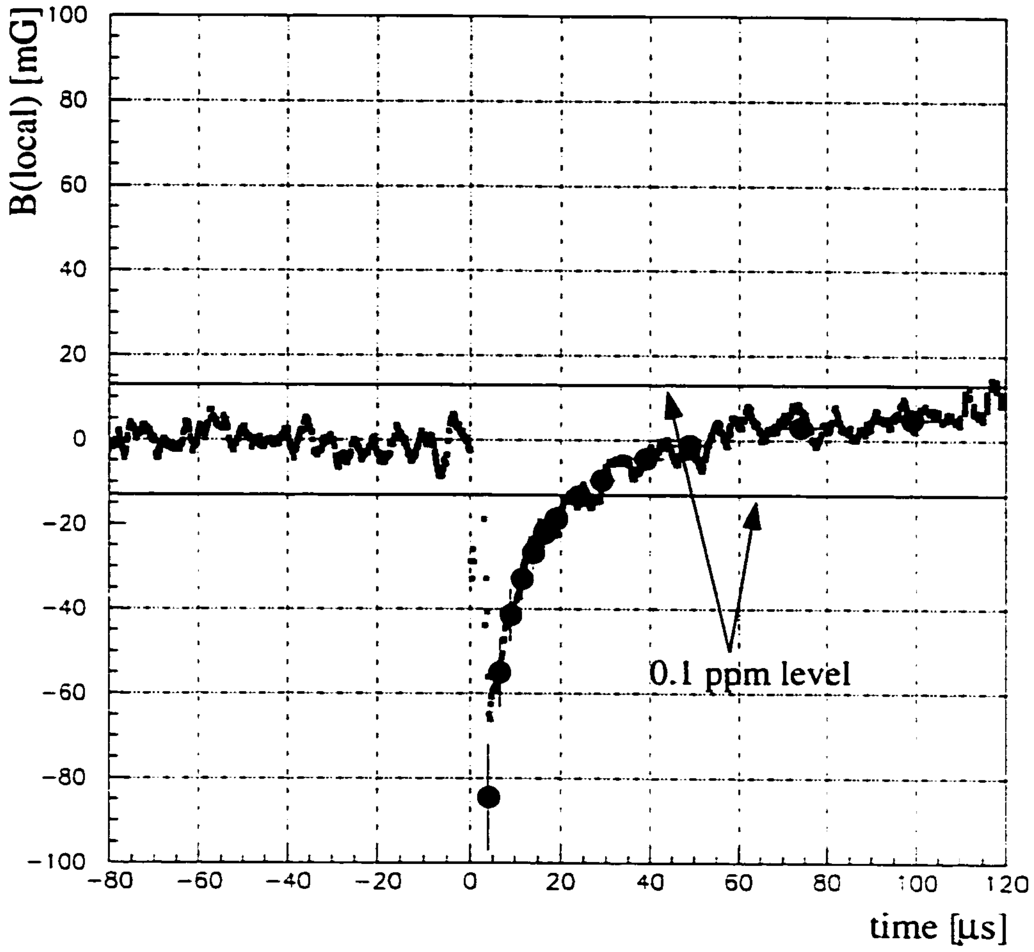

Figure 5.36: The local magnetic field of the kicker eddy currents measured by Farady effect. The small stars show the measurements and large dots shows the prediction from calculations. The two horizontal lines indicate the level at which the effect on the magnetic field averaged over azimuth. B_0. is 0.1 ppm.

5.9 Muon Distribution

The magnetic field weighted by the muon distribution

$$\tilde{B} = \int\int B(x,y)\mu(x,y)dxdy, \tag{5.12}$$

where $\mu(x,y)$ is the equilibrium muon distribution in radial(x) and vertical(y) direction.

In our storage ring, the injected muons start in 50 ns bunches and debunch with a decay time of about 20 μs due to their 0.6% momentum spread. Shortly after injection when the beam was not fully debunched, the detectors observe a change in the number of decay positrons due to their bunch structure, the so called fast rotation. The fast rotation has a period of about 149.2 ns which is the muon cyclotron period in our storage ring. Fig. 5.37 shows the fast rotation observed in one detector. Because muons in our storage ring are ultra relativistic, the fast rotation period of a muon is proportional to the radius of its equilibrium orbit as

$$T_{\mathrm{fr}} = 2\pi r/(\beta c), \tag{5.13}$$

where c is the speed of light. Hence, the radial equilibrium muon distribution can be obtained from analysis of the debunching of the beam due to different T_{fr}[63]. The fast rotation analysis of the 1999 data shows that the radial position of the equilibrium center of the muon distribution $< r >= r_{\mathrm{magic}} +$ 3.7 mm with an error of 1.0 mm, where $r_{\mathrm{magic}} = 7112$ mm is the center of the storage region determined by the electrostatic quadrupoles and the collimaters. The mean square of the orbital displacements $< (r - r_{\mathrm{magic}})^2 >= 1.107$ cm^2. The radial distribution of the muons is shown in Fig. 5.38. An independent fast rotation analysis of 15% of the 1999 data gives a result that agrees with this result. The average normal quadrupole field component measured by the trolley is -1.8 ppm at 4.5 cm. Hence the magnetic field at the beam center

$$\tilde{B} = B_0 + a_1\frac{r_{\mathrm{beam}}}{r_0} = B_0 - 1.8 \times \frac{3.7}{45} = B_0 - 0.15 \text{ ppm}. \tag{5.14}$$

where a_1 is the normal quadrupole moment. The error is 0.04 ppm due to the 1 mm uncertainty in the radial beam position. Studies of the data from the FSD indicate that the beam shifted upwards by 2 mm with respect to the position at the beginning of the run. The beam was vertically centered within 1 mm by maximizing the number of stored muons with the radial magnetic field at the beginning of the run as discussed in Sec. 4.2. Hence, we estimate the vertical beam center to be 2 ± 2 mm and then

$$\tilde{B} = B_0 + b_1\frac{r_{\mathrm{beam}}}{r_0} = B_0 = 2.7 \times \frac{2}{45} = B_0 + 0.12 \text{ ppm}. \tag{5.15}$$

where $b_1 = 2.7$ ppm at 4.5 cm is the average skew quadrupole field component measured by the trolley. The error on this correction is 0.12 ppm. In total, the magnetic field at the beam center is 0.03 ppm lower than B_0.

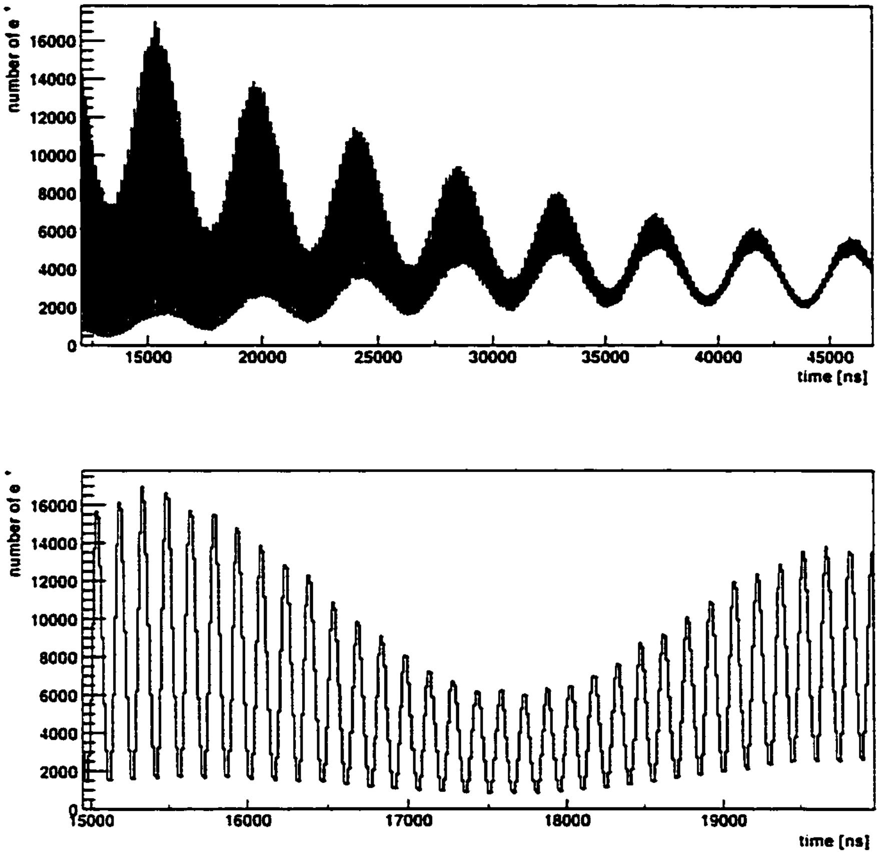

Figure 5.37: The figures show the fast rotation structure in the time spectrum of the decay positron from one detector. The top plot shows that the fast rotation structure dominates at early times and then decays. At late times, the $g-2$ oscillation dominates. The bottom plot shows the fast rotation structure in more detail.

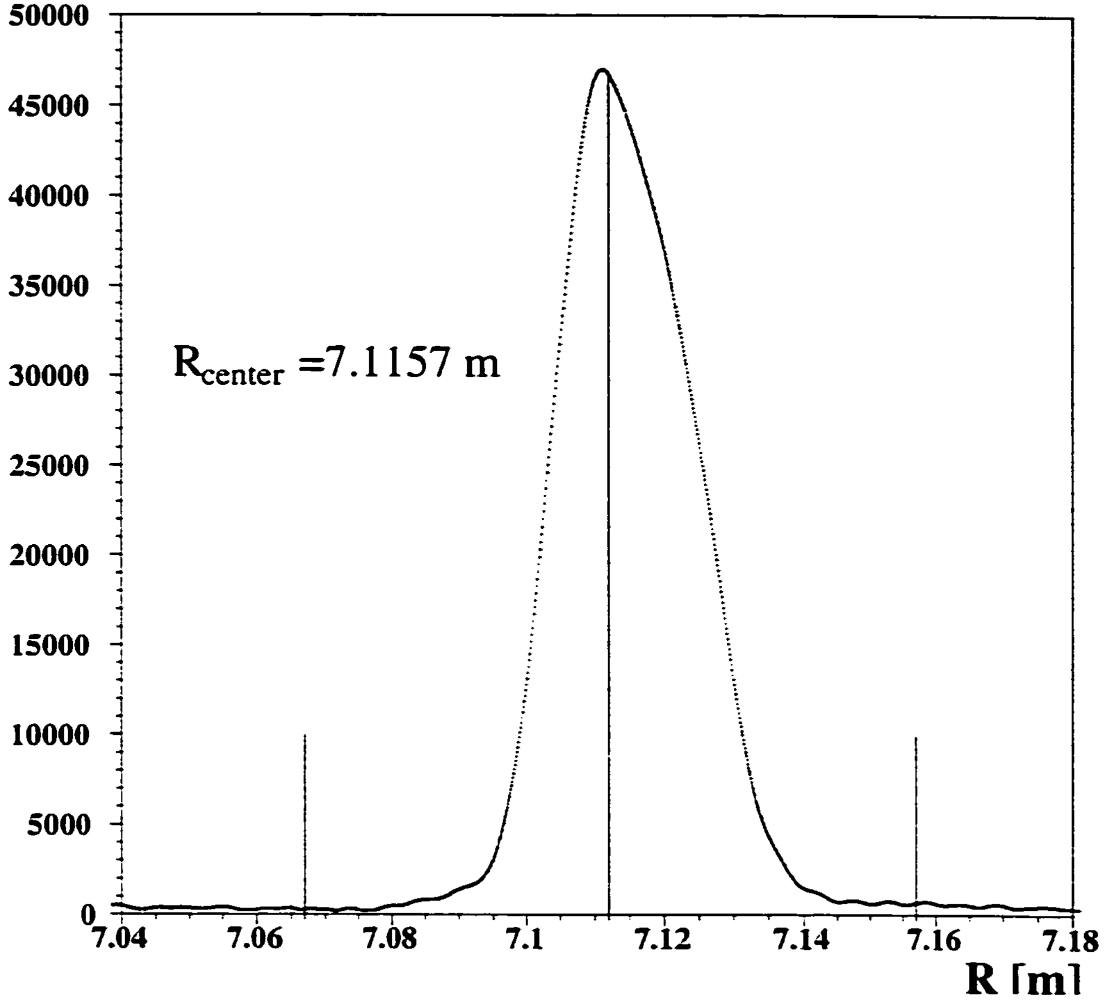

Figure 5.38: The distribution of the muon radial equilibrium orbit. The line at 7.1157 m marks the center of the distribution. The center of the storage region is at 7.112 m and the lines at 7.112 ± 0.045 m mark the edge of the aperture of the storage region.

Table 5.1: Systematic errors for the $\langle\tilde{\omega}_p\rangle$ analysis of the 1999 data

Source of errors	Size [ppm]
Absolute calibration of standard probe	0.05
Calibration of trolley probes	0.20
Trolley measurements of B_0	0.10
Interpolation with fixed probes	0.15
Inflector fringe field	0.20
Uncertainty from muon distribution	0.12
Others †	0.15
Total Systematic Error on $\langle\tilde{\omega}_p\rangle$	0.4

† Higher multipoles, trolley temperature and its power supply voltage response, and eddy currents from the kickers.

The magnetic field seen by muons was calculated in software by tracing a sample of muons through a measured field taken in 1998 (The very small change in field for 1999 as compared to 1998 does not change the muon dynamics significantly), and by averaging the field values these muons encounter. The calculation shows that the resulting average field agrees to within 0.05 ppm with the field value at the beam center and averaged over azimuth[64]. Other similar study found a difference of 0.04 ppm[65].

5.10 ω_p and its systematic errors

The magnetic field B_{0i} for each data-taking run i is weighted by the number of analyzed positrons with start times $t > 30$ μs and energies $E > 2.0$ GeV in that run, N_i, to obtain the average field

$$\langle B\rangle = \frac{\sum_i B_{0i} N_i}{\sum_i N_i}. \tag{5.16}$$

The muon distribution is then taken into account. The final average magnetic field, $\langle\tilde{B}\rangle$, for the 1999 run is expressed as the free proton spin precession frequency and is determined to be

$$\langle\tilde{\omega}_p\rangle/2\pi = 61\ 791\ 256 \pm 25 \text{ Hz } (0.4 \text{ ppm}). \tag{5.17}$$

Table 5.1 lists the systematic errors for $\tilde{\omega}_p$.

Chapter 6

ω_a analysis

6.1 Introduction

The ω_a analysis started with the pulse reconstruction which determined the times and energies of positrons from raw WFD signals. The positron data selection was made based on some statistical criteria and infomation on operating conditions. After subtracting time spectrum of overlaping pulses and eliminating the fast rotation structure. we fit the time spectrum of positrons with energies greater than 2.0 GeV to a function including Eq. 3.8. muon loss. and coherent betatron oscillations. The effects on ω_a from radial electric field and pitch corrections were added to the result from the fitting to obtain the $g-2$ frequency ω_a.

6.2 Pulse reconstruction

The 1999 raw data of the decay e^+ were processed by two groups to find the positron pulses and reconstruct the energies and times of the pulses. The pulse reconstruction algorithms of both groups are based on the same principles. One group wrote the codes in FORTRAN and used PAW. Their production was called G2off[66. 67]. The other wrote the codes in C++ and used ROOT. Their production was called G2Too.

Examples of the pulses in the raw data are shown in Fig. 6.1. in which the left plot shows a single positron pulse and the right plot shows two pulses about 20 ns seconds apart. The typical FWHM of the positron signals is 5 ns. To reconstruct positron pulses from WFD data, both productions firstly obtained the average pulse shape for each individual detector. In G2off the pulses from 1-3 GeV after normalizing the amplitudes are used to determine the average pulse shape. and only the pulses near 2 GeV are used in G2Too. Both used pulses more than 150 μs after injection to avoid problems at early times. such as the high pedestal and overlap of two or more pulses. Fig. 6.2 shows the average pulse shapes used in G2off. The 400 MHz WFD is composed of a pair of 200 MHz WFDs operating 180° out of phase on the same analog pulse

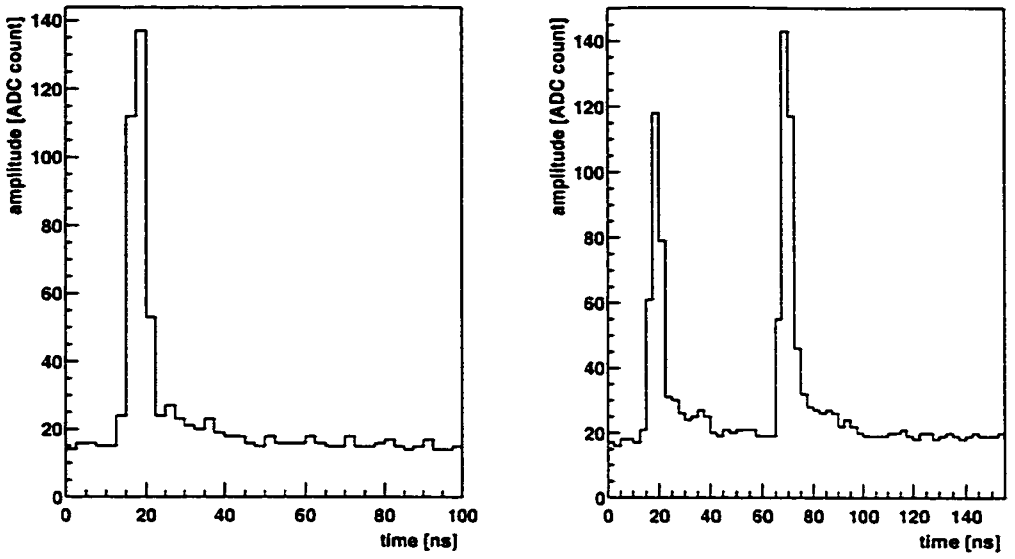

Figure 6.1: Two examples of raw WFD data are shown. The left figure shows a single positron pulse and the right figure shows two pulses close together.

as mentioned in Sec. 3.9. The pulse shapes are different for the two WFD phases. After obtaining the average pulse shapes, the WFD signals were fitted to the sum of a constant pedestal and the pulse shape, taking into account the difference of the shapes for two WFD phases. Both G2off and G2Too assign a constant error to the amplitude of each WFD bin and apply least square fitting to the WFD signals. Fig. 6.3 shows the fitting of the WFD signals. If the fitting failed some criteria on χ^2, both productions refit the WFD signal with the assumption that there were two or more pulses. If the pulses are closer than the resolution time, 2.9 ns for G2off and 5 ns for G2Too, the productions identify them as a single pulse. These overlaping pulses are called pileup pulses.

Simulations were used to examine both productions, especially for the determination of the energies and times of the pulses. For the G2off production, a pulse with energy lower than 250 MeV can not be reconstructed, which means an effective energy threshold in the production. The pulse energy, calculated from the amplitude of the pulse in G2off, agrees with the input energy to within 3 MeV, and it does not vary with the pulse amplitude. The time of the pulse, calculated from the fit time of the peak in G2off, differs from the input time by 20-100 ps depending on the amplitude. However this difference does not depend on the time and, therefore, does not affect the $g-2$ frequency measurement.

G2Too uses the integrated area of the pulse as the energy and the ADC count weighted time as the time of the pulse. Extensive studies, using sim-

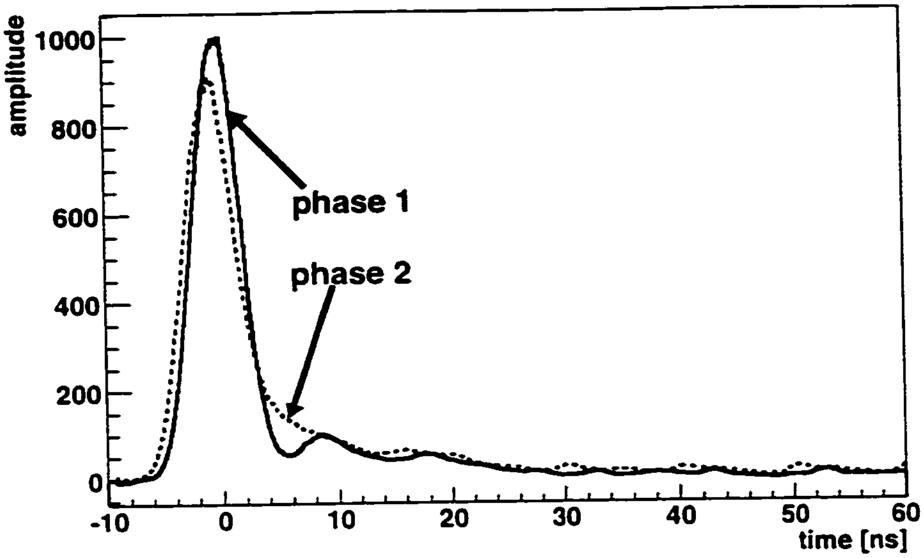

Figure 6.2: The average pulse shapes from G2off. The amplitudes shown in the figure are in an arbitary units. The pulse shapes are different for the two WFD phases.

ulations, were also done to test the G2Too approach. No effect which could affect the $g-2$ measurements was found.

The productions provide the amplitude or the integrated area of the fitted pulse as the energy of a positron. An endpoint calibration was done to convert the ADC value into the energy in GeV. This calibration is based on the fact that the maximum energy that a decay positron can have is equal to the energy of the muon, namely 3.09 GeV in our experiment. Part of the energy spectrum of the decay spectrum was fitted with a linear function. The fitting range is from 1/2 to 1/6 of the maximum value as shown in Fig. 6.4. The line then was extrapolated to the point where the number of the decay positrons is zero. This point is calibrated as 3.09 GeV. The inaccuracy of the endpoint does not affect the ω_a measurement because it only affects the value of positron energies in units of GeV and does not introduce a time dependent effect. In G2Too, a single endpoint calibration for all runs is provided for each detector. In G2off, the data-taking runs are divided into several groups and an endpoint is provided for each group and each detector. Fig 6.5 shows the endpoint (in GeV) for one detector processed by G2off.

Detailed comparisons between the two productions were made. No systematic differences were found.

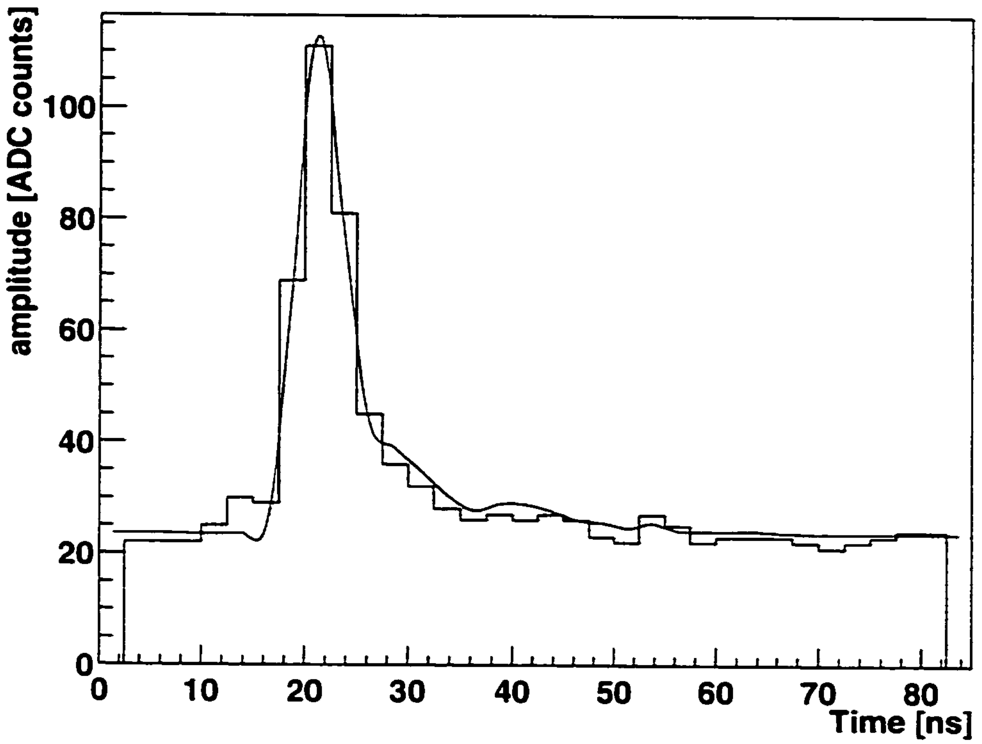

Figure 6.3: The fitting of the WFD signal for a positron.

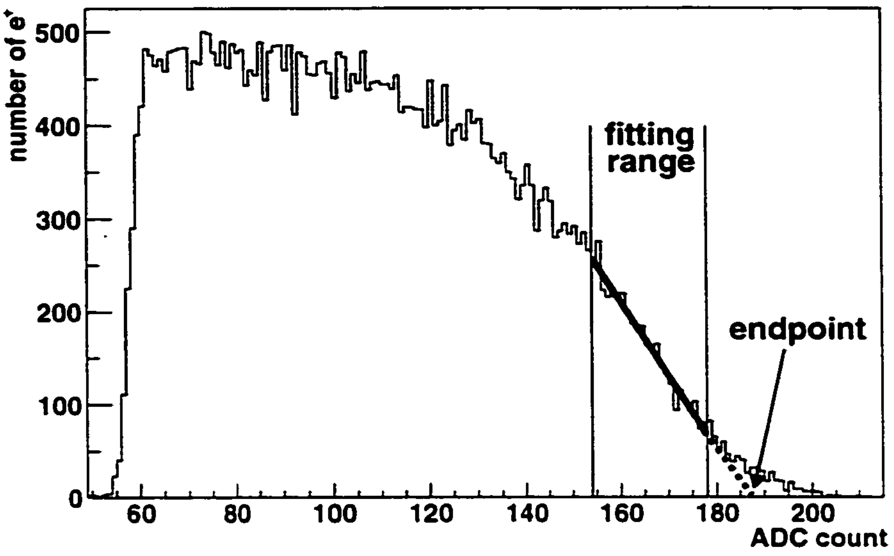

Figure 6.4: The linear fit to the energy spectrum in ADC count to find the endpoint. The fit range is from 1/2 to 1/6 of the maximum value in the energy spectrum.

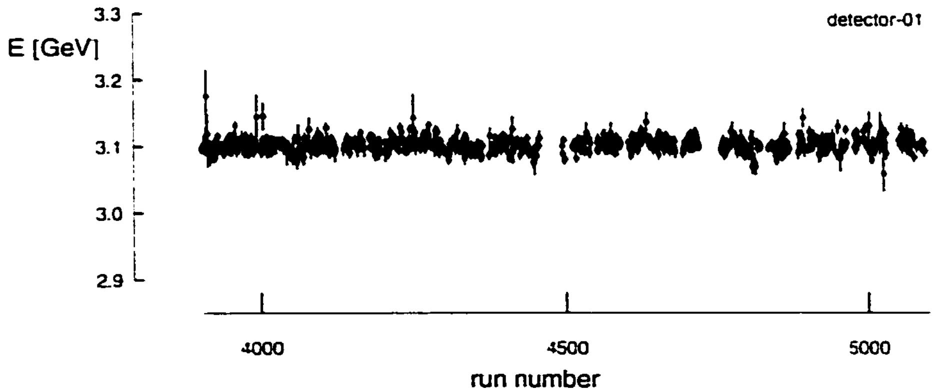

Figure 6.5: The end-point of the energy spectrum for one detector versus run.

6.3 Data selection

In the 1999 run, we took 1280 data-taking runs, each of which lasted from 0 to about 60 minutes. The data from detector 2 were not used in the ω_a analysis owing to a readout problem. The data from detector 20 were not used because the traceback chamber was installed in front of this detector, which had a significant effect on the data due to multiple scattering.

The data selection is performed initially at the level of data-taking runs. Many data-taking runs, especially the runs in January 1999, contained high level of AGS flashlet contamination. Simulations found that the flashlets was able to affect the measured values of ω_a by up to 1 ppm. The method mentioned in Sec. 4.3 was used. If one or more bins in t' spectrum (Fig. 4.4) have more positrons than the average by more than 3 times the statistical fluctuations, the data-taking run was excluded from further analysis.

After the above selections, events were randomly chosen from a set of 10 carefully examined runs scattered over the 1999 data taking period to form a reference. The other runs were individually compared to the reference using Kolmogorov-Smirnov test to determine the probability that the run was essentially the same as the reference run within the statistical fluctuations. In a two-dimensional, time and energy, distribution of the positrons, each positron is characterized by it energy and time $(E_i,\ t_i)$. The other positrons can be divided into four group, $(E < E_i,\ t < t_i)$, $(E > E_i,\ t < t_i)$, $(E < E_i,\ t > t_i)$, $(E > E_i,\ t > t_i)$. The relative populations of these four groups, f_i, with respect to the point $(E_i,\ t_i)$, were calculated for all positrons of this run and for those of the reference data , which we denote by g_i. The maximum difference, $|f_i - g_i|$, ranging both over the positron in the run and over the four groups, gives the probability that the two distributions are statistically the same. The probabilities, $P_{r,d}$, are calculated with respect to the reference data for run r and detector d. The average probability for run r is calculated as

$$P_r = \frac{\sum_d P_{r,d}}{22}. \tag{6.1}$$

where d is summed over all 22 detectors used in the analysis. The number of detectors which have $P_{r,d} < 0.05$ is counted and divided by 22 to obtain the fraction of low probability detectors for each run. Fig. 6.6 shows the average probability and the fraction of low probability detectors. Runs with an average probability lower than 0.25 and runs with more than 3 detectors which have a probability lower than 0.05 were excluded from the analysis for ω_a. Differences at the level of 1% in the integral distribution of positrons , which by construction is insensitive to frequency changes, are caught in this method. The log books were carefully studied to cross-check the Kolmogorov-Smirnov test. All the runs which were marked as runs not suitable for ω_a analysis because of a distorted positron spectrum were found by the Kolmogorov-Smirnov test.

After the run selection, further data selection was done on the AGS fills. Two criteria for the fill selection are the T0 signal and the quality of the

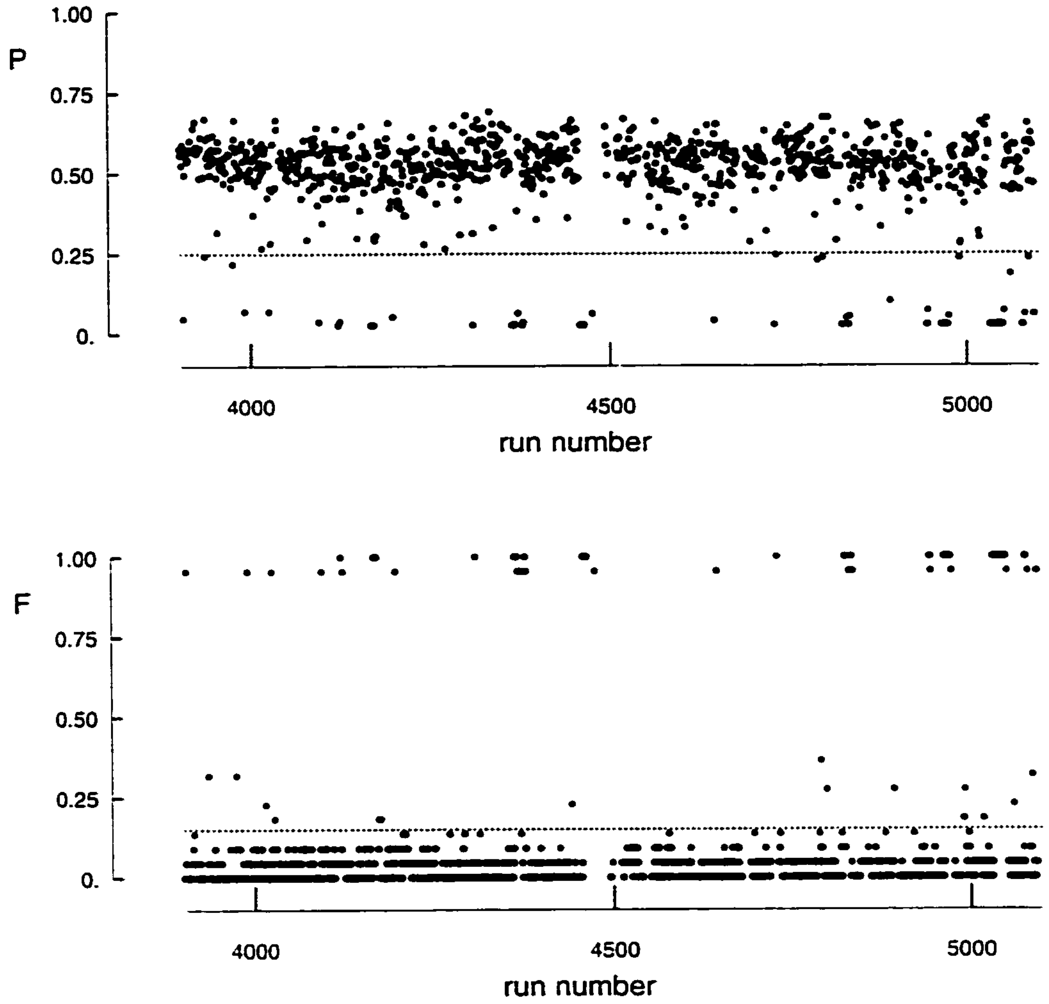

Figure 6.6: The top plot shows the average probability for all 22 detectors used in the analysis vs. run number. A cut at 0.25 was made to exclude the low probability runs. The bottom plot shows the fraction of low probability detectors vs. run number. A cut of 3/22 was made to exclude low probability runs.

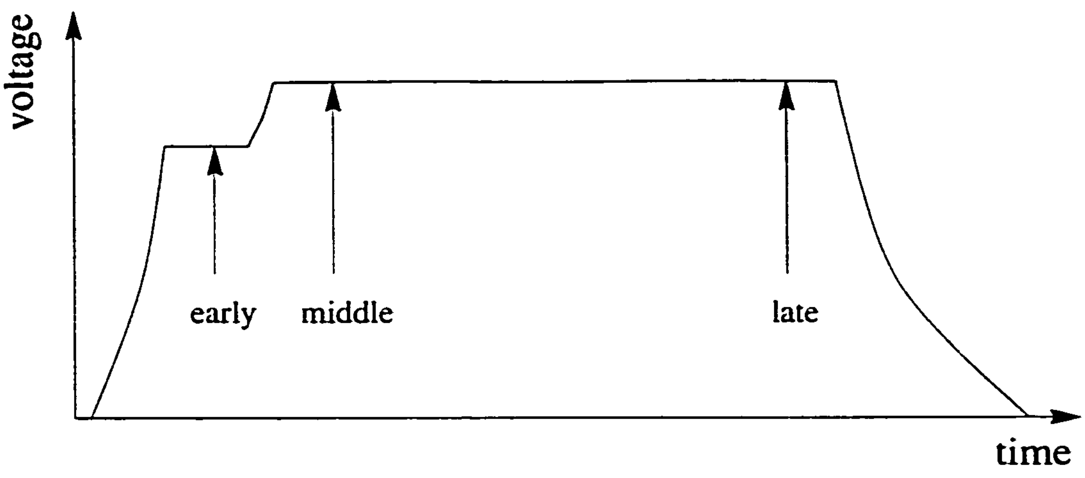

Figure 6.7: Schematic plot of a quadrupole pulse.

electrostatic quadrupole fields.

When the AGS misfired its kickers, only a small portion of the proton bunch was sent to our target. The leftover protons produced flashlets afterwards (see Sec. 4.3). In most of these cases, the number of protons sent to our target was so few that the amplitude of the signal in the T0 counter was below threshold. Hence, the T0 counter recorded no signal. Studies on highly contaminated runs, which had already been excluded from the analysis, showed that the AGS cycles (including 6 bunches) contained most AGS flashlets if one of the bunches was not properly extracted and no signal on T0 counter was observed. In the analysis, we exclude all the AGS cycles with one or more fills having no signal on the T0 counter[68]. They account for 5.4% of the data in the selected data-taking runs.

The electrostatic quadrupoles, used for focusing, occasionly sparked and discharged before the set discharge time. The stored muons were instantly lost on such occasions. This significantly changed the beam dynamics and affected the measurements of muon lifetime and ω_a. The quadrupole voltage pulse shape was digitized by WFD and a schematic plot of a WFD trace is shown in Fig. 6.7. The fills with early discharges of the quadrupoles were excluded by requiring that the voltages at the middle and late times were equal to within 5% for fills kept in the analysis. To reduce uncontrolled muon losses, a 7 kV scraping voltage was applied for the first 20 μs after beam injection(Sec. 3.7). The fills with failed scraping were excluded by requiring that the voltages at early and middle times differed by 7 kV to within 5%. The number of fills excluded owing to this selection amounts to 0.3%.

6.4 Pileup subtraction

Because of the high rate of the decay positrons and the finite pulse resolution time of the WFD and the pulse reconstruction algorithm, about 1% of the

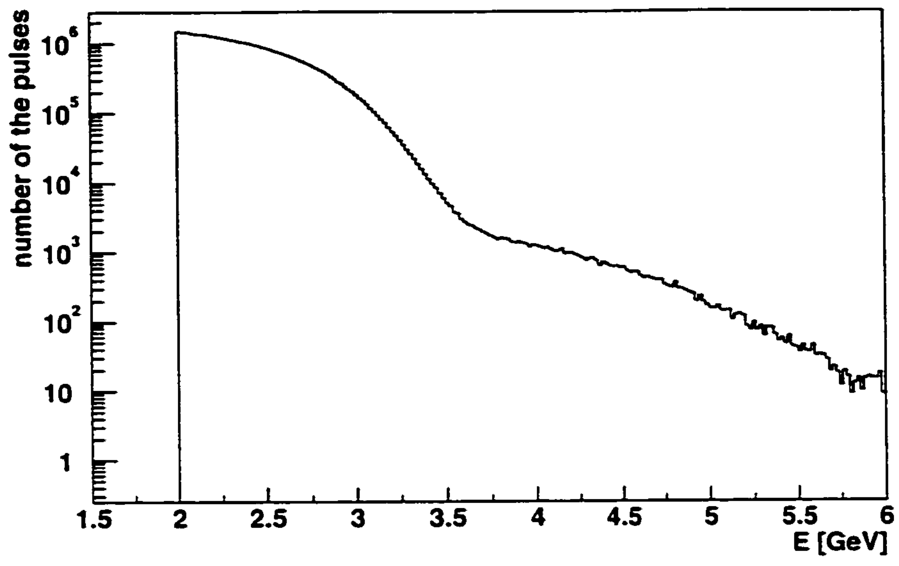

Figure 6.8: The energy spectrum of the e^+ pulses.

positron pulses overlap when the fits of ω_a to the data are started. Fig. 6.8 shows the energy spectrum of the pulses. The pulses with energy greater than 3.09 GeV, the energy of the stored muon beam, are mostly pileup pulses, but some are due to the detection energy resolution. The number of pileup pulses in the reconstructed data is proportional to the instantaneous counting rate squared $(dN/dt)^2$ and to the minimum pulse resolution time of the reconstruction algorithm t_R, which is 2.9 ns for G2off and 5 ns for G2Too. The pileup amounts to 1% of the data at 32 μs when the fits of ω_a to the data are started and the number of the pileup pulses decays with a lifetime of 32.2 μs, half of the dilated life time of the muons in our storage ring. Pileup distorts the e^+ time spectrum because of misidentification of the number, energies, and times of the positrons. Since the phase of the $g-2$ oscillation, $\phi_a(E)$ in Eq. 3.8, depends on the energies of the positrons, pileup has a phase which differs from ϕ_a. Because the lifetime of the pileup pulses is different from the dilated lifetime of the muons in our storage ring, an early to late phase shift resulted from the pileup pulses leads to an error in ω_a. Therefore, the data are corrected prior to fitting by subtracting a constructed pileup spectrum[69, 70]. The construction of the pileup spectrum makes use of a character of our WFD records. In the WFD records, if the energy of a positron exceeds the energy threshold and triggers the WFD, the WFD will record for about 50-80 ns. The triggering pulse is labelled $S1$. If another positron arrives after the trigger pulse within the 50-80 ns, it will be recorded regardless of its energy. This pulse is labelled $S2$. This character allows us to observe the positron pulses with energies lower than the 1 GeV hardware threshold (see Sec. 3.9). To construct the pileup

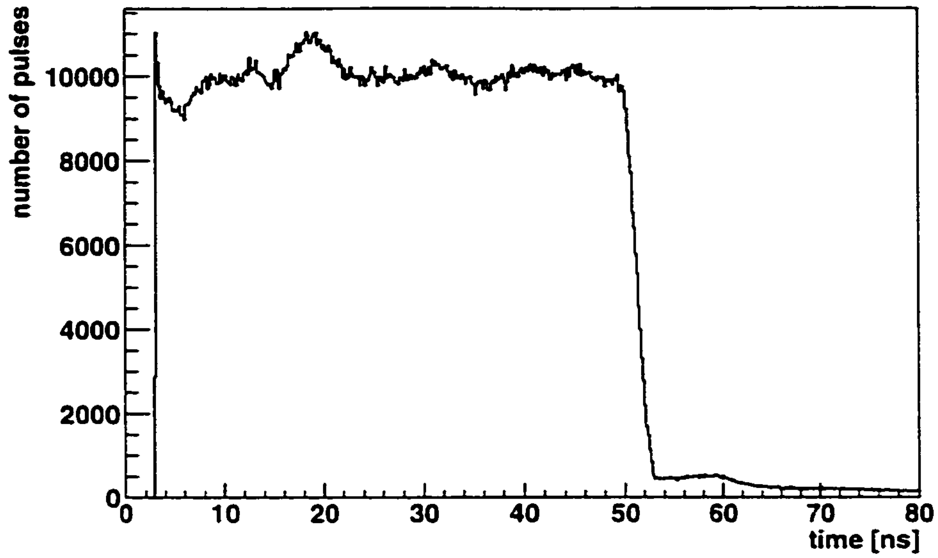

Figure 6.9: Spectrum of $t_{S2} - t_{S1}$. The drop at about 52 ns is because the WFD records were ended at that time.

spectrum, we made the assumption that the instantaneous positron rate varies significantly only on time scales larger than 40 ns. The muon lifetime of 64.4 μs and the $g-2$ oscillation period of 4.365 μs make this assumption an approximation. Some features of the pulse reconstruction algorithm will also affect the validity of this assumption. Fig. 6.9 shows the instantaneous positron rate is constant to within 10% within 40 ns. The probability of two pulses overlapping is thus nearly identical to the occurance of two pulses seperated by a fixed time $T < 40$ ns. Hence, we can construct the pileup pulse by treating $S1$ and $S2$ as if they overlap as shown in Fig. 6.10. The time and energy of the pulse $S1$ are labelled as t_{S1} and E_{S1}, and as t_{S2} and E_{S2} for the pulse $S2$ in the time period from $t_{S1} + T - t_R$ to $t_{S1} + T + t_R$, where T is a fixed time delay and t_R is the resolution time of the pulse reconstruction algorithm. The constructed pulse is labelled as D with time t_D and energy E_D. To determine the time and energy of the pileup pulse D, we create pileup pulses in a simulation in which we know the times and energies of the pulses which overlap to form the pileup pulses. We fit the pileup pulses with the pulse finding algorithm to get the reconstructed times and energies of the pileup pulses. It was found that the time and energy of the D are best approximated by

$$t_D = \frac{t_{S1}E_{S1} + (t_{S2} - T)E_{S2}}{E_{S1} + E_{S2}} \qquad (6.2)$$

$$E_D = f_{\mathrm{pu}}(E_{S1} + E_{S2}) \qquad (6.3)$$

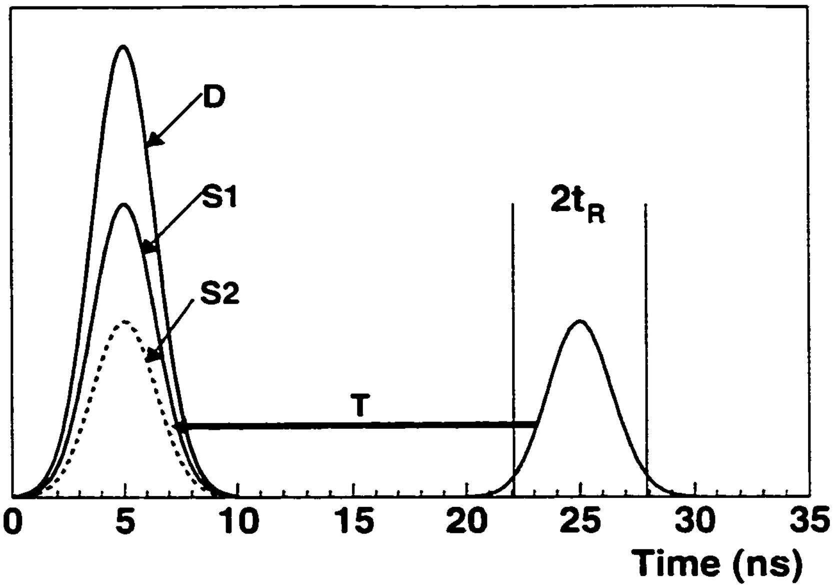

Figure 6.10: The shadow pulse $S2$ which is between $T - t_R$ ns and $T + t_R$ ns is moved earlier by T to construct the pileup pulse with the trigger pulse $S1$, where t_R is the pulse resolution time. The constructed pulse is labelled D.

where $f_{\text{pu}} = 0.96$ for G2off and $f_{\text{pu}} = 0.94$ for G2Too. No significant energy and separation time dependences in f were found in the studies. If the pulse $S2$ has an energy less than the 1 GeV hardware threshold, one more pileup pulse is constructed and the time and energy is assigned to be

$$t_D = \frac{t_{S1}E_{S2} + (t_{S2} - T)E_{S1}}{E_{S1} + E_{S2}} \tag{6.4}$$

$$E_D = f_{\text{pu}}(E_{S1} + E_{S2}) \tag{6.5}$$

The reason is that the equivalent situation, in which the pulse $S1$ has an energy less than 1 GeV, was not recorded due to the hardware threshold. Since we cannot construct pileup pulses from two pulses with both energies lower than the hardware threshold, only data with energies at least twice the hardware threshold are fully corrected by this method. Our 1 GeV hardware threshold leads to a choice of $E > 2$ GeV for the positrons used in the ω_a analysis. The spectrum $(D - S1 - S2)/2$ is subtracted from the original spectrum since pileup pulses are created when two single pulses are lost. The factor 2 is the normalization of the contruction algorithm. Fig. 6.11 shows the energy spectrum of $D, S1$, and $S2$ together with the energy spectrum before and after pileup subtraction. The contribution to pileup from signals too small to be reconstructed by the pulse reconstruction algorithm is not accounted for by the procedure described above. These small signals increase the reconstructed energies when they overlap with positron pulses. However, the small signals

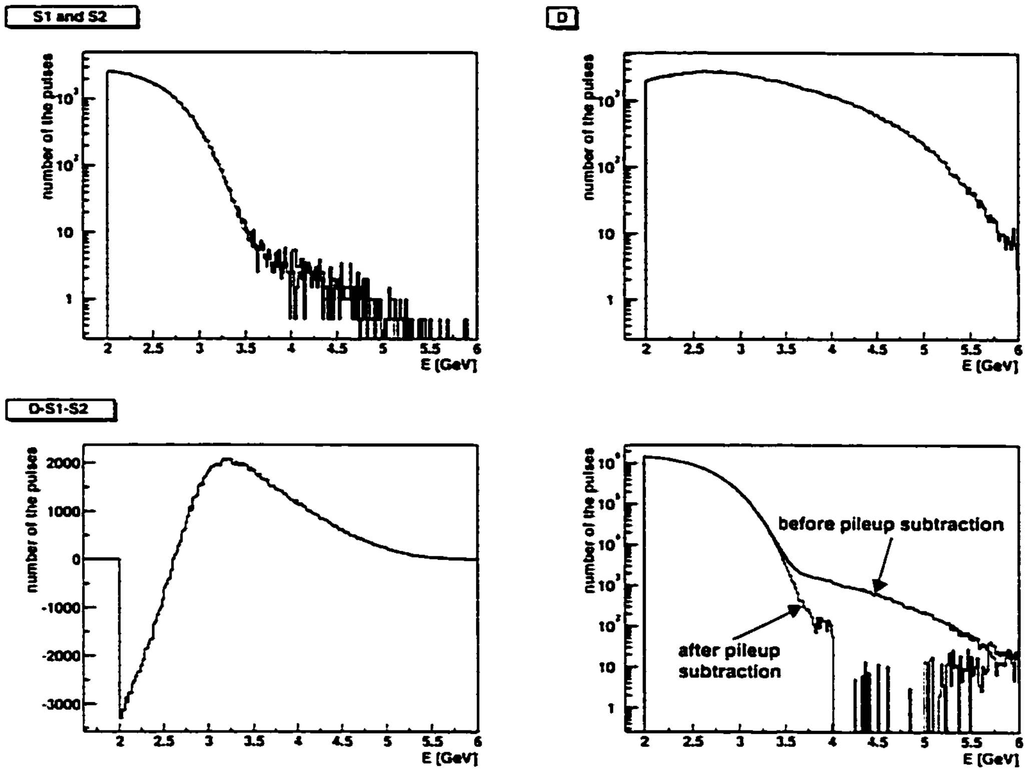

Figure 6.11: The energy spectrum of the D, S1, S2 and D-S1-S2. The spectra of S1 and S2 differ only by statistical fluctuation.

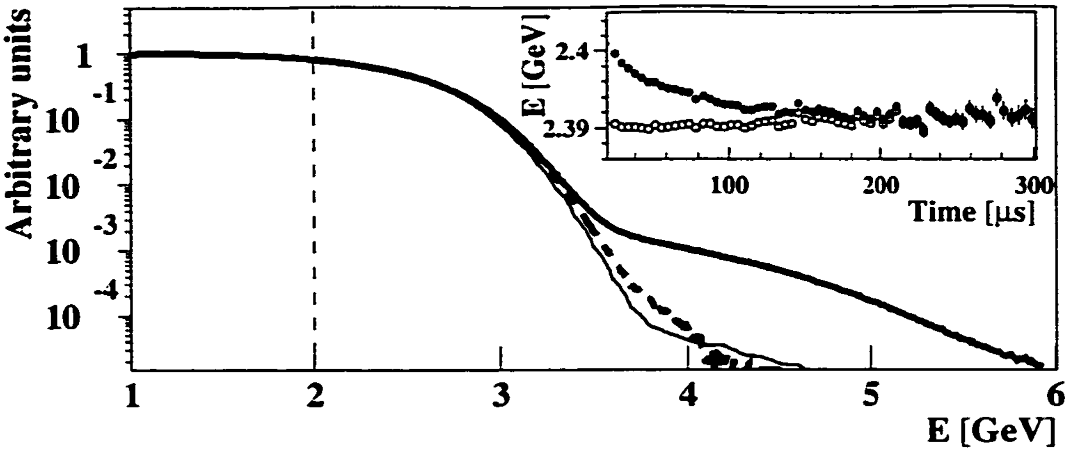

Figure 6.12: The energy spectrum of the detected positrons above 1 GeV at all times (thick line) and at late times (thin line) together with the pileup subtracted spectrum at all times (dashed line). The inset shows the energy above 2 GeV averaged over $g-2$ period as a function of time before (filled circles) and after (open circles) pileup subtraction for a typical detector.

can also decrease the reconstructed energies when when they are away from the positron pulses and increase the pedestal in the pulse reconstruction. These small signals distort the pulse reconstruction but do not, on average, affect the energy. However, such unseen pulses introduce small time-dependent shifts in $A(E)$ and $\phi_a(E)$ because they cause the migration of the positrons with energies just below and above the energy threshold. The time dependence of the asymmetry, which is more sensitive than the phase, is used to set a limit on the shift on the phase which leads to an error on ω_a.

Fig. 6.12 shows the agreement between the positron energy spectrum after pileup subtraction and the spectrum at later times when pileup is negligible, together with the uncorrected spectrum. The inset illustrates that the average energy after pileup subtraction is constant with time, as expected.

6.5 Data randomization and studies of rate dependent effects

As mentioned in Sec. 5.9, the bunch structure of the beam shortly after beam injection (fast rotation) leads to a strong modulation of the decay positron time spectra as shown in Fig. 5.37. This modulation, with a period of 149.2 ns, remains at 32 μs when we begin our fits. In the analysis of the 1999 run, the fast rotation modulation is eliminated from the time spectra by randomizing the start time for each detector and each storage fill over the range of one fast rotation period of 149.2 ns. This process reduces the $g-2$ asymmetry. However, the reduction is small because the fast rotation frequency of 6.706 MHz is far

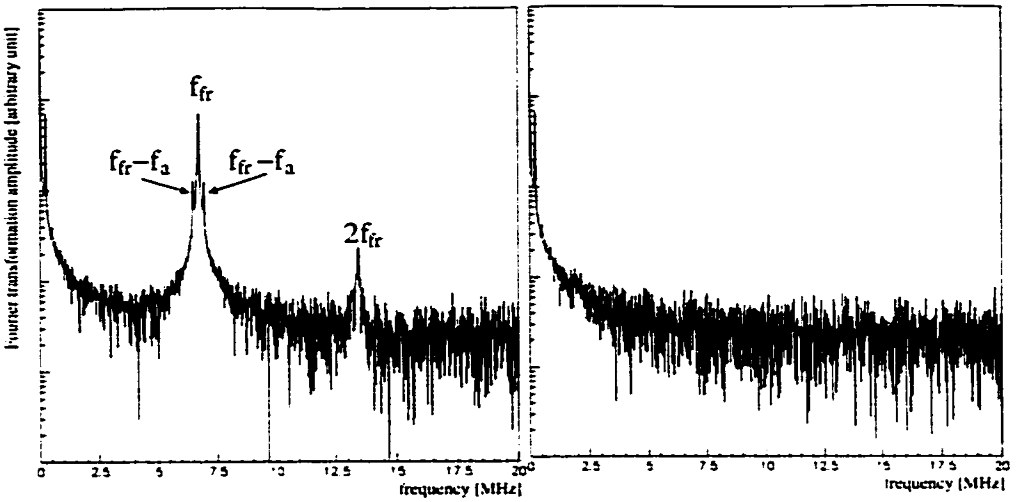

Figure 6.13: The left figure shows the Fourier transformation of the time spectrum of the decay positrons. The large peak at 6.706 MHz is the fast rotation frequency and the sidebands are the beat between the fast rotation and the $g-2$ oscillation. The second harmonic frequency of fast rotation is also seen. The right figure shows the Fourier transformation of the time spectrum of the decay positrons after the data randomization. The fast rotation peak is eliminated by the randomization.

higher than the $g-2$ frequency of 0.2291 MHz. The choice of the interval used in the randomization was studied. No systematic difference in the measured ω_a was found when randomization intervals of 149.12 ns and 148.96 ns were used. Fig 6.13 shows the Fourier transformation of the time spectrum of the decay positrons before and after the randomization.

The strong modulation of the decay positron time spectra can be useful for other studies. The very high positron rate at the peak of the fast rotation enhances the effects which depend on the decay positron rate. such as the dectector gains and pileup. The effects change the energy spectrum of detected positrons with the $g-2$ frequency. Therefore the time spectrum of the detected positrons with energy larger than some threshold becomes

$$N(t) = N_0 e^{-t/\tau}[1 + A\cos(\omega_a t + \phi_a) + \underline{N_g e^{-t/\tau_g}(1 + A_g\cos(\omega_a t + \phi_a + \phi_g))}], \tag{6.6}$$

where the symbols with g are related to the effect. Fitting this spectrum with the function in Eq. 3.8 will give a wrong ω_a value. In the case of pileup $n_g = 5 \times 10^{-3}$. $\tau_g = 64\ \mu s$. $A_g = 0.06$, and $\phi_g = 70$ mrad and the result on ω_a from the fitting will differ from the true value by 0.3 ppm. The study of the average energy shortly after the beam injection gives us a measurement of the rate-dependent effects (underlined in Eq. 6.6) when the decay positron rate is high. The rapid change of rate enables us to decouple effects which depend on the rate from other effects which change slowly with time.

Fig. 5.37 shows the fast rotation structure in the decay positron time spec-

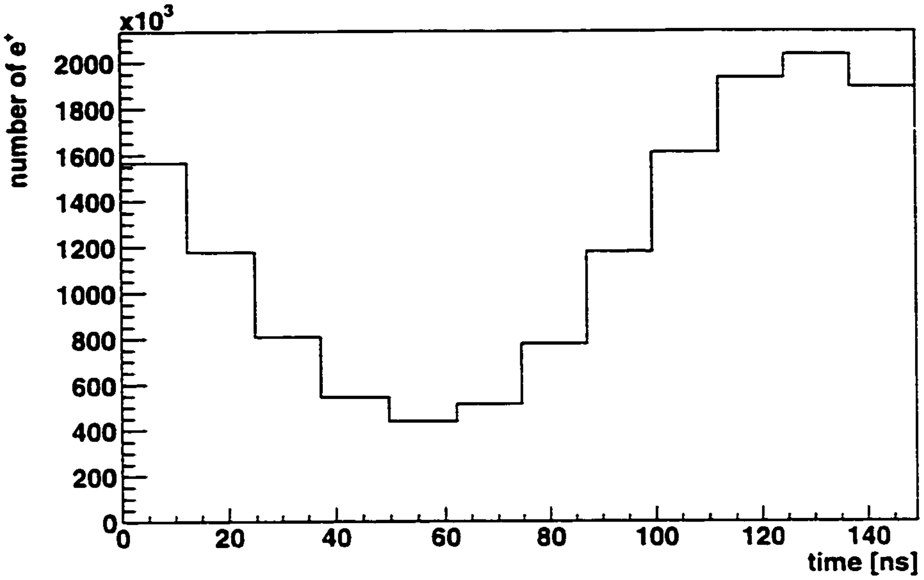

Figure 6.14: The decay positron time spectrum with 234 fast rotation periods folded into one.

trum for one detector shortly after the beam injection. Two hundred and thirty-four fast rotation periods are folded onto one period to increase statistics. This folded time spectrum is shown in Fig. 6.14. We choose 234 fast rotation periods because this time interval is nearly 8 times the $g-2$ period. This choice minimizes the energy spectrum change due to the $g-2$ oscillation. Since one bin in Fig. 6.14 contains positrons from 234 fast rotation periods, the average time of the positrons in each bin has to be calculated and the largest time difference between bins is about 7 μs instead of 149.2 ns. The average times are shown in Fig. 6.15. In the folded time spectrum, the positron rate changes by a factor of 4.5 within about 7μs. Fig 6.16 shows the average energy of the positrons for each bin in Fig. 6.14. Combining the data in Fig. 6.16 and in Fig. 6.14, we get the average energy versus the positron rate as shown in Fig. 6.17. In the bunched muon beams, there is about 0.6% momentum spread. The higher momentum muon have a larger orbital radii and lag the lower momentum muons in the fast rotation. The positrons decayed from higher momentum muons get more energy from the boost and have higher average energy. This effect leads to the vertical bifurcation of the curve, apart by about 0.6% of the average energy as shown in Fig. 6.17. The slope from the linear fit to the data points in Fig. 6.17 is proportional to the amplitude of the effects which depend on the decay positron rate. The data without pileup subtraction are shown for comparison. As mention above, the shift in ω_a due to the rate dependent effect from pileup is 0.3 ppm. Therefore, after the pileup subtraction, the shift in ω_a due to the rate dependent effects

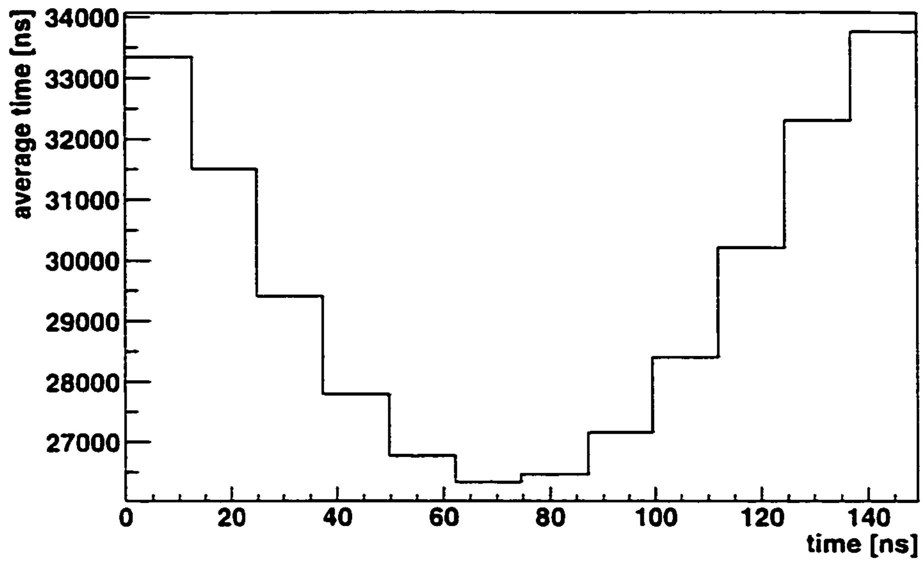

Figure 6.15: The average time the the positrons in the folded time spectrum of Fig. 6.14. The largest time difference between bins is about 7 μs instead of 149.2 ns.

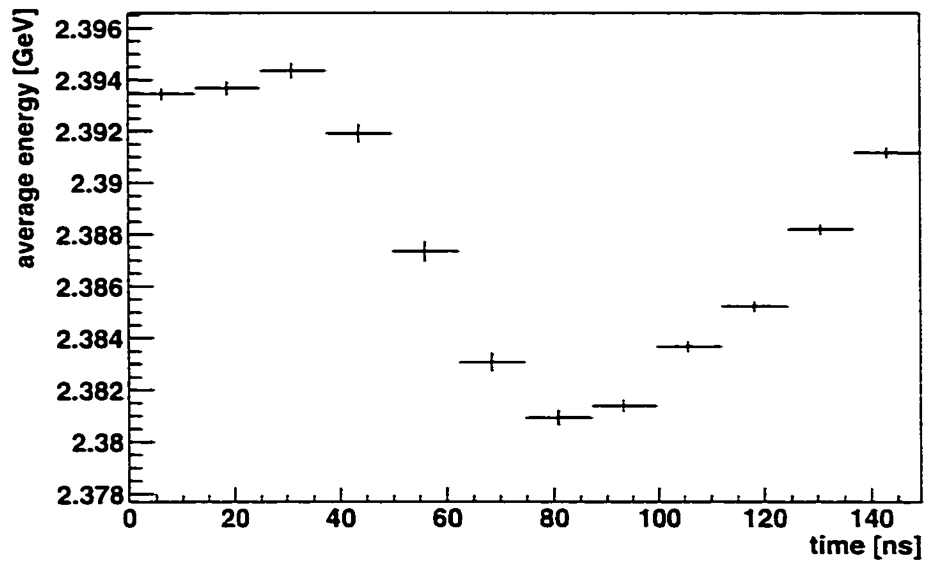

Figure 6.16: The average energy of the positrons vs. the time in each bin in Fig. 6.14.

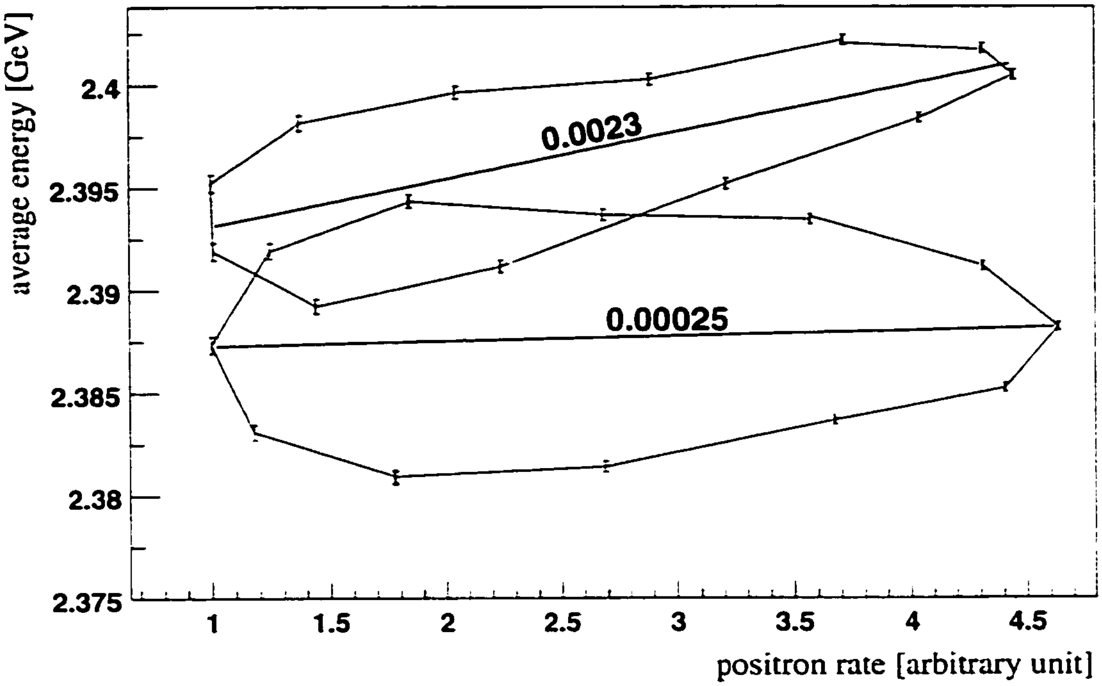

Figure 6.17: The average energy vs. the decay positron rate. The lower bifurcation shows the result from the data in Fig. 6.16 and in Fig. 6.14, in which the pileup has been subtracted using the method mentioned above. The upper bifurcation shows the result from the data without pileup subtraction. The lines show linear fit to the data and the slopes are shown.

is less than 0.05 ppm which agrees with other studies of possible instrumental sources for the rate dependent effects[71].

6.6 Fitting of the data

The high counting rate and large data sample for 1999 make the 5-parameter function Eq. 3.8 inadequate for fitting the data and require careful consideration of (1) coherent betatron oscillations, (2) muon loss, and (3) detector gain stability during the muon storage time.

1. The storage ring is a weak focusing spectrometer(field focusing index $n = 0.137$) with a circular aperture 9 cm in diameter. It is large compared to the 18(width) x 57(height) mm^2 inflector aperture shown in Fig. 3.5. Therefore, the phase space for betatron oscillations which is defined by the acceptance of the storage ring is not filled by injected muons. In combination with imperfect horizontal kick, this results in betatron oscillations of the beam as a whole – coherent betatron oscillations(CBO). These oscillations are observed directly with the fiber monitors (Sec. 3.10) plunged into the storage region at 180° and 270° downstream from the injection point in azimuth. The measurement at 180° is shown in Fig. 6.18. From this measurement and from simulation, it is found that the amplitude of the CBO is about 1 mm in the vertical and about 1 cm in radial directions. The frequency of horizontal CBO is $f_b = f_c(1 - \sqrt{1-n}) \approx 470$ kHz, where $f_c = 6.706$ MHz is the cyclotron frequency. The CBO amplitude decays owing to both the momentum spread of the muons and the spread of field focusing index n seen by muons. The CBO modulate the positron time spectra since the acceptances of the calorimeters vary with the radial position of the muon decay. Fig. 6.19 shows this modulation in the Fourier transformation of the residuals after the fit to the positron time spectrum with Eq.3.8 which takes into account the muon decay and the $g-2$ precession. The CBO effect changes $N_0(E)$, $A(E)$ and $\phi_a(E)$ in Eq. 3.8

$$\begin{aligned} N_0(E,t) &= b(t)N_0(E) = [1 + A_{bN}e^{-t^2/\tau_b^2}\cos(\omega_b t + \phi_{bN})]N_0(E), \\ A(E,t) &= X(t)A(E) = [1 + A_{bA}(t)\cos(\omega_b t + \phi_{bA})]A(E), \\ \phi(E,t) &= Y(t)\phi(E) = [1 + A_{b\phi}(t)\cos(\omega_b t + \phi_{b\phi})]\phi(E), \end{aligned} \tag{6.7}$$

where the angular frequency $\omega_b = f_{cbo}/2\pi$. The phase ϕ_{bN}, ϕ_{bA}, and $\phi_{b\phi}$ varies for the different detectors

$$\phi_{bN,\ bA,\ b\phi} = \phi^0_{bN,\ bA,\ b\phi} + z, \tag{6.8}$$

where $\phi^0_{bN,bA,b\phi}$ are different constants for ϕ_{bN}, ϕ_{bA}, and $\phi_{b\phi}$ respectively and z is the azimuthal location of the detector. Hence, the CBO effect is cancelled by summing the data from all detectors. This cancellation

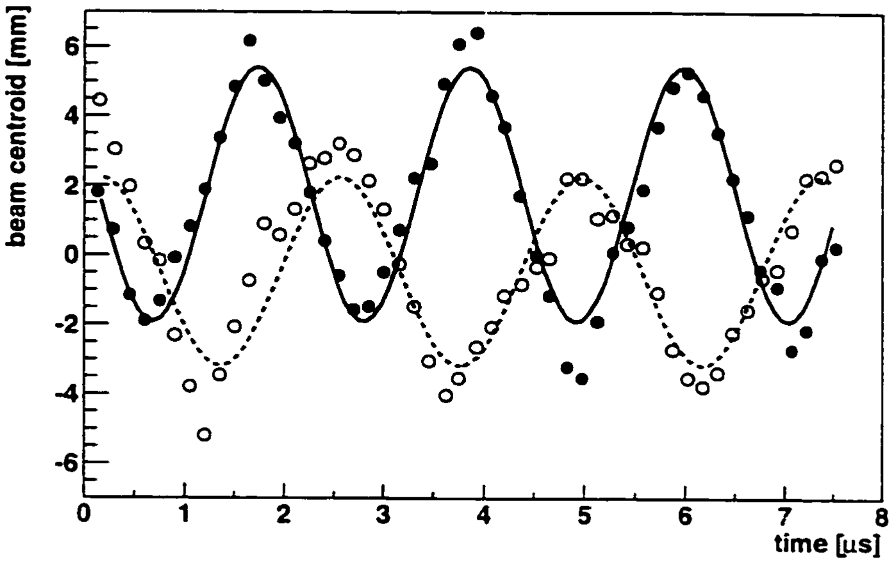

Figure 6.18: The radial beam position versus time measured by the fiber monitor at 180° downstream from the injection point. The two curves show the horizontal movement of the beam centroid during the 7 kV scraping period (open circles) and at later time without scraping (filled dots).

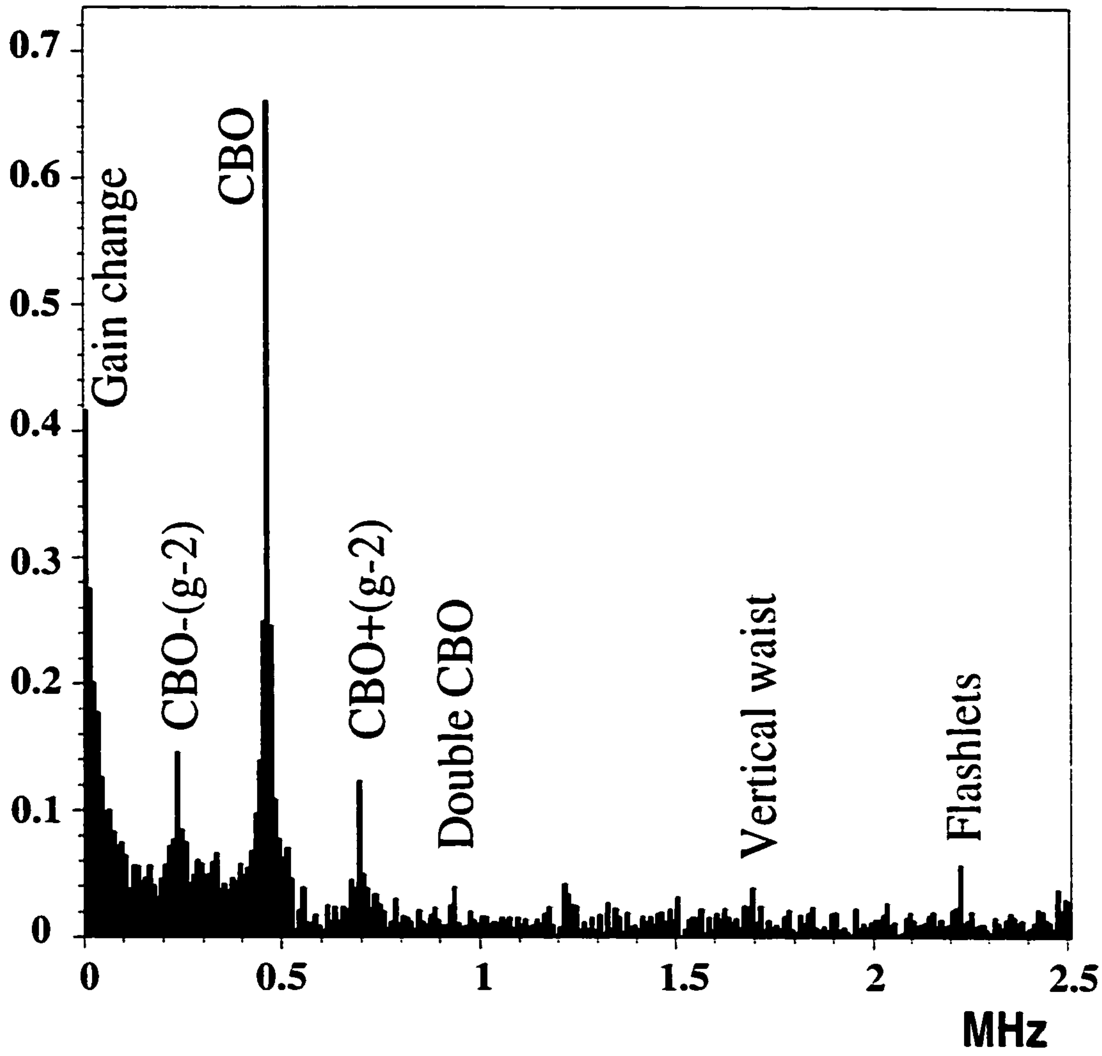

Figure 6.19: Fourier transformation of the residuals after the fit to the positron time spectrum with Eq. 3.8.

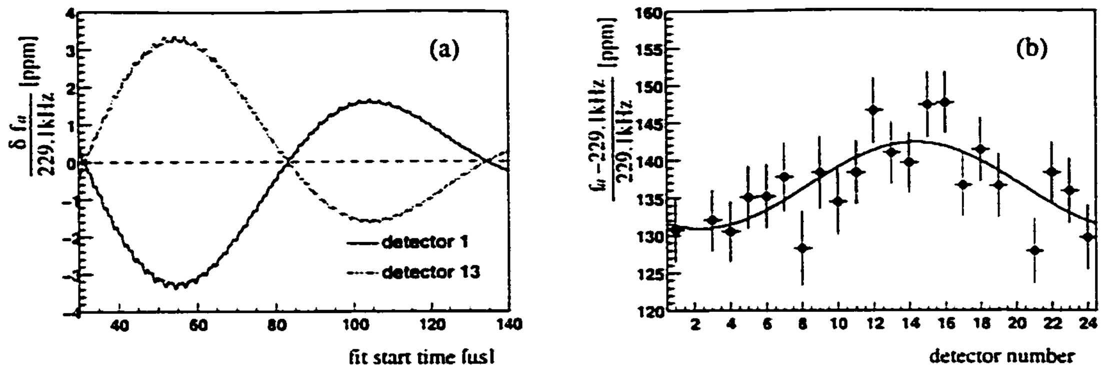

Figure 6.20: (a) Offset of $f_a = \omega_a/2\pi$ versus fit start time for detector 1 and 13 due to neglecting $A_{bA}(t)$ and $A_{b\phi}$ in a simulation. Detectors 1 and 13 are at opposite sides of the ring. (b) f_a versus detector at the fit start time of 60 μs after the injection. The fit to a sine curve is shown.

is incomplete because the data from dectector 2 and 20 are not used and because the different acceptances of detectors. In the fitting function, we set $A_{bA}(t) = 0$ and $A_{b\phi}(t) = 0$, but the function $b(t)$ in $N_0(E, t)$ is included. The angular frequency ω_b is determined from the Fourier spectrum shown in Fig 6.19. The asymmetry A_b, the time constant τ_b, and the phase ϕ_b are determined from the fit to the data. A_b is found to be about 0.01 and τ_b is found to about 120 μs, and ϕ_b varies by detectors roughly from 0 to 2π as expected. The neglect of $A_{bA}(t)$ and $A_{b\phi}$ leads to an offset in the results for ω_a for individual detectors. The amplitude of the offset for one detector at one fit start time depends on the phase differences $\omega_b t + \phi_{bA} - \omega_a t - \phi_a$ and $\omega_b t + \phi_{b\phi} - \omega_a t - \phi_a$. In 1999, this effect is not significant compared to the large statistical errors for each detector. The data from 2000 run is used to study this effect. The results of ω_a for each detector at the fit start time of 60 μs after injection in the 2000 run is shown in Fig 6.20 together with the offset versus fit start time from simulation for two detector on opposite sides of the ring. Careful study shows that the systematic effect due to CBO on measured ω_a is reduced to 0.2 ppm by fitting to the summed spectra of all 22 detectors with a function including $b(t)$[14, 74].

2. Losses of muons during the data collection are minimized by controlled scraping before the data collection(Sec. 3.7). The muons at the edge of the beam were scraped by the colimators and were lost during the scraping period instead of being lost later during the data collection. However, there is still some muon loss during the data collection as shown in Fig. 6.21. An adequate parametrization of the muon loss is found to be

$$l(t) = 1 + n_l e^{-t/\tau_l}. \tag{6.9}$$

The decay time and the amplitude of the muon loss are found to be

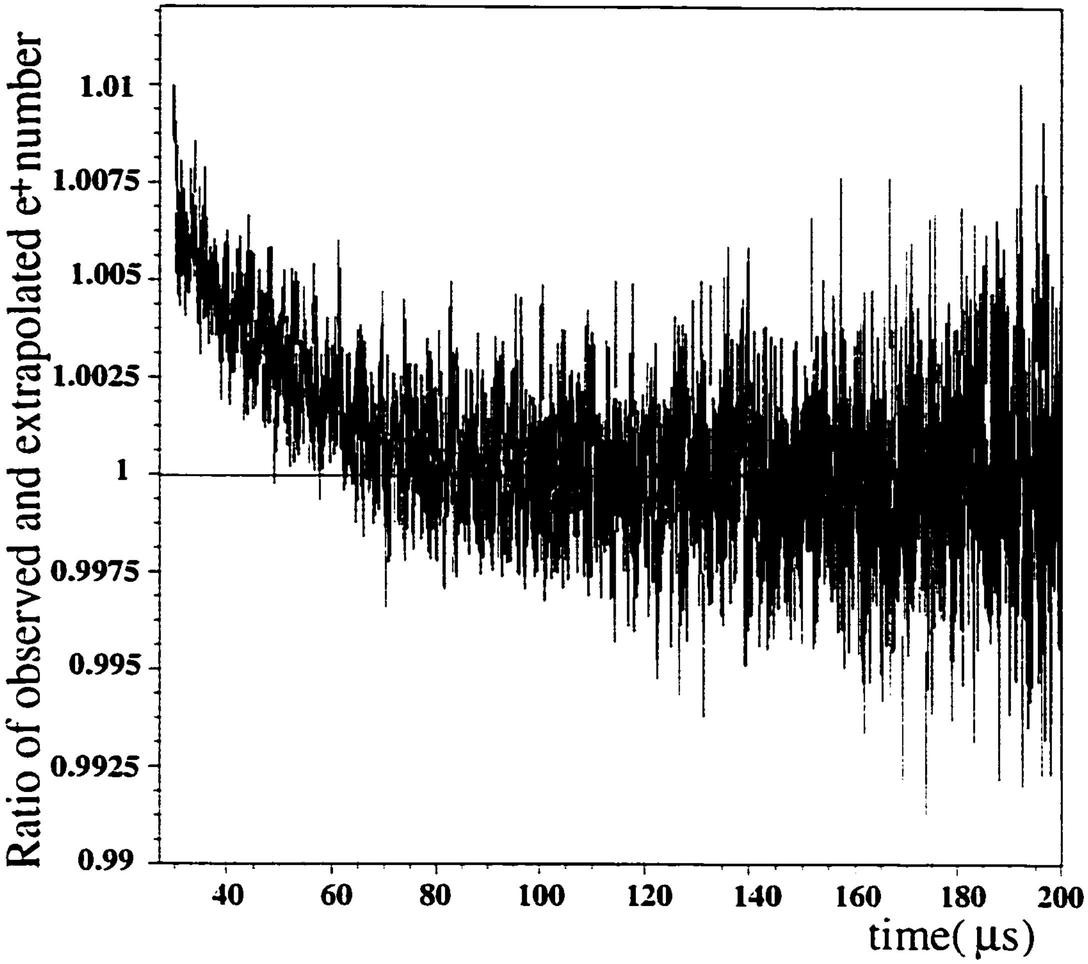

Figure 6.21: The ratio of the observed and extrapolated numbers of positrons vs. time. The positron time spectrum after 150 μs is extrapolated to early times with the function of Eq. 3.8. The excess of the observed positrons, compare to the extrapolated number of positrons, shows the munber of the lost muons at early times.

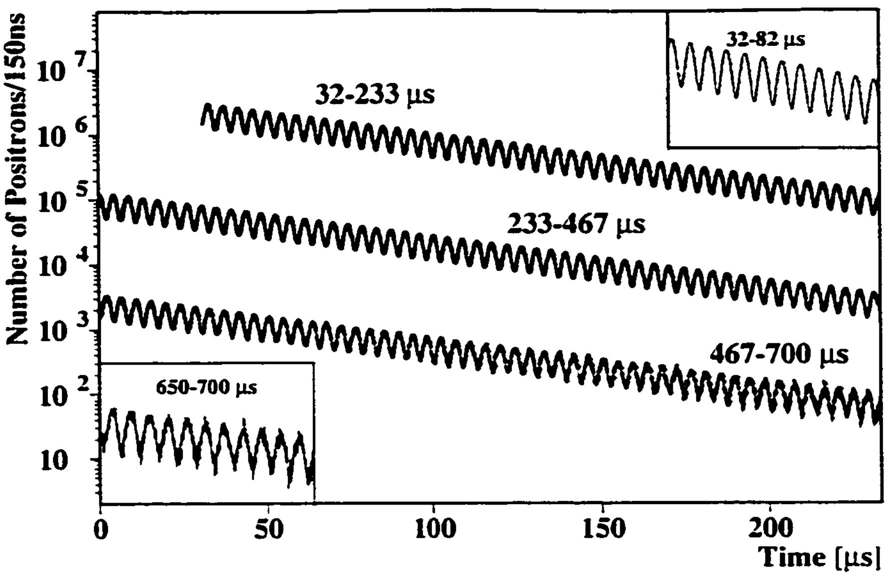

Figure 6.22: Positron time spectrum overlaid with the fit with Eq. 6.10 ($\chi^2/d.o.f = 3818/3799$). The total event sample of 0.95×10^9 e^+ with $E \geq 2.0$ GeV is shown.

$\tau_l = 27$ μs and $n_l = 0.025$ by fitting the data.

3. Detector gain changes and time shifts are monitored with a pulsed laser system and determined in analysis by using the positron energy spectra. From 32 μs on. the gains of all the detectors except two detectors are stable to within 0.1% over 10 delated muon lifetimes. which leads to an error of less than 0.02 ppm in ω_a. The reconstructed times are stable to within 20 ps over 200 μs which gives an error of less than 0.1 ppm in ω_a.

After the fast rotation randomization and pileup subtraction. the time spectrum of positrons is then fitted by the function

$$f(t) = N(t)b(t)l(t). \tag{6.10}$$

Here. $N(t)$ is the muon decay and precession function of Eq.3.8. $b(t)$ is the coherent betatron oscillation function. and $l(t)$ is the muon loss term. The CBO frequency ω_b is determined from a Fourier analysis as mentioned above. The remaining 10 parameters in Eq.6.10 are adjusted to the data. in the sense of minimizing χ^2. The frequency ω_a correlates strongly only with ϕ_a. Consequently. ω_a is insensitive. unlike χ^2. to the values of the other 8 parameters and to the functional forms of $b(t)$ and $l(t)$. Fig. 6.22 demonstrates the good agreement of data and fit. as indicated by χ^2 =3818 for 3799 degrees of freedom(d.o.f.).

The internal consistency of the results was verified in several ways. As an example. Fig. 6.23a shows the results when the fit range starts at increasing

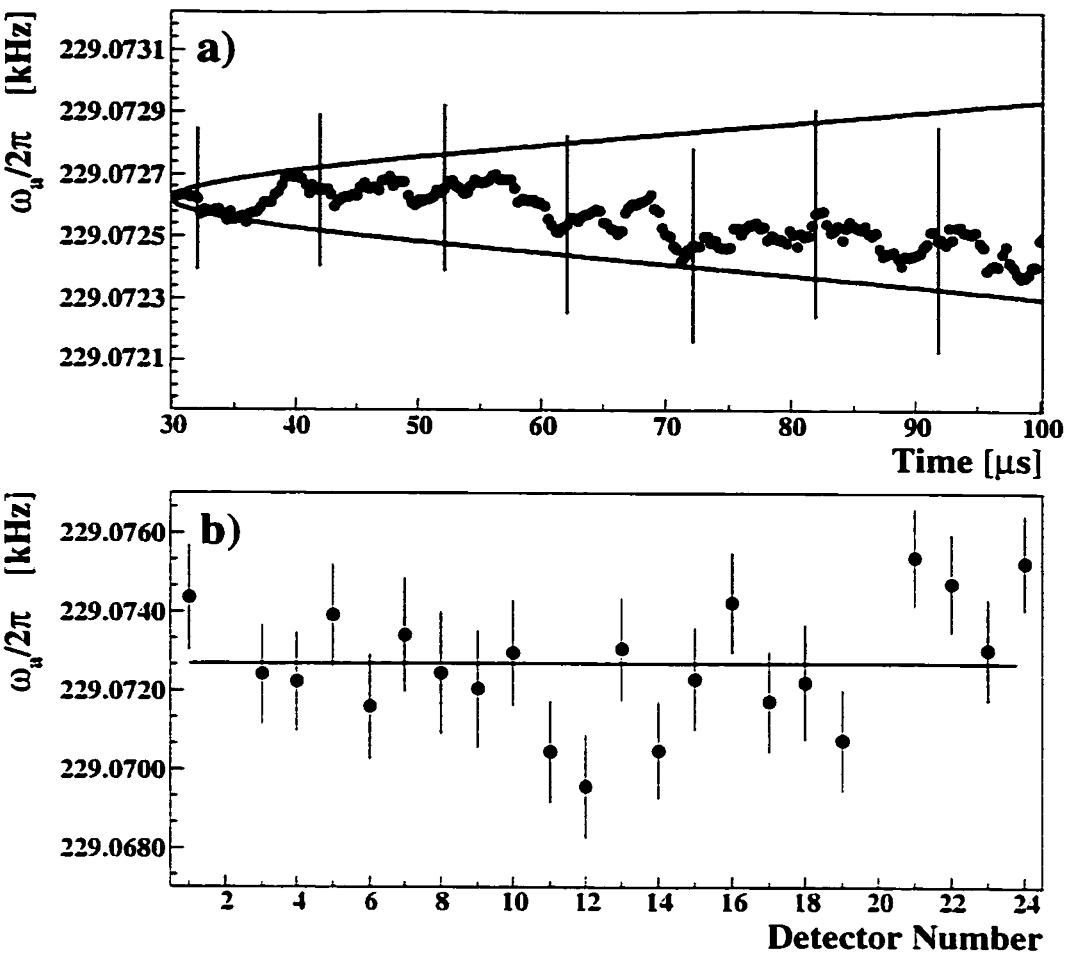

Figure 6.23: (a) The fitted frequency $\omega_a/2\pi$ vs start time of fit is shown together with representative error bars. The band indicates the size of the expected statistical fluctuations. (b) Fits to the spectra from individual detectors. Detectors 2 and 20 were excluded from the ω_a analysis because of a readout problem and a miscalibration, respectively.

times after injection and ω_a is seen to be constant within statistical errors. Fig. 6.23b shows these results for fits to the spectra from individual detectors (χ^2/d.o.f.=30/21). The result for ω_a obtained from the average of individual detector fits (Fig. 6.23b) agrees with the result from the fit to the sum (Fig. 6.23a) to within 0.07 ppm. The fitted lifetime, after correcting for muon loss, agrees with the value expected from special relativity to better than 0.1%.

6.7 Comparison of independent analyses

Four ω_a analyses were made. Two of them used the G2off production and the other two used the G2Too production. The principal differences between the analysis[73] described before and the others consist in a somewhat different choice of data selection and fitting parameters, a refined treatment of detector gain changes, and alternative ways to determine pileup. In one analysis[72], a pileup correction was made by varying the pulse resolution time in the reconstruction algorithm, whereas in the other analysis[75] pileup is incorporated in the fitted function. The pileup phase was fixed to the value obtained from the constructed pileup spectrum. In the fourth analysis, the data are randomly split in four samples $n_1 - n_4$ which are rejoined in $u(t) = n_1(t) + n_2(t)$, $v(t) = n_3(t - \tau_a/2) + n_4(t + \tau_a/2)$, and the ratio

$$r(t) = \frac{u(t) - v(t)}{u(t) + v(t)} = A(E)\sin(\omega_a t + \phi_a(E)) + \frac{1}{16}\left(\frac{\tau_a}{\tau_\mu}\right)^2 \qquad (6.11)$$

where τ_a is an estimate of the $g - 2$ period and τ_μ is the dilated lifetime of the muons in the storage ring. This ratio is largely independent of changes of observed counts on time scales larger than τ_a, *e.g.* the muon lifetime. The ratio can thus be fitted with fewer free parameters and its results have somewhat different systematic uncertainties[74].

The results from the analyses are found to agree, on ω_a to within 0.3 ppm. This is within the statistical variation of 0.4 ppm expected from the use of slightly different data in the respective analyses.

6.8 Radial electric field and pitch corrections

Two corrections have to be made to the ω_a from the fitting because of the presence of a radial electric field and because of vertical betatron oscillations of the muon beam.

Eq. 3.1.

$$\vec{\omega}_a = \vec{\omega}_s - \vec{\omega}_c = -\frac{e}{m_\mu c}\left[a_\mu \vec{B} - \left(a_\mu - \frac{1}{\gamma^2 - 1}\right)\vec{\beta} \times \vec{E}\right]. \qquad (6.12)$$

has a contribution $\left(a_\mu - \frac{1}{\gamma^2-1}\right)\vec{\beta} \times \vec{E}$ from the electric field. This contribution vanishes for muons with the "magic" gamma. $\gamma_{\text{magic}} = 29.3$. Such muons have an equilibrium orbit with a radius $r_{\text{magic}} = 7.112$ m. However, not all muons have exactly the "magic" gamma. Therefore, the measured ω_a has a contribution from the electric field[76]. Since the direction of $\vec{\beta}$ is perpendicular to the radial and vertical direction in our experiment, the electric field contribution

$$\Delta\omega_a = \frac{e}{m_\mu c}\left(a_\mu - \frac{1}{\gamma^2 - 1}\right)\vec{\beta} \times \vec{E}$$

$$
\begin{aligned}
&= \frac{e}{m_\mu c}\left(a_\mu - \frac{1}{(\gamma_{\text{magic}}+\Delta\gamma)^2-1}\right)\beta E_r \\
&= -\frac{2\beta E_r}{B}\frac{\Delta\gamma}{\gamma_{\text{magic}}}\omega_a,
\end{aligned}
\tag{6.13}
$$

where E_r is the radial electric field and $\Delta\gamma/\gamma_{\text{magic}}$ is related to the muon momentum spread $\Delta p/p_{\text{magic}} \approx 0.6\%$. If r_e is the displacement of the equilibrium orbit of the muon from $r_{\text{magic}} = 7.112$ m and r is the instantaneous radial displacement of the muon,

$$
\frac{\Delta\gamma}{\gamma_{\text{magic}}} = (1-n)\frac{r_e}{r_{\text{magic}}}, \qquad E_r = n\beta B\frac{r}{r_{\text{magic}}}, \tag{6.14}
$$

where the field index $n = 0.137$ in Eq. 3.20. Hence,

$$
\Delta\omega_a = -2n(1-n)\frac{rr_e}{r^2_{\text{magic}}}\omega_a. \tag{6.15}
$$

Averaging over all muons, we get

$$
\Delta\omega_a = -2n(1-n)\frac{\langle r_e^2\rangle}{r^2_{\text{magic}}}\omega_a. \tag{6.16}
$$

The muon radial distribution was measured by the fast rotation studies discussed in Sec. 5.9 and is shown in Fig. 5.38. The result $\langle r_e^2\rangle = 1.107$ cm^2 gives $\Delta\omega_a = -0.51 \times 10^{-6} \cdot \omega_a$.

The other correction arises from vertical betatron oscillations and is called pitch correction. Eq.6.12 is exact only when the momentum of the muon $\vec{p}_\mu$ is perpendicular to the magnetic field $\vec{B}$. Vetical betatron oscillation changes the angle between $\vec{p}_\mu$ and $\vec{B}$ and gives a contribution to ω_a,

$$
\Delta\omega_a = -\frac{1}{2}\langle\theta^2\rangle\omega_a = -\frac{1}{2}n\frac{\langle y^2\rangle}{r^2_{\text{magic}}}\omega_a, \tag{6.17}
$$

where θ is the deviation of the angle between $\vec{p}_\mu$ and $\vec{B}$ from $\pi/2$ and y is the vertical displacement from the midplane of the storage ring. Simulations[65] show that $\Delta\omega_a = -0.29 \times 10^{-6} \cdot \omega_a$.

The total contribution to ω_a from the two effects is

$$
\Delta\omega_a = (-0.80 \pm 0.08) \times 10^{-6} \cdot \omega_a, \tag{6.18}
$$

where the uncertainty is dominated by the 0.5 mm uncertainty in the positions of the quadrupole plates. A correction of $(+0.8 \pm 0.08) \times 10^{-6} \cdot \omega_a$ is applied to the ω_a from the fitting of positron time spectra[65, 77].

Table 6.1: Systematic errors for the ω_a analysis of the 1999 data

Source of errors	Size [ppm]
Coherent betatron oscillation	0.20
Pileup	0.13
AGS background	0.10
Lost muons	0.10
Timing shifts	0.10
E field and vertical betatron oscillation	0.08
Binning and fitting procedure	0.07
Beam debunching/randomization	0.04
Gain changes	0.02
Total systematic error on ω_a	0.4

6.9 ω_a and its systematic errors

We combined the results from the four analyses[78] and obtain

$$\omega_a/2\pi = 229\ 072.8 \pm 0.3 \text{ Hz } (1.3 \text{ ppm}). \tag{6.19}$$

The error reflects the total uncertainty, accounts for the strong correlations between the individual results, and is dominated by the statistical contribution of 1.3 ppm. The systematic errors are listed in Table 6.1. The errors due to gain changes, lost muons, and pileup may be correlated because they have similar effects on the number of detected positron with energy $E > 2GeV$. They are added linearly. The other errors are uncorrelated and were added in quadrature. Most of the systematics were common to all four analyses. Spin resonances, fit start time, and clock synchronization were considered and each was estimated to be less than 0.01 ppm.

Chapter 7

Conclusions

7.1 Result for a_μ from the 1999 data

The analysis of $\tilde{\omega}_p$ and ω_a were made separately and independently. The free proton spin precession frequency in the magnetic field averaged over the muon distribution in space and time for the 1999 data is

$$\tilde{\omega}_p/2\pi = 61\ 791\ 256 \pm 25 \text{ Hz } (0.4 \text{ pm}), \tag{7.1}$$

and the muon $g-2$ precession frequency is

$$\omega_a/2\pi = 229072.8 \pm 0.3 \text{ Hz } (1.3 \text{ ppm}). \tag{7.2}$$

After both analyses were finalized. the ratio between two frequencies was evaluated

$$R = \omega_a/\tilde{\omega}_p = 37\ 072\ 043(51)^{-10}. \tag{7.3}$$

The errors of $\tilde{\omega}_p$ and ω_a are added in quadrature to obtain the error of R. In principle. the two frequencies ω_p and ω_a should be determined for each data-taking run and then R evaluated for each data-taking run should be averaged as

$$R = \langle R \rangle = \langle \frac{\omega_a}{\omega_p} \rangle. \tag{7.4}$$

A simulation was made to determine the difference between the R value from either method. Eleven sets of decay positron data were generated with

$$\begin{aligned} \omega_{pi} &= \omega_{p0}(1 + i^2 \times 10^{-6}) \\ \omega_{ai} &= \omega_{a0}(1 + i^2 \times 10^{-6}), \qquad i = 0, 1, 2, \ldots, 10, \end{aligned} \tag{7.5}$$

where ω_{p0} and ω_{a0} are arbitrary numbers. Each set has equal number of decay positrons and the total number from all sets is about 10^{11}. The value of R is

$$R = \langle \frac{\omega_{ai}}{\omega_{pi}} \rangle = \frac{\omega_{a0}}{\omega_{p0}}. \tag{7.6}$$

These 11 sets of data were added and fitted to obtain $\langle\omega_a\rangle$. The results are

$$\begin{aligned} \langle\omega_p\rangle &= \omega_{p0} \times (1 + 35.00 \times 10^{-6}), \\ \langle\omega_a\rangle &= \omega_{a0} \times (1 + (34.998 \pm 0.012) \times 10^{-6}), \\ \frac{\langle\omega_a\rangle/\langle\omega_p\rangle - \omega_{a0}/\omega_{p0}}{\omega_{a0}/\omega_{p0}} &= 0.020 \pm 0.012 \times 10^{-6}. \end{aligned} \tag{7.7}$$

The difference between the R values from the two methods is 0.020±0.012 ppm where the error is due to statistics in the simulation. Since our magnetic field did not change by more than 20 ppm during the 1999 run as shown in Fig. 5.32, the two methods for calculating R are equivalent in our experiment.

The muon anomalous magnetic moment is evaluated to be

$$a_{\mu^+} = \frac{R}{\lambda - R} = 11\ 659\ 202(14)(6) \times 10^{-10}\ (1.3\ \text{ppm}), \tag{7.8}$$

where $R = \omega_a/\tilde{\omega}_p$, $\mu_\mu = e\hbar(1+a_\mu)/(2m_\mu c)$, and $\lambda = \mu_\mu/\mu_p = 3.183\ 345\ 39(10)$ [16]. This new result is in good agreement with previous measurements[9, 11, 12] and reduces the combined error by a factor of about three.

In Fig. 7.1, the five most recent measurements of a_μ are shown along with the standard model prediction. The difference between the weighted mean of the experimental results, $a_\mu = 11\ 659\ 203(15) \times 10^{-10}(1.3\ \text{ppm})$, and the theoretical value $a_\mu(\text{SM}) = 11\ 659\ 177(7) \times 10^{-10}$ (0.6 ppm) from the standard model (see Chapter 2) is

$$a_\mu(\text{exp}) - a_\mu(\text{SM}) = 26(16) \times 10^{-10}. \tag{7.9}$$

7.2 Future Perspectives

Since the data collection period in 1999, the muon $g-2$ experiment has taken data on μ^+ in 2000 and its first data on μ^- in 2001 (cf. Table 7.1). The analyzable events in the 2000 run are about 3.8×10^9 decay positrons and the statistical error for ω_a is 0.62 ppm[14]. The analyzable events are expected to be 3×10^9 decay electrons from the data taken in 2001, corresponding to statistical uncertainties of 0.74 ppm. If the results for a_{μ^+} and a_{μ^-} are found to be in agreement, as is expected from CPT invariance, the values will be combined. The combined statistical uncertainty from all the data collected through 2001 is projected to reach 0.4 ppm.

After the data collection period in 1999, we replaced the inflector with a new one which has a much smaller fringe field, which thus improved field homogeneity and measurement. During the data collection period in 2000 and 2001, we did additional calibrations during the running period and improved the calibration by measuring the position of the probes inside the trolley shell. We installed a sweeper magnet in the beamline after the data collection in 1999.

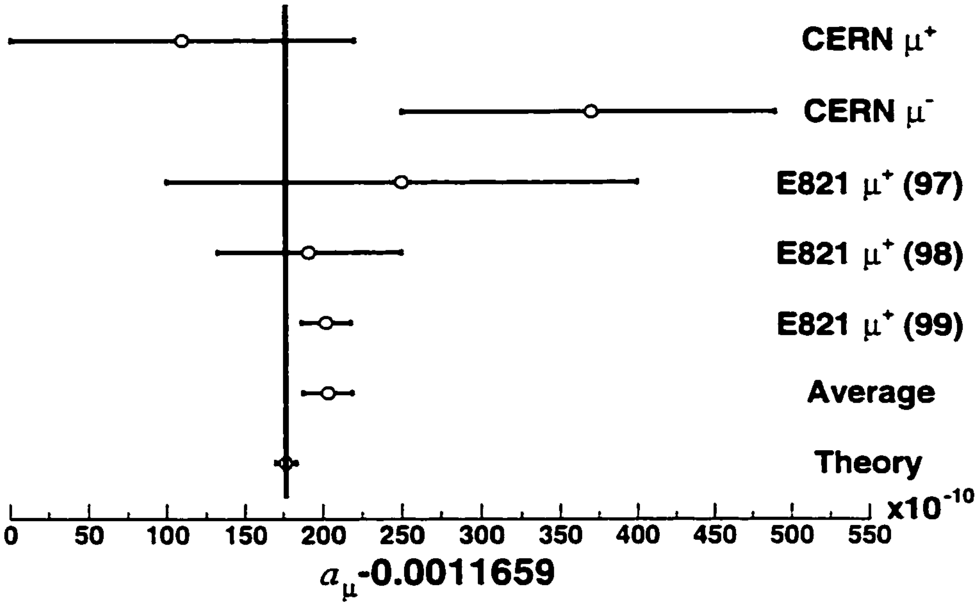

Figure 7.1: Measurements of a_μ and the standard model prediction with their total errors.

Year:	1999	2000	2001	*2003*
beam:	μ^+	μ^+	μ^-	μ^-
detected events:	2.9×10^9	7×10^9	4×10^9	8×10^9
analyzable events:	1.0×10^9	3.8×10^9	3×10^9	6×10^9
statistical uncertainty:	1.25 ppm	0.62 ppm	0.74 ppm	0.5 *ppm*
	0.56 ppm		0.41 *ppm*	
	0.33 *ppm*			
systematic uncertainty:	0.5 ppm	0.4 ppm	0.3 ppm	0.3 *ppm*

Table 7.1: Sample size and statistical and systematic uncertainties from the 1999–2001 data-taking periods, and the projected increase from our proposed 2003 run.

This magnet reduced the AGS background(flashlets). We also improved our understanding of the effects of coherent betatron oscillation and adjusted the operating settings of our experiment accordingly in the 2001 running period. As the result of these combined efforts, the systematic error for ω_a in 2000 run is 0.4 ppm[14], and we tentatively forsee a reduction of the systematic errors to about 0.3 ppm on our future results (cf. Table 7.1).

On the theoretical side, the evaluation of a_μ from Standard Model theory has achieved an accuracy of about 0.6 ppm, which predominantly comes from the uncertainties in the lowest order hadronic contribution. New experimental measurements of

$$R(s) = \frac{\sigma_{total}(e^+e^- \to hadrons)}{\sigma_{total}(e^+e^- \to \mu^+\mu^-)} \tag{7.10}$$

from Beijing[36], Novosibirsk[37] and the Frascati ϕ factory, and measurements of hadronic τ decay[25] should reduce the error in a_μ(had 1). The treatment of the τ decay data to evaluate a_μ(had 1) will benefit from further study of the CVC hypothesis.

With smaller uncertainties for both the experimental measurement and the theoretical calculation for a_μ, the comparison between two values will remain of great interest for years to come.

Bibliography

[1] R.S. Van Dyck Jr., P.B. Schwinberg, and H.G. Dehmelt, Phys. Rev. Lett., **59**, 26 (1987); R.S. Van Dyck Jr., in *Quantum Electrodynamics*, ed. T. Kinoshita (*World Scientific, Singapore*, 1990), 322.

[2] V.W. Hughes and T. Kinoshita, Rev. Mod. Phys. **71**, No. 2, S133(1999).

[3] T. Kinoshita in *Quantum Electrodynamics*, ed. T. Kinoshita (*World Scientific, Singapore*, 1990), 218.

[4] P.J. Mohr and B.N. Taylor, Rev. Mod. Phys. **72**, 351 (2000).

[5] V.W. Hughes and T. Kinoshita, Rev. Mod. Phys. **71** Centenary 1999 S 1333.

[6] A. Jeffery *et al.*, Conf. on Precision Electromagnetic Measurements, Braunschweig, Germany, 1996.

[7] G. Charpak *et al.*, Nuovo Cim. **37** 1241 (1965).

[8] J. Bailey *et al.*, Nuovo Cim. **A9** 369 (1972).

[9] J. Bailey *et al.*, Nucl. Phys. **B150**, 1 (1979).

[10] A. Czarnecki and W.J. Marciano, Nucl. Phys. (Proc. Suppl.) **B76**, 245 (1999).

[11] Muon $(g-2)$ Collaboration, R.M. Carey *et al.*, Phys. Rev. Lett. **82**, 1632 (1999).

[12] Muon $(g-2)$ Collaboration, H.N. Brown *et al.*, Phys. Rev. D **62**, 091101 (2000).

[13] Muon $(g-2)$ Collaboration, H.N. Brown *et al.*, Phys. Rev. Lett. **86**, 2227 (2001).

[14] Muon $(g-2)$ Collaboration, G.W. Bennett *et al.*, Phys. Rev. Lett. **89**, 101804 (2002).

[15] T. Kinoshita and W.J. Marciano in *Quantum Electrodynamics* ed. T. Kinoshita (World Scientific, Singapore, 1990), p. 419.

[16] D.E. Groom *et al.*, Eur. Phys. J. **C15**, 1 (2000).

[17] A. Czarnecki, B. Krause, and W. Marciano, Phys. Rev. Lett. **76**, 3267 (1996).

[18] A. Czarnecki, BB. Krause, and W. Marciano, Phys. Rev. **D62**, R2619 (1995).

[19] G. Degrassi and G.F. Giudice, Phys. Rev. **D58**, 053007 (1998).

[20] M. Gourdin and E. de Raphael, Nucl. Phys. **B10**, 667, (1969).

[21] M. Davier and A. Höcker, Phys. Lett. **B435**, 427 (1998).

[22] R. Alemany, M. Davier and A. Höcker, Eur. Phys. J. **C2**, 123 (1998).

[23] CMD2 Collaboration, R.R. Akhmetshin *el al.*, Phys. Lett. **B475**, 190 (2000); CMD2 Collaboration, R.R. Akhmetshin *et al.*, Nucl. Phys. **A675**, 424 (2000). CMD2 Collaboration, R.R. Akhmetshin *et al.*, Phys. Lett. **B527**, 161 (2002).

[24] Z.G. Zhao. Int. J. Mod. Phys. **A15**, 3739 (2000); BES Collaboration. J.Z. Bai *et al.*, Phys. Rev. Lett. **84**. 594 (2000).

[25] CLEO Collaboration. S. Anderson *et al.*. Phys. Rev. **D61**. 112002 (2000).

[26] The Aleph collaboration. R. Barate *et al.*. Z. Phys. **C76**. 15 (1997); Eur. Phys. J. **C4**. 409 (1998).

[27] The Opal collaboration, K. Ackerstaff *et al.*. Eur. Phys. J. **C7**. 571 (1999).

[28] B. Krause. Phys. Lett. **B390**. 392 (1997).

[29] J. Bijnens. E. Pallante. and J. Prades. Nucl. Phys. **B474**. 379 (1996).

[30] M. Hayakawa and T. Kinoshita. Phys. Rev. **D57**, 465 (1998).

[31] M. Knecht and A. Nyffeler. Phys. Rev. **D65**.073034. (2002). hep-ph/0111058.

[32] M. Knecht. A. Nyffeler. M. Perrottet. and E. De Rafael. Phys. Rev. Lett. **88**, 071802 (2002), hep-ph/0111059.

[33] I. Blokand. A. Czarnecki. and K. Melnikov. Phys. Rev. Lett. **88**. 071803 (2002), hep-ph/0112117.

[34] M. Hayakawa and T. Kinoshita, hep-ph/0112102 (2001).

[35] J. Bijnens. E. Pallante. and J. Prades. Nucl. Phys. **B626**. 410 (2002). hep-ph/0112255.

[36] J.Z Bai *et al.*, Phys. Rev. Lett. **88** 101802 (2002), hep-ex/0102003.

[37] CMD2 Collaboration, R.R. Akhmetshin *el al.*, Phys. Lett. **B527**, 161 (2002), hep-ex/0112031.

[38] A. Czarnecki and W.J. Marciano, Phys. Rev. **D64** 013014 (2001).

[39] T. Moroi, Phys. Rev. **D53**, 6565 (1996); S. Komine, T. Moroi, M. Yamaguchi, Phys. Lett. **B506**, 93 (2001).

[40] U. Chattopadhyay and P. Nath, Phys. Rev. **D53**, 1648 (1996); U. Chattopadhyay and P. Nath, Phys. Rev. Lett. **86**, 5854 (2001).

[41] J.L. Lopez, D.V. Nanopoulos and X. Wang, Phys. Rev. **D49** 366 (1994); J.R. Ellis, D.V. Nanopoulos, K.A. Olive, Phys. Lett. **B508**, 65 (2001).

[42] S. Davidson, D. Bailey, and B.A. Campbell, Zeits. f. Physik **C61**, 613 (1994); G. Couture and H. König, Phys. Rev. **D53**, 555 (1996); D. Chakraverty, D. Choudhury, and A. Datta, Phys. Lett. **B506**, 103 (2001); K. Cheung, Phys. Ref. **D64**, 033001 (2001).

[43] T. Appelquist and B.A. Dobrescu, Phys. Lett. **B516**. 85 (2001).

[44] W. Marciano, in *Particle Theory and Phenomenology*, ed. by K. Lassila *et al.*, (*World Scientific, Singapore*, 1996), 22.

[45] W. Liu *et al.*, Phys. Rev. Lett **82**, 711 (1999).

[46] Muon g-2 Collaboration, BNL AGS E821 Design Report, 3rd ed., March (1995).

[47] F. Krienen, D. Loomba, and W. Meng, Nucl. Instr. Meth. **A283**, 5 (1989); A. Yamamoto *et al.*, in *Proceedings of the 15th International Conference on Magnet Technology*, pl 246, (Science Press, Beijing, 1998).

[48] A. Yamamoto *et al.*, Nucl. Instr. Meth. **A491**, 23 (2002)

[49] G.T. Danby *et al.*, Nucl. Instr. Meth. **A457**, 151 (2001).

[50] A. Grossmann, Ph.D dissertation, Universität Heidelberg (1998).

[51] J.H. Simpson and H.Y. Carr, Phys. Rev. **111**, 1201 (1958).

[52] R. Prigl *et al.*, Nucl. Instr. Meth. A **A374**, 118 (1996).

[53] R. Prigl, Ph.D dissertation, Universität Heidelberg (1994)

[54] X. Fei, V.W. Hughes and R. Prigl, Nucl. Instr. Meth. **A394**, 349 (1997).

[55] W.D. Phillips *et al.*, Metrologia 13, 179 (1977).

[56] B.W. Petley *et al.*, Metrologia 20, 81 (1984).

[57] E. Efstathiadis *et al.*, accepted by Nucl. Instr. Meth. A (2002).

[58] Y. Semertzidis *et al.*, submitted to Nucl. Instr. Meth. A (2002).

[59] S. Sedykh *et al.*, Nucl. Instr. Meth. **A455**, 346 (2000).

[60] S.I. Redin, Ph.D dissertation, Yale University (1999).

[61] V.W. Hughes in "*Physics Since Parity Symmetry Breaking*", ed. Fan Wang, World Scientific, Singapore, 508 (1999).

[62] Private communication with G.T. Danby and J. Jackson.

[63] Y. Olov, C.S. Ozben and Y.K. Semertzidis, Nucl. Instr. Meth. **A482**, 767 (2002).

[64] S.I. Redin, internal g-2 note 381 (2001).

[65] J.M. Paley, internal g-2 note 379 (2001)

[66] I. Logashenko, internal g-2 note 369 (2000).

[67] I. Logashenko, internal g-2 note 378 (2000).

[68] V. Druzhinin and G. Fedotovich, interanl g-2 note 375 (2000).

[69] C.S. Özben, Y.K. Semertzidis, internal g-2 note 365 (2000).

[70] F.J.M. Farley *et al.*, internal g-2 note 377 (2000).

[71] H. Deng *et al.*, internal g-2 note 394 (2001).

[72] G. Onderwater, internal g-2 note 390 (2001).

[73] C.S. Özben, internal g-2 note 385 (2001).

[74] L. Duong, Ph.D dissertation, University of Minisota (2002).

[75] A. Trofimov, Ph.D dissertation, Boston University (2001).

[76] F.J.M. Farley and E. Picasso in *Quantum Eletrodynamics*, edited by T. Kinoshita (*World Scientific, Singapore*, 1990), p. 479.

[77] F.J.M. Farley, internal g-2 note 370 (2000).

[78] O. Rind and E. Sichtermann, internal g-2 note 380 (2001)